Assessing the Potential of Sentinel-1 and Sentinel-2 Satellite Imagery for Shoreline Classification in Support of Oil Spill Preparedness and Response

By

Maria Yulmetova

A thesis submitted to the

School of Graduate Studies

in partial fulfillment of the requirements for the degree of

Master of Engineering

Faculty of Engineering and Applied Science

Memorial University of Newfoundland

October 2021

St. John's, Newfoundland and Labrador, Canada

This page is intentionally left blank

ABSTRACT

Coastal zones are critical ecosystems that provide important habitat for marine animals, fish, shellfish, birds, and many other species. However, there is a risk of mineral oil impacting in these areas due to human activities offshore. Shoreline classification is the first step to establishing response contingency plans in case of an oil spill.

This study estimates the potential of using open-access, high-resolution Sentinel-1 and Sentinel-2 imagery for the mapping of shoreline types in support of oil spill preparedness and response activities. The two classification maps, depicting shoreline and coastal land cover, were produced using an advanced object-based Random Forest (RF) algorithm. Various features extracted from multi-source data, including spectral, texture, ratio, polarimetric features, and digital elevation model (DEM), were analyzed to identify the most valuable features for discrimination between different shoreline types. Multiple classification scenarios with the most useful features were then assessed and compared to find the best classification model.

The developed algorithm achieved accuracies of 87.10% and 84.75% of coastal land cover and shoreline maps. These results demonstrated the high potential of using freely available Sentinel-1 and -2 satellite data for coastal mapping.

KEY WORDS

Shorelines, Sentinel-2, Sentinel-1, Object-Based Classification, Random Forest, Canada, Newfoundland

ACKNOWLEDGEMENTS

I would like to take this opportunity to express my deepest thanks to those who helped along the journey of my Master's.

I express my sincere gratitude to my (co-)supervisors, Vandad Talimi, Thomas Puestow, Sherry Warren, and Masoud Mahdianpari, for their guidance, continuous support, and encouragement. Thomas Puestow introduced this interesting topic to me, provided valuable suggestions and advice during this project. I am grateful for his technical expertise and for the opportunity to learn from his experience. Sherry Warren was always very kind and ready to help at every moment of my study. Her help was fast and effective. Vandad Talimi supported me in every step during my master's program and was ready to solve any problems that arose. I am grateful to Masoud Mahdianpari for his time, valuable comments, and all the support provided during my program.

None of this would have been possible without the Ocean Frontier Institute's financial support that provided the research funding through an award from the Canada First Research Excellence Fund.

I would like to thank the Canada Center for Mapping and Earth Observation and Environment and Climate Change Canada for providing aerial photography.

I am grateful to my husband, without his support this work would never have been possible, and to my whole family for all their love and support, I got in every step of my life.

TABLE OF CONTENTS

LIST OF TABLES vii

LIST OF FIGURES ix

ACRONYMS xii

SYMBOLS xv

1. Introduction 1

1.1 Overview 1

1.2 Research Goals and Objectives 5

1.3 Document Structure 6

2. Background 7

2.1 Shoreline Assessment and Classification 7

2.2 Land Cover Classification Using Satellite Remote Sensing 20

2.2.1 Satellite Sensor Characteristics 20

2.2.2 Image Preprocessing 25

2.2.3 Feature Extraction 27

2.2.4 Image Classification 33

2.3 Satellite-Based Shoreline Classification 39

3. Study Area and Data 48

3.1 Study Area 48

3.2 Data 51

3.2.1 Satellite Data 51

3.2.2 Auxiliary Data 56

3.2.3 Field Data 56

4. Methodology 61

4.1 Image Preprocessing 62

4.2 Feature Extraction & Selection 63

4.3 Segmentation 68

4.4 Random Forest Classification 69

4.5 Accuracy Assessment 71

5. Results 75

5.1 Selection of Predictor Variables 75

5.1.1 Spectral Bands and Indices 76

5.1.2 Principal Component Analysis 79

5.1.3 Texture Features 80

5.2 Classification 84

5.2.1 Segmentation 84

5.2.2 Classification Scenarios 87

6. Discussion 107

6.1 Classification Scheme 107

6.2 Feature Extraction & Selection 108

6.3 Classification 112

7. Conclusions 116

8. Future Work 118

References 120

Appendix A : Spatial Resolution Enhancement Results 160

Appendix B : Correlation Matrices 161

Appendix C : Box-and-Whiskers Plots 164

Appendix D : Principal Components 179

LIST OF TABLES

Table 2.1. The elements of the Pre-SCAT mapping dataset 10

Table 2.2. Comparison of shoreline classification schemes 13

Table 2.3. SCAT shoreline types characteristics and oil response considerations 16

Table 2.4. Characteristics of some of the microwave bands used in remote sensing 23

Table 2.5. Satellite-based shoreline classification studies over the Canadian coastline 41

Table 3.1. Sentinel-2 sensor characteristics (ESA, n.d.) 52

Table 3.2. Low water level around the time of Sentinel-2 image acquisition. 54

Table 3.3. Water level around the time of Sentinel-1 image acquisition 55

Table 3.4. Shoreline types used in this study and corresponding SCAT classes 60

Table 4.1. Derived indices and band ratios details 65

Table 4.2. GLCM texture measures and their equations. 67

Table 4.3. The accuracy measures calculated in this research 72

Table 4.4. The matrix of correctly and incorrectly classified pixels for classifications used for McNemar's test 73

Table 5.1. Extracted features from Sentinel-2 and Sentinel-1. 76

Table 5.2. Percent and Accumulative of Eigenvalues 79

Table 5.3. Texture measures extracted in the study 81

Table 5.4. Shoreline classification accuracy and Kappa coefficients of segmented images with various scale parameters 87

Table 5.5. Classification scenarios tested in this research 89

Table 5.6. Confusion matrix obtained from the classification scenario 1 90

Table 5.7. Confusion matrix obtained from the classification scenario 2 91

Table 5.8. Confusion matrix obtained from the classification scenario 3 92

Table 5.9. Confusion matrix obtained from the classification scenario 4 93

Table 5.10. Confusion matrix obtained from the classification scenario 5 93

Table 5.11. Confusion matrix obtained from the classification scenario 6 94

Table 5.12. Confusion matrix obtained from the classification scenario 7 95

Table 5.13. Confusion matrix obtained from the classification scenario 8 96

Table 5.14. Confusion matrix obtained from the classification scenario 9 96

Table 5.15. Confusion matrix obtained from the classification scenario 10 97

Table 5.16. *z* score obtained from comparison accuracies from different classification scenarios 103

Table 5.17 Shoreline classification confusion matrix..... 105

LIST OF FIGURES

Figure 2.1. Photograph examples of SCAT shoreline types (Wynja et al., 2014)..... 15

Figure 3.1. Study area. 48

Figure 3.2. Sentinel-2 image coverage. 53

Figure 3.3. Sentinel-1 image coverage. 55

Figure 3.5. Initial shoreline types identified during fieldwork. 59

Figure 4.1. Methodology..... 61

Figure 5.1. Spectral profiles of shoreline types using Sentinel-2A data..... 77

Figure 5.2. The most important GLCM texture measures. 82

Figure 5.3. Correlation matrix of features selected for the final classification..... 83

Figure 5.4. Sentinel-2 image segmentation results obtained by applying various variables and parameters. 86

Figure 5.5. Coastal land classification. 99

Figure 5.6. The subsets of coastal land cover map and shoreline classification on aerial photography. 100

Figure 5.7. PAs for coastal land cover types obtained in different scenarios. 101

Figure 5.8. UAs for coastal land cover types obtained in different scenarios. 102

Figure 5.9 Shoreline classification map. 104

Figure 5.10. The distribution of classified shoreline classes along the study area. 106

Figure A.1. Original B5 and B11 20m-resolution images (a, d) and the corresponding 10-m resolution products obtained after resampling (d, e) and super-resolution (c, f) algorithms..... 160

Figure B.1. Matrix of correlation between Sentinel-2 bands, principal components, and spectral indices. 161

Figure B.2. Correlation matrix of GLCM texture measures obtained from Sentinel-2 VNIR bands. 163

Figure C.1. Pixels distributions of the shoreline classes in Sentinel-2 B2. 164

Figure C.2. Pixels distributions of the shoreline classes in Sentinel-2 B3. 164

Figure C.3. Pixels distributions of the shoreline classes in Sentinel-2 B4. 165

Figure C.4. Pixels distributions of the shoreline classes in Sentinel-2 B5. 165

Figure C.5. Pixels distributions of the shoreline classes in Sentinel-2 B6. 166

Figure C.6. Pixels distributions of the shoreline classes in Sentinel-2 B7. 166

Figure C.7. Pixels distributions of the shoreline classes in Sentinel-2 B8. 167

Figure C.8. Pixels distributions of the shoreline classes in Sentinel-2 B8a. 167

Figure C.9. Pixels distributions of the shoreline classes in Sentinel-2 B11. 168

Figure C.10. Pixels distributions of the shoreline classes in Sentinel-2 B12. 168

Figure C.11. Pixels distributions of the shoreline classes in MNDWI. 169

Figure C.12. Pixels distributions of the shoreline classes in NDBI. 169

Figure C.13. Pixels distributions of the shoreline classes in Ratio 1. 170

Figure C.14. Pixels distributions of the shoreline classes in Ratio 2. 170

Figure C.15. Pixels distributions of the shoreline classes for PC1. 171

Figure C.16. Pixels distributions of the shoreline classes for PC2. 171

Figure C.17. Pixels distributions of the shoreline classes for PC3. 172

Figure C.18. Pixels distributions of the shoreline classes for PC4. 172

Figure C.19. Pixels distributions of the shoreline classes for PC5. 173

Figure C.20. Pixels distributions of the shoreline classes for PC6. 173

Figure C.21. Pixels distributions of the shoreline classes for PC7. 174

Figure C.22. Pixels distributions of the shoreline classes for PC8. 174

Figure C.23. Pixels distributions of the shoreline classes for PC9. 175

Figure C.24. Pixels distributions of the shoreline classes for PC10. 175

Figure C.25. Pixels distributions of the shoreline classes for B2 GLCM ASM measure. 176

Figure C.26. Pixels distributions of the shoreline classes for B2 GLCM contrast measure. 176

Figure C.27. Pixels distributions of the shoreline classes for B2 GLCM E measure. 177

Figure C.28. Pixels distributions of the shoreline classes for B2 GLCM VAR measure. 177

Figure C.29. Pixels distributions of the shoreline classes for B4 GLCM contrast measure. 178

Figure C.30. Pixels distributions of the shoreline classes for B4 GLCM ENT measure. 178

Figure D.1. Principal components obtained from Sentinel-2 red, green, blue, NIR, narrow-NIR, RE 1-3, SWIR-1, and SWIR-2 band. 179

ACRONYMS

AFRI	Aerosol-free Vegetation Index (p.65)
AFRI2	Aerosol-free Vegetation Index 21 (p.65)
ASM	Angular Second Moment (p.30)
B1-B12	Sentinel-2 band from 1 to 12 (p.66)
BCCMP	British Columbia Coastal Mapping Program (p.12)
BI2	Second Brightness Index (p.65)
BI2	Brightness Index (p.65)
BV	Brightness Value (p.30)
CART	Classification and Regression Trees (p.36)
CDEM	Canadian Digital Elevation Model (p.56)
CI	Color Index (p.65)
CIRedEdge	Red Edge Chlorophyll Index (p.66)
CON	Contrast (p.30)
COR	Correlation (p.31)
DEM	Digital Elevation Model (p.32)
DISS	Dissimilarity (p.30)
DN	Digital Number (p.28)
DT	Decision Tree (p.37)
DVI	Difference Vegetation Index (p.65)
E	Energy (p.30)
ECCC	Environment and Climate Change Canada (p.3)
EMR	Electromagnetic Radiation (p.20)
ENT	Entropy (p.30)
ESA	European Space Agency (p.25)
ESI	Environmental Sensitivity Index (p.12)
EVI2	Two-band Enhanced Vegetation Index (p.66)
EVI	Enhanced Vegetation Index (p.66)
FQ	Fine-Quad (p.44)
GEMI	Global Environment Monitoring Index (p.66)
GIS	Geographical Information System (p.10)
GI	Greenness Index (p.66)
GLCM	Gray-Level Co-occurrence Matrix (p.30)
GNDVI	Green Normalized Difference Vegetation Index (p.65)
GPS	Global Positioning System (p.11)
GRD	Ground Range Detected (p.54)
GRVI	Green-Red Vegetation Index (p.66)
HH	Horizontal transmit and Horizontal receive polarization (p.24)
HOM	Homogeneity (p.30)
HR	High Resolution (p.46)

HV	Horizontal transmit and Vertical receive polarization (p.24)
IPVI	Infrared Percentage Vegetation Index (p.65)
IRECI	Inverted Red-Edge Chlorophyll Index (p.65)
IW	Interferometric Wide (p.54)
KNN	K-Nearest Neighbor (p.36)
LAI	Leaf Area Index (p.66)
MAX	Maximum (p.30)
MCARI	Modified Chlorophyll Absorption Ratio Index Improved (p.66)
MCARI2	Modified Chlorophyll Absorption in Reflectance Index (p.66)
MIR	Mid-infrared (p.28)
ML	Maximum Likelihood (p.35)
MNDWI	Modified Normalized Difference Water Index (p.65)
MRS	Multi-resolution segmentation (p.34)
MSAVI	Modified Soil Adjusted Vegetation Index (p.65)
MSAVI2	Modified Soil Adjusted Vegetation Index (p.66)
MTVI	Modified Triangular Vegetation Index (p.66)
NDBI	Normalized Difference Built-up Index (p.66)
NDPI	Normalized Difference Pigment Index (p.65)
NDTI	Normalized Differential Turbidity Index (p.65)
NDVI	Normalized Differences Vegetation Index (p.65)
NDWI	Normalized Difference Water Index (p.65)
NIR	Near-Infrared (p.28)
NL	Newfoundland and Labrador (p.48)
NMDI	Normalized Multi-band Drought Index (p.66)
NOAA	National Oceanic and Atmospheric Administration (p.12)
NRCan	Natural Resources Canada (p.56)
OA	Overall Accuracy (p.21)
O-B	Object-Based (p.44)
OBIA	Object-based Image Analysis (p.33)
OSAVI	Optimized soil-adjusted vegetation index (p.66)
PA	Producer Accuracy (p.71)
P-B	Pixel-Based (p.44)
Pre-SCAT	Pre-spill SCAT (p.4)
PSSRA	Pigment Specific Simple Ratio (Cholophyll a) (p.65)
PVI	Perpendicular Vegetation Index (p.65)
RAR	Real Aperture Radar (p.23)
RENDVI	Red Edge Normalized Difference Vegetation Index (p.66)
RF	Random Forest (p.36)
RI	Redness Index (p.66)

RVI	Ratio Vegetation-Index (p.66)
SAR	Synthetic Aperture Radar (p.23)
SAVI	Soil Adjusted Vegetation Index (p.66)
SCAT	Shoreline Cleanup Assessment Technique (p.4)
SVM	Support Vector Machine (p.36)
SWIR	Short-wave Infrared (p.51)
TNDVI	Transformed NDVI (p.65)
UA	User Accuracy (p.71)
UTM	Universal Transverse Mercator (p.63)
UNESCO	United Nations Educational, Scientific and Cultural Organization (p.49)
VAR	Variance (p.31)
VH	Vertical transmit and Horizontal receive polarization (p.24)
VNIR	Visible and Near-Infrared (p.28)
VV	Vertical transmit and Vertical receive polarization (p.24)
WDVI	Weighted Difference Vegetation Index (p.65)

SYMBOLS

μ	Mean (p.67)
σ^2	Variance (p.67)
P	Probability (p.67)
q	Number of classes (p.72)
N	Total number of test pixels (p.72)
z	z score (p.73)
f_{12}	Number of samples correctly classified by the first scenario but misclassified by the second one (p.73)
f_{21}	Number of samples wrongly classified by the first scenario but correctly classified by the second one (p.73)
f_{11}	Numbers of samples correctly classified by both scenarios (p.73)
f_{22}	Numbers of samples correctly misclassified by both scenarios (p.73)
H_0	Null hypothesis (p.73)
X^2	Chi-squared value (p.74)
σ°	Sigma Naught backscatter (p.75)

1. Introduction

1.1 Overview

Coastal zones are critical transition areas between terrestrial environments, freshwater habitats, and the ocean (Baztan et al., 2015). A coastline, which is defined as the line of contact between land and the water body, is one of the most important linear features on the earth's surface (Alesheikh et al., 2007). These dynamic environments are among the most productive ecosystems providing spawning habitats for marine animals, fish, shellfish, birds, and many other oceanic creatures (Crossland et al., 2005). The coastal areas are highly diverse and play an essential role in transferring matter, energy, and organisms (Joensuu et al., 2018). Also, coastal areas are substantial for maintaining human life and are used as both commercial and subsistence food sources. More than half of the world's major cities are located in coastal zones, and 40% of all the people on the planet live within 100 km of a coastal zone (Saleem & Awange, 2019; Baztan et al., 2015). Besides having an aesthetic appeal, the areas near the shore provide recreational and tourism opportunities for many people.

Human activities in the marine environments, such as exploration and extraction of resources, freight and transport, marine tourism, and fishing, increases the risk of oil spills and other contaminations. Oil spills can occur for various reasons, such as a tanker accidents, discharges during the loading and unloading of oil (Fingas, 2014), illegal discharges from ships (Martín Alonso et al., 2015), or blowouts (French-McCay et al., 2018; Zhao et al., 2014), etc. It is worth noting that most oil tanker accidents occur near land, and thus, the spilled oil can reach shorelines very quickly (Wiens, 2013). That is why a rapid and effective response to an oil spill that has reached shorelines is critical.

In case of oil contamination, plants and animals populating the coastal zone may be killed outright or severely injured to dramatically decrease their survival chances (Jackson et al., 1989). For example, birds' feathers might be fouled by oil sticking them together. This results in an inability of birds to fly. Moreover, oil pollution affects the thermal balance of seabirds. If oil adheres to the plumage, water-repellant properties of the plumage reduce and an insulating layer of air is displaced by water. In this case, the seabird's heat loss can exceed their heat production causing a bird's death from hypothermia (Jenssen, 1994).

Smaller organisms can suffocate if they are covered by a thick layer of oil. Several studies have demonstrated the harmful effects of crude oil in capelin. It was shown that an oil spill occurring during springtime in the vicinity of the capelin's spawning grounds could significantly impact capelin recruitment (Frantzen et al., 2012; Khan & Payne, 2005). Even short-term exposure of capelin eggs to heavy fuel oil, at environmentally relevant total hydrocarbon content concentrations, may induce adverse developmental effects on growth and embryo development in capelin eggs, as well as mortality (Tairova et al., 2019). Therefore, there is a need for oil spill response preparedness.

There are approximately 20,000 oil tanker passages through or near Canadian waters each year. Of these, approximately 17,000 occur on the east coast of Canada (Turner, 2010). During the past decade, 176 oil spills were registered in the area of active oil exploration and production off the coast of Newfoundland and Labrador (C-NLOPB, 2020).

Despite significant development of new technologies for oil spill clean-up, looking at the examples of oil spills that occurred on March 5, 2006, in the Gulf of Finland and on November 16, 2018, near Newfoundland, it remains questionable whether the industry is capable of mitigating a large oil spill in ice-covered or harsh environments (K. Wang et al., 2008). When Newfoundland's

largest-ever oil spill occurred in 2018, zero liters (out of 250,000) of spilled oil was collected during the recovery efforts due to harsh weather conditions. Rough seas and strong northwest gale winds at the time of the spill blocked workers from attempting a cleanup over the first days, and the oil was broken down to the point that it could not be cleaned up in the following days. Failing to mitigate the oil from marine environments increases the risk of coastal areas being impacted by oil spills.

The distribution of oil washed onto a shoreline is not uniform. Being thinly spread on one location, oil can be heavily concentrated in adjacent areas (Lamarche et al., 2007). Thus, to protect coastal environments effectively, it is necessary to determine sections that are the most vulnerable to an oil spill. Oil spill contingency plans are created to address controlling and recovering an oil spill effectively. The oil spill contingency plans include the procedures, materials, and other information to quickly respond to discharged oil, including information about shoreline types that determine the choice of an oil spill mitigation technique (RRT, 2015; US EPA, 2019).

Many factors affect the behavior of oil that has reached a shoreline. According to Environment and Climate Change Canada (ECCC) (2016), the main factors include a) the physical properties of the oil, such as viscosity, density, solubility, interfacial tension, and stickiness; b) the dynamic coastal processes, such as tide, wind, water flow, and currents; and c) the physical properties of the shoreline, which include the substrate type, the form, and the slope of the coastal zone. Depending on these factors, oil can be naturally removed, buried under the upper layer of the surface, penetrate through the substrate, or be retained on the surface. Depending on oil behavior on various types of shorelines, appropriate treatment options must be selected. These treatment tactics include natural recovery, washing removal methods, physical removal techniques, or chemical and biological treatment.

Shoreline classification is the first step to creating Environmental Sensitivity Index (ESI) maps. ESI maps are an important decision-support tool used for emergency response in case of an oil spill incident (Lawal & Oyegun, 2017). They help to identify the elements at risk and prioritize the most sensitive areas for protection. These areas usually include high biodiversity, critical habitats, endangered species, critical natural resources, and others of environmental, economic, or cultural importance (Michel et al., 1995).

In Canada, the Shoreline Cleanup Assessment Technique (SCAT) is used for collecting field data to document shoreline conditions after oil spills (Lamarche et al., 2007). However, pre-spill SCAT (or pre-SCAT) procedures are still needed to support early response management and planning, reducing environmental impacts and making the response and cleanup efforts more efficient (Percy et al., 1997).

Pre-spill SCAT methodology is based on the data collected by helicopter videography (Demers et al., 2013; Wynja et al., 2014). Implementing this approach over large, remote areas may cause additional logistical challenges, higher costs, and a potential hazard for people. Thus, there is a need to explore the potential of satellite imagery classification as an alternative, cost-effective method for coastal mapping. This research utilizes imagery obtained from Sentinel-1 and Sentinel-2. These satellites provide freely available data with global coverage of land and coastal areas, revisit schedules of 5- and 6-days, and spatial resolutions of 10 and 20 m, respectively (ESA, n.d.). Applying automated processing techniques to the Sentinel satellite data allows for a more cost- and time-effective broad-scale mapping than traditional helicopter videography.

1.2 Research Goals and Objectives

The overall goal of this research was to assess the potential of Sentinel-1 and Sentinel-2 satellite data for shoreline classification in support of oil spill response. The specific study objectives were to:

1) determine shoreline categories, such as bedrock, sand, or vegetation, important for oils spill response planning that can be identified using Sentinel-1 and Sentinel-2 satellite data;
2) identify suitable features to extract shoreline categories from Sentinel-1 and -2 imagery;
3) develop a suitable processing chain to extract shoreline types from Sentinel-1 and -2 imagery; and
4) assess the accuracy and utility of the resulting shoreline classification.

The shoreline categories relevant to oil spill response planning were determined by developing a classification scheme based on the analysis of field data samples of spectral response in Sentinel-2 bands. Potentially predictable variables extracted and analyzed in this study included reflectance, radar backscatter, image transforms, image texture, and terrain parameters. The most valuable features for shoreline classification were found through feature selection and separability analysis procedures. The most suitable processing chain was identified by testing various classification scenarios using different predictable variables as well as the accuracy assessment and comparison.

1.3 Document Structure

Chapter 2 provides background information for shoreline classification methodology, including the description of classification schemes and the literature review of relevant work. The study area and data used in this investigation are described in Chapter 3. The methodology is described in detail in Chapter 4. The results of the analysis are presented in Chapter 5, while Chapter 6 comprises a critical discussion of the results of this investigation. Chapter 7 presents conclusions and recommendations for future work.

2. Background

2.1 Shoreline Assessment and Classification

On March 23, 1989, the oil tanker Exxon Valdez, loaded with approximately 200 million liters of crude oil, grounded on Bligh Reef in Prince William Sound (PWS), Gulf of Alaska, U.S., spilling 40 million liters of its cargo. An estimated 40% of the spilled oil was stranded on 783 km of shoreline, whereas 141 km (18%) were heavily oiled, 94 km (12%) were moderately oiled, 326 km (41%) were lightly oiled, and the remaining 223 km (29%) were only very lightly oiled (Neff et al., 1995).

To deal with the most extensive marine oil spill in the U.S. at that time, the largest ever containment and cleanup operation was mobilized (Neff et al., 1995). The Exxon Valdez response's cornerstone was the Shoreline Cleanup Assessment Technique (SCAT) process, which was created to provide decision-making support to Exxon’s spill-management team for shoreline treatment planning and operations throughout the response effort (ECCC, 2016; Owens & Sergy, 2004). SCAT teams analyzed shoreline physical characteristics and oiling conditions, which were later used to set priorities and methods for shoreline clean-up.

The data provided by the SCAT teams played a key role in the Exxon Valdez shoreline response operation in Alaska from 1989 through 1993 at both the strategic and tactical levels (Wiens, 2013). Later, SCAT evolved and was applied in other environments, including rivers, freshwater, and Arctic waters (Owens & Sergy, 2004). The SCAT data were fundamental for developing shoreline treatment recommendations on the Deepwater Horizon shoreline response from 2010 through 2012 in the Gulf of Mexico (Michel et al., 2013; Santner et al., 2011).

In the wake of the Exxon Valdez spill, the International Convention on Oil Pollution Preparedness, Response, and Cooperation (OPRC) was established in 1990 to facilitate international cooperation on oil pollution emergencies (Canada, 2020). Many countries, including Canada, adopted the SCAT concept and continued developing standardized guidelines for oil spill response (ECCC, 2016; NOAA, 2013; Owens & Sergy, 2004). The development of these guidelines was necessary to provide responders with specific and detailed information for operational-level decisions. These standards would help prioritize the most sensitive shorelines (with biological or human resources) for clean-up. Moreover, the oil distribution is usually non-uniform in the affected area which can be extensive. Therefore, having a detailed survey helps to minimize the problems related to logistics and accessibility (Lamarche et al., 2007). The SCAT process comprises the following elements:

- Collection of real-time survey data on shoreline oiling conditions, as well as shoreline and backshore character;
- Identification of environmental, cultural, and operational constraints to shoreline treatment;
- Recommendations regarding shoreline treatment priorities, criteria for the completion of the desired treatment, and treatment options;
- Monitoring of the treatment progress; and
- Working with stakeholders to ensure an agreement that sufficient treatment has been completed (ECCC, 2018).

Some of the information obtained by the SCAT program can be gathered and processed in advance (ECCC, 2018). While SCAT applies to the surveying of shorelines already affected by an oil spill, the pre-SCAT mapping process aims at collecting and assessing data before an incident

to support early response management and planning and help to reduce environmental impacts and make the response and cleanup efforts more efficient (Percy et al., 1997). Pre-SCAT data includes two main components: pre-SCAT mapping and pre-SCAT segmentation. The pre-SCAT shoreline segmentation is the process of the along-shore division into sections within which the shoreline characteristics are relatively homogeneous (ECCC, 2018). These characteristics include physical features, substrate type, wave exposure, and other factors that directly affect oil behavior and the choice of treatment options. In general, segments should be between 100 m and 1000 m in length (ECCC, 2018). The information pre-SCAT mapping dataset typically includes for each segment is described in Table 2.1.

Table 2.1. The elements of the Pre-SCAT mapping dataset

Pre-SCAT mapping dataset components	
Backshore character	The predominant coastal character within the shoreline segment, e.g., cliff/hill, sloped, flat/lowland, beach, delta, dune, lagoon, wetland, public road, agricultural field, parking lot, etc.
Shoreline character	Substrate materials and the morphology (form). The substrate classification is based on the grain size (diameter) of the sediment and includes: - boulder (>256mm); - cobble (64-256 mm); - pebble (4-64 mm); - granule (2-4 mm); - sand (0.125-2 mm); - silt (0.004-0.0625 mm); and - clay (0.00024-0.004 mm). Shore form can be represented by the beach, flat, cliff, bedrock ramp, bedrock platform, and terrace.
Oil behavior parameters	Description of tidal range, natural collection sites (e.g., debris, logs, traps), over wash potential, exposure to waves, intertidal/nearshore vegetation.
Access and Staging	Land, water, and air access equipment; Staging areas type and capacity; Boat ramps; Storage facilities; and Proximity to resources and operational support.
Response constraints	Ecological, biological, wildlife, archaeological, historical, cultural and subsistence, socio-economic, and other constraints.
Jurisdiction and ownership	Land ownership or management information including federal, provincial, municipal, commercial, private, first nations, agency, government, or personal contact information.
Auxiliary data	Photographs, video materials, and maps.
Response priorities	Sensitivity ranking based on ecological, cultural, and human use; Seasonal assessments (e.g., sediment accretion and erosion related to seasonal wave-energy levels); Remoteness; and Resources availability.

The 1989 surveys for the Exxon Valdez shoreline response operation in Alaska were carried out with few Geographical Information System (GIS) supporting tools and no recent aerial photographs or digitized shoreline maps. All navigation was carried out with the help of paper maps and charts. The maps for the area affected by the Exxon Valdez oil spill were not revised after an earthquake in 1964, which changed the shoreline in Prince William Sound significantly (Wiens, 2013). As the technology developed, videography became the principal source of information about physical and biotic characteristics. The use of videography for shoreline

mapping was explored during the development of the British Columbia Physical Shore-Zone Mapping System in 1979, and it was recognized as an efficient method to monitor shoreline characteristics, including morphology, substrate, and wave exposure (Howens et al., 1994). The development of GIS enabled a more effective and accurate assessment of shorelines. Today, audio commentaries and helicopter videography acquired at low altitudes can be transferred into a GIS, and Global Positioning System (GPS) waypoints are continuously obtained during the flight and subsequently overlaid onto the digitized vector layers (Owens & Sergy, 2004). This allows the association of video fragments with vector portions and furthers manual shoreline segmentation and classification.

There are several requirements for conducting efficient aerial surveys. According to the ECCC, aerial surveys should be taken with an altitude of 50-150 m and a ground speed of approximately 50-70 knots. The flight line should be around 200 m seaward from the water line. Also, the location of viewing targets should be ahead at approximately 45 degrees from the flight line, while the sun is preferred to be behind the video camera operator for best lighting (ECCC, 2018). Integrated audio commentaries provided descriptions of the coastline can be recorded to aid with interpretation (Wynja et al., 2014). The georeferenced videos are subsequently imported into the GIS software to be integrated with other geospatial information.

Although helicopter-based aerial surveys provide imagery at a very high spatial resolution capable of distinguishing finer substrate types (Anderson et al., 2012; Berry et al., 2001), there are several limitations of this method which including the following:

- Data acquisition and processing are expensive and time-consuming;
- Acquiring videography often faces logistical challenges related to weather and accessibility. Flights are usually limited to ideal weather conditions, low tides, as well

as the operational range of the helicopter. Fuel caching might be required as well in cases of dealing with remote locations where no or few refueling stations are available (Banks et al., 2014a); and

– The quality of the resulting maps directly depends on the experience of the videographer/interpreter (Lamarche et al., 2007).

Several shoreline classification systems designed for different purposes are currently in use. Commonly used shoreline classification schemes are included in the following programs: the Environmental Sensitivity Index (ESI) habitat mapping by National Oceanic and Atmospheric Administration (NOAA), the British Columbia Coastal Mapping Program (BCCMP), and ECCC SCAT shoreline classification mapping.

In general, shoreline classification used in the three above-mentioned programs is based primarily on a substrate character (material) and secondarily on shoreline morphology (form). Table 2.2 provides an overview of the shoreline categories used in these programs.

Table 2.2. Comparison of shoreline classification schemes

ECCC	NOAA	BCCMP
Bedrock	Exposed Rocky Shores Exposed Rocky Cliffs Exposed Wave-Cut Platforms Sheltered Rocky Shores	Rock Cliff, Narrow
		Rock Platform Wide/ Narrow
		Rock Ramp Wide/ Narrow
Sand beach/bank	Fine to Medium- Grained Sand Beaches Scarps and steep slopes in a sand Coarse-Grained Sand Beaches	Rock Ramp with Sand Beach Wide/ Narrow Rock Platform with Sand Beach Wide/ Narrow Rock Cliff with Sand Beach Sand Beach Sand/Mud Textures Sand Beach
Mud tidal flat	Exposed Tidal Flats Sheltered Tidal Flats Exposed scarps and steep slopes in clay	Mud Flat
Sand tidal flat	Exposed Tidal Flats Sheltered Tidal Flats	Sand Flat
Mixed and coarse sediment tidal flat	Exposed Tidal Flats Sheltered Tidal Flats Hypersaline tidal flats	Gravel Flat or Fan Sand and Gravel Flat or Fan
Mixed sediment beach/bank	Mixed Sand and Gravel Beaches	Rock Ramp with Sand and Gravel Beach Wide/ Narrow Rock Platform, with Sand and Gravel Beach Wide/ Narrow Rock Cliff with Sand and Gravel Beach Sand and Gravel Beach
Pebble/cobble beach/bank	Gravel Beaches Gravel Beaches (cobbles and boulders)	Rock Ramp with Gravel Beach Wide/ Narrow Rock Platform, with Gravel Beach Wide/ Narrow Rock Cliff with Gravel Beach Gravel Beach
Boulder beach/bank	Gravel Beaches (cobbles and boulders) Sheltered Rocky Rubble Shores	Gravel Beach
Man-made permeable	Riprap Sheltered Riprap	Man-made, Permeable
Man-made solid	Exposed, solid man-made structures	Man-made, impermeable
Marsh	Salt- and Brackish- Water Marshes Freshwater Marshes Swamps Shrub-Scrub Wetlands	Estuarine/Organics/ Fine
Peat shoreline	Peat shorelines	-
Ice-poor tundra cliff	Tundra Cliffs	-
Ice-rich tundra cliff	Tundra Cliffs	-
Inundated low-lying tundra	Inundated Low-Lying Tundra	-
Ice shelf	-	-
Snow	-	-
-	Vegetated low banks	-
-	Swamps	-
-	Scrub-shrub wetlands; Mangroves	-
-	-	Channels

NOAA uses 27 marine classes for Environmental Sensitivity Index (ESI) habitat mapping (NOAA, 2013) to provide a summary of coastal resources that are at risk in case of an oil spill. The shorelines are ranked based on their sensitivity to oiling. The resulting NOAA ESI maps integrate geographically-referenced biological and human-use resources with ESI-classified shorelines.

The BCCMP was developed to map the physical characteristics of the coastal zone. The scheme included 40 shore types that were designed to create an inventory dataset containing shore morphology, substrate, and wave exposure characteristics (Howens et al., 1994).

ECCC uses 24 SCAT classes for the description and documentation of oiled shorelines (ECCC, 2018). Example photographs of ECCC shoreline types are provided in Figure 2.1, while their detailed characteristics and corresponding oil response considerations are described in Table 2.3. This classification has been the common standard for the physical description of shoreline types, backshore types, coastal character, and substrate types for national oil spill response in Canada. For example, this classification scheme was used for the Emergency Spatial Pre-SCAT for Arctic Coastal Ecosystems (eSPACE) project initiated by Environment Canada in 2009. Detailed shoreline mapping for several Arctic study areas, including the Beaufort Sea–Mackenzie Delta channels–Banks Island, Resolute Bay, Victoria Strait, Hudson Bay, James Bay, and Labrador, was conducted through traditional helicopter videography (Wynja et al., 2014). Besides that, the use of satellites, including RADARSAT-2, SPOT-4 and -5, Landsat-5, for shoreline mapping was also explored (Banks et al., 2014b, 2014b, 2015; Demers et al., 2013) as a part of the eSpace program where the ECCC SCAT shoreline classification scheme was also adapted.

Figure 2.1. Photograph examples of SCAT shoreline types (Wynja et al., 2014)

Table 2.3. SCAT shoreline types characteristics and oil response considerations

SCAT Class	Description
Bedrock shorelines	Impermeable outcrops of consolidated native rock. They are divided into cliffs, ramps, and platforms. Cliffs are characterized by the slopes more than 35°; ramps slopes range from around 5° to 35°; and platforms have an overall slope of less than 5° (ECCC, 2016). Plants and animals usually accumulate in the intertidal zone, especially in cracks and crevices, which are protected from wave, wind, and ice actions. Oil often does not persist on bedrock cliffs as it is rapidly removed by wave action. However, in sheltered locations, heavy or weathered crude oils can persist for months to years because wave energy is too low to remove the oil naturally. The most appropriate response action on exposed high wave-energy coasts is natural recovery. However, sheltered coasts are not able to recover naturally, and the oil may persist for a long time. In this case, the other techniques, such as flooding, physical washing, hand-deployed vacuum systems, or dispersants, should be implemented depending on the type of stranded oil. Also, low- to high-pressure spraying at ambient water temperatures can be applied to remove fresh oils.
Sand beaches	Beaches are composed of sand with a grain-size diameter ranging from 0.0625 mm to 2.0 mm. Small amounts of granules, pebbles, cobbles, boulders, silts, or clay may also be present. The sand beaches are divided into coarse- and fine-sand beaches having grain diameters ranging from 0.5 mm to 2 mm and less than 0.5 mm, respectively (ECCC, 2016). The sand beaches are unstable and mobile as their surface easily changes under even slight wave actions. Therefore, the oil can be buried or mixed with the sand very quickly. Also, light and medium oils can readily penetrate coarse-sand beaches mixing with groundwater. Although the biological productivity of sand beaches is relatively low, these areas are often used as recreational facilities for people as well as resting or foraging habitats for birds. Also, organisms living in the beach sediment may die if oil concentrations in the interstitial water are high. These factors increase the sensitivity of sand beaches significantly. Oil can penetrate fine- to medium-grained sand up to 10-15 cm in depth. Fine- and medium-grained sand beaches are considered among the easiest to clean (NOAA, 2013). However, there is a high risk of the mixing of oil deeper into the sediments by vehicle movements and foot traffic. The treatment techniques depend on several factors, including the size of the oiled area, accessibility, time available for cleanup, and others. For example, manual removal is preferred when a little area is affected. However, with the increase of the oiled area size, the effectiveness of this technique decreases. Combinations of methods, such as flooding oil into trenches followed by recovery with vacuums or skimmers and mechanical removal followed by sediment relocation, are recommended.
Flats	Wide low angled (less than 5°) sloping surfaces of sediments are usually located near low-lying areas, lagoons, or estuaries. Mudflats contain very fine (smaller than 0.0625 mm in diameter) sediments, such as mud, silt, or clay. The grain size of sediment in sand flats ranges from 0.0625 to 2.0 mm in diameter (ECCC, 2016). Flats are often located in the lower intertidal zone in conjunction with marsh or boulder flats in the upper intertidal and supratidal zones. Since mud flats are usually water-saturated, the potential for natural penetration of oil is low. However, having a mobile surface layer, these sediments can be mixed with light oils. Mixed with subsurface sediments, oil can persist there for long periods. Also, oil can be moved deeper into the sediments through cracks in the mud or the holes of burrowing animals. Being very productive biological habitats for many burrowing animals (such as snails, worms, and clams) and birds, mudflats have a high sensitivity to spilled oil. Sand flats have lower biological productivity than mudflats but higher than sand beaches. Since there is a high risk of driving oil into the subsurface, there are limited options for the removal of oil from mudflat's shorelines. The preferred methods include herding, flooding or washing, and collection using sorbents or vacuums. Flooding or low-pressure ambient temperature water washing can be used to flush oil for on-water recovery. Disturbing sediment can have an impact of mixing oil into sediments. All movement of personnel and vehicles must be taken with caution.

[Continued on the next page]

Table 2.3. SCAT shoreline types characteristics and oil response considerations [continue]

SCAT Class	Description
Mixed sediment beaches & flats	Mixed sediment beaches and flats are composed of sand (with grains of 0.0625 to 2.0 mm in diameter) with a combination of granules (two to four mm in diameter), pebbles (4 to 64 mm in diameter), or cobble (64 to 256 mm in diameter) (ECCC, 2016). The surface layer usually consists of coarser sediments, while the subsurface contains predominantly sand. Oil penetration into the beach sediments may be up to 50 cm (NOAA, 2013). Also, the burial of oil may occur due to the mobility of sand fractures. The sensitivity of a mixed sediment beach to oil and treatment is low to medium as the coarse sediments support little life. The most common biota are burrowing or mobile species. A mixed sediment beach is similar to a sand beach in terms of penetration, retention, and persistence of oil. For example, as on sand beaches, light oils can readily penetrate medium- or coarse materials and mix with groundwater. However, the cleanup approaches are more similar to a pebble/cobble beach. Flushing techniques should be avoided as they can move the oil deeper into the sediments.
Pebble/ cobble beach	"Coarse sediment beach" consists of either pebble (four to 64 mm in diameter) or cobbles (64 to 256 mm in diameter), or a combination of both. The main difference between a pebble/cobble from mixed sediment beaches is the open interstitial spaces between individual pebbles or cobbles not filled with finer sediments. Similar to mixed sediment beaches, the oil sensitivity level ranges from low to medium. Pebble/cobble beaches are very permeable and have a dynamic and unstable surface layer. Therefore, the oil penetrates easily, especially when the particle size is large. The slopes on pebble/cobble beaches range from 5° to 35°, whereas the upper part of the intertidal zone usually has a steep slope, which hinders accessibility for cleanup vehicles. As with mixed sediment beaches, the main concern during the cleanup process is the excessive removal of sediment, which should be avoided because natural replacement rates are usually very slow and can take decades. Moreover, this technique can cause the beach to retreat or erode.
Boulder beach	An unconsolidated accumulation of boulders that are more than 256 mm in diameter in the shore zone. Boulder beaches are highly permeable and allow the oil to penetrate underlying sediments, which usually consist of pebbles and cobbles. This type of beach is stable and, therefore, provides habitats for biological growth, especially in more sheltered and shaded areas. Thus, biological productivity and sensitivity to oil can be relatively high, especially in the lowest parts of the beach, where the sediments are less mobile. The outer exposed surfaces of boulders usually cleaned using similar techniques used for a bedrock outcrop. However, the inner protected surfaces of the interstitial spaces are very difficult to access, limiting the oil removal options. In these cases, natural recovery is a preferred option. In most cases, mechanical removal is not practical. However, if this treatment technique is used, the boulders must be replaced with new boulders from other sites or the same cleaned boulders.
Man-made shorelines	Anthropogenic structures composed of either solid or permeable materials. Solid man-made structures include seawalls, groins, piers, port facilities, etc., while permeable features may consist of berms, bulkheads, cribwork, dikes, gabion, baskets, piers, rip-rap, etc. The surfaces of each of these materials are different in texture and roughness that affect the potential of oil to cling to them. For example, oil readily adheres to dry and rough surfaces; however, it does not stick to wet and smooth materials. Similar to the bedrock shorelines, oil is not left ashore on exposed areas, while it may persist for a long period on sheltered locations. Manmade structures usually are of great importance due to their frequent use by people or high social values. Thus, the treatment techniques depend not only on the type of material but the purpose of the structure itself. For example, for historic structures, only non-aggressive, labor-intensive manual methods are typically used. In the low human use areas, the option of natural recovery might be preferred. Physical washing can be efficient for oil removal from solid man-made shorelines.

[Continued on the next page]

Table 2.3. SCAT shoreline types characteristics and oil response considerations [continue]

SCAT Class	Description
Marsh	Marsh is a coastal zone that is covered at least once a month by salt or brackish water at high tide, and that supports significant (more than 15%) non-vascular, salt-tolerant plants such as grasses, rushes, reeds, and sedges. Saltwater marshes are common in sheltered wave-energy environments, such as estuaries, lagoons, deltas, or behind-barrier beaches (ECCC, 2016). Although the fine mud substrate prevents penetration, light oils can fill animal burrows and cracks. Also, oils easily adhere to the stems and leaves of vegetation. If so, the oil may persist for very long periods due to the low level of wave energy in these environments. Salt marshes are very sensitive to oil as they are extremely productive ecosystems and important to migratory birds, fish populations, and resident fauna. Salt marshes vary significantly in terms of physical and biological characteristics. Therefore, an individualized treatment plan should be implemented for each distinct marsh depending on substrate character, oiling conditions, species composition, time of year, size of the spill, type of oil, location, and others. Response activities should avoid the trampling of a marsh as it can drive the oil deeper into the sediments. Thus, it is recommended to use boats, boardwalks, or mats, as well as to limit the number of personnel. Sediment removal techniques are not recommended as they may result in oil mixing or disrupting the root systems. Low-pressure, ambient water washing is the preferred method that allows light- or medium-oil removal without causing damage. Sometimes, vegetation cutting or burning should be considered to lower the risk of sticky oil to marsh birds and animals. If burning is chosen, the protection of root systems by a layer of water should be ensured.
Peat	A spongy, compressible, fibrous material that forms from the incomplete decomposition of plant materials. The peat deposits may occur as a mat on a beach or a mobile slurry. This shoreline is usually located along low-lying and sheltered coastlines, which is where spilled oil is also likely to accumulate. Thick wide mats of suspended peat can occur in the water, forming peat slurry. If oil contact with slurry, it will be mixed and persist for a long time. Peat shorelines are potential bird-feeding areas. Preferred response options include natural recovery, flooding or washing, sorbents. Vacuum systems, combined with booms and skimmers, can also be used to recover deep and thick pools, but only in the areas without debris. If skimmers cannot be deployed, rope mops are used to recover oil in peat slurries. Sometimes, nets with a fine mesh are used to collect oil mixed in a peat slurry. Trampling vegetation and using heavy machinery should be avoided as this can cause deeper penetration of oil into the peat.
Tundra cliffs	An erosional feature present on Arctic coasts. Similar to bedrock cliffs, tundra cliffs have very narrow or absent beaches. Tundra cliffs are divided into ice-rich and ice-poor. Ice-rich tundra cliffs are composed of tundra mat, peat, and ice with relatively little sediment. Ice-poor tundra cliffs are unconsolidated sediment cliffs with an overlying surface layer of tundra vegetation and peat. Wave actions or thermal erosion of the cliff make the tundra and peat materials falling to the base of the cliff. Erosion rates vary from 0.5 m/year to 4.0 m/year depending on wave exposure level and the height of the cliff, which ranges from less than one m to ten m (ECCC, 2016). The potential of oil to stick to the exposed ground is low. However, if the peat contains slumped blocks, the oil may be collected in the spaces between the blocks. If the cliff is low, there is a risk of oil splashed over the cliff where it can persist for a while. Also, although exposed ground ice surfaces do not support plant life, the overlying tundra vegetation is composed of living plants and is sensitive to trampling and other disturbances. The behavior of oil and response options for ice-poor tundra cliffs are similar to sand, mixed sediment, or mud. Tundra cliffs are unstable, and there is always a risk of block falls, slumping, and mudflows due to natural erosion. Therefore, the primary concern during cleanup operations is the safety of personnel. Thus, natural recovery is the preferred response option in these environments. Techniques that can potentially cause additional erosion of the cliff face, such as low-pressure washing, are not recommended.

[Continued on the next page]

Table 2.3. SCAT shoreline types characteristics and oil response considerations [continue]

SCAT Class	Description
Inundated low-lying tundra shoreline	A very low-lying coastal tundra that is flooded by marine waters during spring high tides or wind-induced surges. These shorelines consist of vegetation in combination with peat mats, brackish lagoons, and small streams. While the vegetated soil of the tundra hinders the penetration of heavy oil, light oils can penetrate the soil, especially when the soil is dry. These shorelines have a high sensitivity to the oil spill as they are important bird habitats during the Arctic summer. Low-lying tundra shorelines are usually inaccessible or have limited access. Therefore, natural recovery is often the only option for treating oiling. In other cases, treatment techniques are similar to the ones for peat shorelines. For example, rope mops, as well as vacuum systems combined with booms and skimmers, may be used to recover mobile oil from the open areas without debris. Also, same as for peat shores, these shorelines are sensitive to trampling and vehicle traffic. These methods should be avoided as they can cause driving the oil more deeply into sediments.
Ice shelves	Impermeable surfaces of ice of glaciers reached the coast, or solid seasonal ice formed as a layer on the shore. In general, ice prevents oil from making contact with the shoreline substrate. The behavior of oil depends on the form of shoreline ice, its' texture, and the temperature of the air-ice boundary. For example, stranded on the shore-zone ice oil can be encapsulated within the ice during the freeze-up period. However, during a thaw cycle, oil does not adhere to the ice surface remaining on ice leads. Although marine mammals may use the ice shore to haul themselves out of the water, in general, ice surfaces do not support significant plant or animal life. Therefore, ice shorelines are not considered sensitive environments, and the most appropriate oil removal option in these areas is natural recovery. Other tactics that might be used for removing oil on shore-fast ice include flooding, washing from a boat or barge, high- and low-pressure warm/hot water washing, and others. Sometimes, manual removal of the oiled ice in combination with melting (and then the collection of the oil) or direct burning is implemented to minimize the accumulation of oil in remote areas.
Snow-covered shoreline	Any shoreline type with seasonal snow on top. The oil behavior on snow depends on various factors, including the character of the snow surface (fresh powder, wet slush, compacted, containing ice layers, etc.), the air temperature, and the surface character of the shore (i.e., flat or sloping). The snow layer itself is not considered to be a sensitive environment. When selecting oil removal tactics, the nature and sensitivity of the underlying sediment or bedrock substrates must be considered. Recovery tactics include natural recovery (for light oils that will evaporate during thaw periods), flooding or low-pressure ambient-water washing (if air temperatures are above freezing), manual removal with shovels and rakes (for small amounts of oil), burning (for remote areas), and others.

2.2 Land Cover Classification Using Satellite Remote Sensing

Dating back to the early 1970s, remote sensing technology has offered an opportunity to obtain accurate and timely environmental information covering extensive geographical areas in a cost-efficient manner. Nowadays, remote sensing products are used in a variety of applications, including climate change (Ouyang et al., 2014; Syed et al., 2010; J. Yang et al., 2013), natural hazard assessment (Dell'Acqua & Gamba, 2012; Giustarini et al., 2013; Yuri Fialko et al., 2005), biodiversity studies (Nagendra, 2001; Nagendra & Gadgil, 1999; Skidmore et al., 2015; Steven E. Franklin, 2010), land cover classification for monitoring of urban areas (Georganos et al., 2018; Qiu et al., 2020; Tavares et al., 2019), forest (Hansen et al., 2008, 2013; Myneni et al., 2007), agriculture (Alcantara et al., 2012; Lebourgeois et al., 2017; Segarra et al., 2020), and other environments (Guo et al., 2017; Leigh et al., 2014; Y. Wang, 2010).

The focus of this research is the land cover classification of the shoreline. Land cover mapping is a complicated process that depends on numerous factors, including satellite sensors and their spatial and spectral resolutions, input features, classification schemes, training and validation data, pre- and post-processing techniques, classification algorithms, etc. (Ma et al., 2017). The following subsections describe the most influential factors on the land cover classification results.

2.2.1 Satellite Sensor Characteristics

Remotely sensed data are obtained using passive or active sensors. Passive sensors rely on natural sources of electromagnetic radiation (EMR), e.g., the sun or the earth, with their infrared radiation, and record radiance reflected or emitted from an object on land. Most investigations in optical remote sensing are based on the identification of relationships between the amounts of reflected, emitted, or back-scattered energy in particular bands. Optical sensors have various

spectral resolutions, which refers to the number and size of bands in the electromagnetic spectrum to which the remote sensing instrument is sensitive (Jensen, 2016). In this context, the sensors can be divided into panchromatic, multispectral, or hyperspectral, which acquire data using one, several, or hundreds of spectral bands, respectively (Khorram et al., 2012).

Jiao et al. (2019) used China's Gaofen (GF)-5 hyperspectral satellite, Landsat-8, and Sentinel-2 multispectral data to investigate their difference in the classification performance for coastal wetlands mapping. The GF-5 data provided superior results for finer classification, while the classification based on Landsat-8 data achieved the lowest accuracy. Even though GF-5 data have the same spatial resolution as Landsat-8 (30 m), it has spectral advantages to the Landsat-8 data. Having numerous bands and narrow spectral range, hyperspectral sensors are able to obtain almost continuous spectral information of ground objects, which allow a significant improvement of the classification results. Jiao et al. (2019) found that the three satellites achieved similar results when the number of land cover types for classification was small, i.e., 13 classes. With the increase in the number of classes, Sentinel-2 and Landsat-8 data performance decreased compared to GF-5. The better performance of GF-5 was explained by the numerous narrow bands which were found capable of providing sufficient spectral information to classify coastal wetlands into 22 classes.

Multispectral data have been widely used for land cover classification. Since 2008, Landsat sensor data was available at no charge to users, and therefore, it has become the traditional choice as well as due to the wide geographic coverage and temporal depth of the archive (Gallant, 2015; Klemas, 2013). However, for a finer classification, multispectral data of higher spatial resolution is needed to be used. Lane et al. (2014) used a high spatial resolution WorldView-2 (WV-2) satellite, which provides imagery in eight spectral bands, including coastal, blue, green, yellow, red, red-edge, and two NIR bands. WV-2 with a high spatial resolution of two m produced a detailed classification of coastal wetlands into 22 classes with an overall accuracy (OA) of 86.5%.

(Laba et al., 2008) used 0.61-cm and 2.4-m QuickBird data to classify wetlands into 20 land cover types achieving an OA of 75%. Also, the use of Landsat sensor data might be inefficient for classification of coastal zones which are characterized by frequent clouds and continuous changes of tide levels. The moderate temporal resolution of 8–16 days for combined Landsat 7 and 8 often does not allow obtaining the images at the time with the lowest and highest tides.

Coastal zones often appear in narrow and patchy patterns, especially in the case of cliffs in Newfoundland. In this context, one of the major limitations of Landsat imagery is its spatial resolution of 30 m, which might be too low relative to the coastline width. Therefore, using Landsat imagery for shoreline classification may be insufficient, as the width of the coastline may appear to be less than one pixel (Jia et al., 2021; Saleem & Awange, 2019). Sentinel-2, which includes two identical sensors launched in June 2015 and March 2017, enhanced the mission of Landsat and SPOT (Kaplan & Avdan, 2017; Qunming Wang et al., 2017). Free access, global coverage, a wide-swath, high spatial resolution (10–60 m), the temporal resolution of five days, and multi-spectral (13 spectral bands) capabilities allow using the data for a wide range of applications, including land cover classification (Nivedita Priyadarshini et al., 2018; Thanh Noi & Kappas, 2018), wetland (Kaplan & Avdan, 2017), vegetation (T. Dong et al., 2020; Korhonen et al., 2017; Immitzer et al., 2016), urban mapping (X. Yang et al., 2017; Kopecka et al., 2017; Lefebvre et al., 2016), coastal waters monitoring (Hedley et al., 2018; Marzano et al., 2021), and others.

Sentinel-2 was also used for coastal area mapping. For example, Zhang et al. (2019) achieved the OA of 95.81% and 95.09% for coastal wetland classifications of the Yellow River Delta into eight classes and Jiaozhou Bay into seven classes, respectively. Jia et al. (2021) used the Sentinel-2 product for mapping tidal flats along China’s coastline. The authors classified China's coastal zone into four categories, including tidal flats, vegetation, water, and built-up. The authors produced a flat tidal map with an OA of 94%.

In contrast to optical sensors, radar systems emit their own EMR. The two types of imaging radars most commonly used are Real Aperture Radar (RAR) and Synthetic Aperture Radar (SAR). The azimuth resolution of RAR systems is determined by the antenna beam width and depends on the distance between the radar and the target. SAR systems coherently synthesize signals collected at different positions. It results in creating a large synthetic aperture with a narrow equivalent beam width and high-resolution imaging in azimuth (Jin, 2013).

One of the main drawbacks of optical sensors is the inability to penetrate through the clouds and collect data at night. The radio waves used in SAR typically range from approximately 3 cm up to a few meters in wavelength, which is much longer than the wavelength of visible and NIR light, typically used in making optical images. Table 2.4 describes some of the frequency bands used in remote sensing. For example, Sentinel-1 used in this research operates at C-band that utilizes the EMR from 3.75 to 7.5 cm in wavelength. Operating at longer wavelengths allows sensors to penetrate through clouds and collect the data day and night and in most weather conditions (Woodhouse, 2017). This is beneficial for coastal environment applications, which are perpetually covered in clouds.

Table 2.4. Characteristics of some of the microwave bands used in remote sensing

Band	**Frequency (GHz)**	**Wavelength (cm)**
P	0.3-1	30-100
L	1-2	15-30
S	2-4	7.5-15
C	4-8	3.8-7.5
X	8-12.5	2.4-3.8

Radar signals can be transmitted and received in various modes of polarization. Polarization is an index describing the characteristics of electromagnetic waves. It is used to express the orientation of the oscillation within the electric field of electromagnetic energy relative

to the direction of motion of the wave (Dwivedi, 2017). Conventional SAR systems transmit the signals in a plane polarization, horizontal (H) or vertical (V). Therefore, four different combinations of signal transmission and reception are possible. They refer to HH, VV, HV, and VH, where the first and second letters indicate the transmitted and received polarizations. Radar systems can have one, two, or all four of these polarization combinations. Besides that, there is a circular polarization where the electric field component rotates as the waves propagate.

Fully polarimetric SAR systems have shown great potential in identifying land cover types (Banks et al., 2015; Beijma et al., 2014; Cable et al., 2014; Corcoran et al., 2013). The parameters extracted using polarimetric decomposition were related to the physical properties of natural objects and useful for land cover mapping. For example, (Y. Chen et al., 2014) used fully polarimetric ALOS PALSAR data for land cover classification over coastal wetlands in Yancheng, China. Coastal and near-shore land cover types in the Beaufort Sea, Canada was also classified using Freeman–Durden and Cloude–Pottier decompositions applied to polarimetric RADARSAT-2 data (Banks et al., 2015). Parameters derived from Cloude–Pottier and Freeman–Durden decompositions extracted from RADARSAT-2 were also found to be supportive in conjunction with polarimetric response plots for land cover identification within the Great Lakes Basin of Canada (Cable et al., 2014).

While optical sensors provide data associated with reflectance and emissivity characteristics of objects, radar data contain information about structural, textural, and dielectric properties (Feng et al., 2019). The integration of data obtained from optical and radar sensors may achieve better classification results.

Corcoran et al. (2013) used multi-temporal and multi-source data, including the one obtained from Landsat 5 TM, RADARSAT-2, and ALOS-2 PALSAR, for coastal wetlands

classification in Northern Minnesota. Beijma et al. (2014) used combined S- and X-band quad-polarimetric airborne SAR, optical Landsat imagery, and elevation data to map coastal salt marsh vegetation habitats. Rodrigues et al. (2011) classified coastal wetlands in the Amazon in northern Brazil using Landsat-7, RADARSAT-1, and integrated data from both satellites. The accuracy obtained from the combined data was higher than the ones obtained from using optical or SAR data alone. These findings were in agreement with the Franklin et al. (2018) research, where integrated RADARSAT-2 and Landsat-8 product outperformed the individual bands of the sensors in the classification of the Hudson Bay Lowlands Ecoregion.

The successful implementation of the European Space Agency (ESA) Copernicus program allowed a synergistic utilization of freely available Sentinel-1 and Sentinel-2 datasets. Sentinel's optical and radar data were used together for mapping soil moisture (Hajj et al., 2017), wetland mapping (Chatziantoniou et al., 2017; Mahdianpari et al., 2019), crop mapping (Van Tricht et al., 2018), coastal land cover classification (Feng et al., 2019), and other applications.

2.2.2 Image Preprocessing

Image preprocessing techniques are intended to correct for sensors radiometric and geometric distortions of data and may improve the classification accuracy. Optical imagery often needs to be atmospherically corrected (Huang et al., 2008; C. Song et al., 2001). The presence of gases and aerosols in the atmosphere causes atmospheric effects, such as absorption and scattering, which affect the spectral radiance measured by the satellite. If sunlight is absorbed by the atmosphere, the sensor receives attenuated radiation. When sunlight is scattered, the radiation received by satellites may be increased or decreased depending on the atmospheric conditions. The atmospheric effect is a significant source of uncertainty in observing the land surface. Accurate atmospheric correction is an essential preprocessing step to improve satellite image quality for land surface property analyses.

Atmospheric correction aims to generate the estimates of radiation that is emitted and reflected at the surface (Thome et al., 1998). Several methods minimize the atmospheric effects, including relative and absolute radiometric corrections, single-image, and multiple-image normalization. Relative radiometric correction normalizes the intensities among different bands within a scene to remove detector-related problems. Then, the intensities are compared with a standard reference surface on the same date and same scene. Absolute radiometric correction uses the data about the solar zenith angle, the optical thickness caused by molecular scattering, the atmospheric transmittance for a given angle of incidence, the spectral irradiance at the top of the atmosphere, and the Rayleigh and Mie scattering. Single-image normalization is based on the assumption that infrared data are less affected by atmospheric scattering effects than visible. The histogram shifts due to haze are used to adjust for the atmospheric effects. This method involves a subtractive bias established for each band. Multiple image normalization uses regression analysis for several dates and is used mainly for change detection purposes (Khorram et al., 2012).

Raw SAR data needs to be calibrated to provide imagery in which the pixel values can be directly related to the radar backscatter of the scene. In other words, calibration allows converting the radar reflectivity into physical units. For example, radar reflectivity may be transformed into Beta Naught β° , where the area normalization is aligned with the slant range; Sigma Naught σ°, where the area normalization is aligned with the ground range plane; and Gamma γ° , where the area normalization is aligned with a plane perpendicular to the slant range (ESA, 2015; Small et al., 2009).

Despite the SAR advantages mentioned in previous section, SAR images contain speckle noise. This noise appears from coherent interference of backscattered radar echoes. The effect of speckle can be removed at the expense of spatial resolution. Many techniques, including Lee,

Kuan, Frost, Gamma MAP, and other speckle filters, can be used to reduce speckle noise (Yommy et al., 2015). Speckle removal methods aim to decrease speckle noise without losing information about the edges, texture, and other object features (Zhong et al., 2009). The effect of speckle filtering often depends on the selected window size. For example, if the window size is too small, the speckle will not be removed. A too-large window size may blur the edges and reduce the contrast between the objects (Lee et al., 1999).

Spatial low pass or smoothing filters are often applied to SAR and optical data to decrease intra-class variability and random noise (Tøttrup, 2004). Pan-sharpening is used to generate a higher spatial resolution multi-spectral image by combining a high-resolution panchromatic image and a low-resolution multispectral image (Mitchell, 2010). For example, (Ranson et al., 2001) investigated the effects of topography on forest classification in mountainous terrain. It was found that radiometric correction improved classification accuracy significantly. Radiometric correction methods are used for the reduction of slope-aspect effects in optical satellite imagery. For example, Meyer et al. (1993) found that the accuracy in a forest type classification was improved by 10% to 30% after applying the radiometric correction.

2.2.3 Feature Extraction

The results of a land cover classification directly depend on the input variables. Besides the original optical or radar bands, additional predictor variables can be generated by applying image transforms, such as spectral indices, band ratios, texture measures, and principal component analysis (PCA).

The extraction of spectral indices and the band ratio technique are the methods of multi-spectral transformation (Bouzekri et al., 2015). These methods allow the suppression in topographic variation and enhance the spectral difference between bands (Rajendran et al., 2012).

In a simple way, these methods are applied by dividing the digital number (DN) values of one band by the values of another, creating a new gray-scale image with relative band intensities (Gabr et al., 2015).

Spectral indices are often used as additional explanatory variables to improve the classification (Dash et al., 2007). Indices are calculated through arithmetic combinations of different spectral bands.

Spectral indices have been widely used to analyze and monitor temporal and spatial variations of different surface type characteristics. For example, vegetation conditions are usually monitored using the indices generated from the data collected in the Visible and Near-Infrared (VNIR) regions (Jiang et al., 2006). The Normalized Difference Vegetation Index (NDVI) is built on the pigment absorption feature in the red and NIR regions of the electromagnetic spectrum. This index has been widely used to estimate various properties of vegetation (Chuvieco et al., 2004; Gamon et al., 1993; Yengoh et al., 2016). To monitor the spatial distribution of urban built-up areas, the difference between the values in NIR and Mid-infrared (MIR) bands is used (Zha et al., 2003), while the normalized difference between the BV in green and NIR bands is useful to identify water bodies (McFeeters, 1996).

Satellite-derived data often contain images having similar information. As a result, an inter-band correlation problem occurs during multispectral image processing (Lillesand & Kiefer, 2000). PCA is designed to address this problem. PCA is an image transformation technique that increases interpretability while reducing dimensionality with minimal loss of information. The data are reduced through their geometrical projection onto lower dimensions called principal components (PCs) (Crósta & Moore, 1988; Jolliffe & Cadima, 2016; Lever et al., 2017). The algorithm utilizes an orthogonal transformation to transform the original dataset into a new space

of linearly uncorrelated attributes. During the eigenvalue decomposition of a correlation matrix, the eigenvector of the highest eigenvalue captures the largest possible information in the dataset. Then, the algorithm selects the subset that contains the most informative eigenvectors. It results in creating the dataset with a lower-dimensional space where every data sample of the original image is represented by a smaller feature vector (Dinç et al., 2014).

PCA is a widely accepted transformation technique that has proven to be of great value for multispectral data analysis (Pan et al., 2019). It is worth noting that principal components are not correlated with each other. Moreover, they can reduce image noise and improve data representation (Pan et al., 2019). However, since the PCA is an unsupervised transformation method, the resulting new feature set is not interpretable.

During the visual interpretation process, humans perceive different factors simultaneously. They include not only spectral information but the texture, edges, context, geometry, size, brightness, etc. Thus, many researchers try to incorporate multiple characteristics into the image classification process (Jensen, 2016). The texture is considered one of the most valuable characteristics used to extract meaningful information for different purposes (Haralick et al., 1973).

The texture is the frequency of tonal change on an image and provides the information of object characteristics, such as smoothness, coarseness, or regularity (Gonzalez & Woods, 1992; Lillesand & Kiefer, 2000). For example, a visually smooth texture may be found over the image area with only slight changes in DN values, while a visually coarse texture is determined by the presence of abrupt changes in DN values (Coburn & Roberts, 2004).

The incorporation of texture is a popular technique for classification improvement (Coburn & Roberts, 2004). Although the textural features are expected to be more useful when analyzing

SAR images, the effectiveness of textures in optical imagery was demonstrated in many applications, such as discriminating urban environments (Dell'Acqua & Gamba, 2006), evaluation of the biomass of various forest types (Singh et al., 2014), and burn scars detection (Smith et al., 2010). It was found that the texture provides information that is independent of spectral reflectance values (Hall-Beyer, 2016). Therefore, incorporating texture allows the improvement of results regardless of the chosen algorithm (Marceau et al., 1990; Presutti et al., 2001; Lu et al., 2008).

There are several approaches to texture processing. In general, they can be grouped based on the statistics texture measures that have been derived: first-order statistics, second-order statistics, or semi-variogram (Jensen, 2016). First-order statistics of local areas include a mean, variance, skewness, kurtosis, minimum and maximum, etc. This category also includes some more complex metrics, such as Moran's I spatial autocorrelation, which is calculated based on the weighted deviations of brightness values (BV) from their mean in the local window (Purkis et al., 2006).

The most commonly used texture measures are those derived from the Grey Level Co-occurrence Matrix (GLCM), which was proposed by Haralick et al. (1973). The GLCM defines the joint occurrence frequency of the two values i and j for a pixel pair within a neighborhood, normalized to probabilities. Many second-order statistical properties can be calculated from the GLCM. Initially, Haralick et al. (1973) proposed 28 different measures. Ten of them were widely adopted by the remote sensing community and are often used in image processing applications. Texture attributes computed from the GLCM may be divided into three groups according to the purpose of the weights in the equations: contrast, orderliness, and statistics (Eichkitz et al., 2013). The Contrast group measures include contrast (CON), dissimilarity (DISS), and homogeneity (HOM). They are calculated using weights related to the distance from the GLCM diagonal. Orderliness group measurements, including Angular Second Moment (ASM), Energy (E),

Maximum (MAX), and Entropy (ENT), show how regular the pixel values are within the window (Hall-Beyer, 2007). The statistics group includes the measures of mean, variance (VAR), and correlation (COR) derived from GLCM. Mean and VAR related to the spectral heterogeneity of the image, while COR measures the linear dependency of grey levels between neighboring pixels (or predictability of pixel relationships).

The GLCM method for texture extraction has been successfully tested for many applications, including land-cover mapping in coastal (Su & Gibeaut, 2017), urban (Herold et al., 2003), forested (Kayitakire et al., 2006; Tuominen & Pekkarinen, 2005) and other environments.

Lane et al. (2014) computed six GLCM texture measures, including HOM, CON, DISS, ENT, ASM, and CORR, from the WV-2 NIR-1 band. They found that the HOM texture variable provided the greatest discrimination between coastal wetland types. Coarse texture indicated by low HOM values was associated with shrub-scrub habitats, where tree leaves, leaf shadows, and interspersed grasses created a high variation of the reflectance intensity within local neighborhoods. In contrast, smooth texture indicated by large HOM values was associated with calm water bodies and aquatic beds with submerged vascular vegetation. Most herbaceous habitats were found to have relatively smooth textures due to the similarity of plant species and their heights within local neighborhoods.

GLCM was also used to extract vegetation information and investigate the land cover change dynamics of Mediterranean coastal wetlands (Berberoğlu et al., 2010). Jiao et al. (2019) implemented four measures of GLCM texture features, including entropy, homogeneity, contrast, dissimilarity, and correlation for mapping coastal wetlands. Wang et al. (2018) assessed vegetation classification using high spatial resolution Pléiades satellite imagery in the central zone of Yancheng National Natural Reservation (YNNR) in Jiangsu, China. The results obtained by using

the high spatial resolution Pléiades spectral data alone and spectral data combined with GLCM texture features were compared. Mean, variance, ASM, entropy, and contrast were tested in the 3 × 3, 5 × 5, 7 × 7, and 9 × 9 window sizes, whereas mean, ASM, and entropy were superior in the vegetation classification. The authors found the improvement of the overall accuracy of vegetation classification about 6.50% from 76.27% to 82.87% with the additional use of GLCM texture features.

The performance of classification can be enhanced by the incorporation of other ancillary data, such as a Digital Elevation Model (DEM) and its derivatives, geological layers, and data from other sensors (Geerling et al., 2007; Hoshikawa & Umezaki, 2014; Ricchetti, 2000; Sluiter & Pebesma, 2010). When multi-temporal imagery is used, the classification is applied to a fusion of images captured at different times from the same site (Persson et al., 2018; Schultz et al., 2015). For example, (Persson et al., 2018) achieved the highest overall accuracy of 88.2% for three species classification using the four image datasets, while the classification of a single image produced the map with an OA of 80.5%.

In most cases, multiple techniques are used. For example, Tøttrup (2004) achieved the highest accuracy for tropical forest classification when using pre-classification image smoothing and multi-date imagery. Ranson (2001) reached the best classification when applying radiometric correction using a DEM, extracting band ratios, and implementing PCA. Lane et al. (2014) improved the coastal wetland classification accuracy from 79% to 86.5% by incorporation of additional bands and features, including yellow, red-edge, NIR-2, coastal bands, NDVI, and texture, with commonly used WV-2 VNIR bands.

2.2.4 Image Classification

The choice of an appropriate classification algorithm is one of the most important influential factors for supervised classification (Ma et al., 2017). It was proven that different classification techniques lead to different results (McInerney & Nieuwenhuis, 2009; Pal, 2005; X. Song et al., 2012). The classification methods can be grouped in different ways. For example, they can be divided into pixel-based (PB) and object-based (OB) algorithms and parametric and non-parametric methods. The description of these methods is provided in this section.

Pixel-based (also called "per-pixel") classification has long been the most common approach in the past (Belgiu & Csillik, 2018; Hussain et al., 2013; Myint et al., 2011). However, with the development of sensors able to produce finer resolution data, it was found that the per-pixel algorithms were not always capable of extracting the desired information and resulted in low accuracy caused by pixel heterogeneity, mixed pixels, and spectral similarity of some features (Peña-Barragán et al., 2011). For example, in optical remote sensing, the single-pixel approach utilizes only spectral information in each pixel. Thus, this method fails when objects have similar spectral characteristics (Herold et al., 2003; Rejaur Rahman & Saha, 2008). Another factor that negatively affects the results of the per-pixel method is that the pixel value forms not only from the signal coming from the land region represented by this pixel but from the surrounding areas. Therefore, many researchers started to develop methods that take into account not only information from a single pixel, but its surrounding pixels. In addition to that not only spectral parameters but also spatial parameters, such as size, shape, and texture, started to be included in the analysis (Jensen, 2016).

The Object-Based Image Analysis (OBIA) method enables the use of both spectral and spatial information and relationships between the image objects (Blaschke, 2010). OBIA is an iterative method with two primary steps. The imagery is first divided into segments (or "image

objects”), defined as individual regions with similar shape and spectral characteristics (Blaschke, 2010; Blaschke et al., 2014). The resulting objects are subsequently classified using various supervised or unsupervised classification approaches (Hay & Castilla, n.d.).

Many researchers have reported superior results obtained from the OBIA method pixel-based approaches (Belgiu & Csillik, 2018; Castillejo-González et al., 2009; Lebourgeois et al., 2017; Ma et al., 2017; Pu et al., 2011; Yan et al., 2006). Besides improved accuracy, OBIA reduces noise effects, which are common in pixel-based classification methods (Liu & Xia, 2010; Whiteside et al., 2011), making the final classification map easier for interpretation and decision-making.

There are several segmentation algorithms, which can be broadly grouped into three categories: pixel-based, edge-based, and region-based (Tian & Chen, 2007). The pixel-based algorithm groups pixels into objects by thresholding (Mardia & Hainsworth, 1988). The edge-based segmentation approach identifies edges between regions based on contrast characteristics and links them into contours to represent the boundaries of objects (Moigne & Tilton, 1995). Region-based segmentation is based on detecting homogeneous parts of images (S.-Y. Chen et al., 1991; Moigne & Tilton, 1995).

Multi-resolution segmentation (MRS) proposed by Baatz & Schäpe (2000) is a bottom-up region-based technique that merges smaller objects into bigger ones. This algorithm implements a local optimization process starting at any point in the image with one-pixel objects. The segments grow simultaneously over the whole scene so that adjacent image objects are of similar size and comparable scale. The segmentation results depend on the user-defined parameters, such as scale, shape, and compactness. The objects have a square shape when higher values are set up for shape and compactness parameters. The scale parameter defines the maximum standard deviation of the

homogeneity criteria with regard to the weighted image layers for generating image objects. In general, smaller values of the scale parameter produce relatively smaller image objects, while greater values produce the larger average size objects. When the smallest growth exceeds the defined scale parameter, the process stops (Benz et al., 2004). An MRS algorithm was widely and successfully used by many researchers (Al-Khudhairy et al., 2005; Myint et al., 2011; Novelli et al., 2016; Wenxia Wei et al., 2005; Zhou & Troy, 2008).

The OBIA approach was assessed in several studies for shoreline classification. For instance, Demers et al. (2013) applied OBIA to develop a classification scheme using combined data obtained from RADARSAT-2, SPOT-4/-5, and a DEM, achieving an overall accuracy of 75%. Demers et al. (2015) compared the per-pixel and object-based methods for shoreline classification in two sites located in the Western Arctic along the Beaufort Sea coastline. The classification was done using RADARSAT-2, SPOT-4/-5, and DEM data. The author noted that the shoreline features on the map obtained from OBIA are clearly visible and better represented than on the map obtained from the pixel-based classification. Also, it was observed that the OBIA approach provides more flexibility allowing the researcher to modify the classification easily.

Numerous pattern recognition techniques have been developed for satellite-based image classification (Lu & Weng, 2007; Schowengerdt & Schowengerdt, 2006). The classification algorithms may be grouped into parametric and non-parametric. The choice of a particular classifier relies on the nature of the data. Parametric algorithms assume that all samples are derived from populations with well-defined statistical distributions, while non-parametric techniques make no such assumptions.

A widely-used parametric algorithm for land cover classification is the maximum likelihood (ML) (Ali et al., 2018; Banks et al., 2014a; Z. Chen et al., 2017). An ML algorithm is

based on Bayes' theorem and requires an assumption of the normal distribution of samples in each class (Duda et al., 2012). If the dataset meets this assumption, the ML is the optimal choice (Kavzoglu & Reis, 2008). The ML decision rule is based on the multivariate probability density function. The ML algorithm assigns each pixel with measurements X to the class i whose units are most probable to give rise to the feature vector X. In other words, the probability of a pixel belonging to each predefined set of m classes is calculated, and then, the pixel is assigned to the class in which the probability is the highest (Jensen, 2016).

There are many non-parametric classifiers, e.g., K-nearest neighbor (KNN), support vector machine (SVM), decision tree (DT), Random Forest (RF), and other algorithms. KNN belongs to the group of the nearest neighbor classifiers, which assign a pixel to a class based on the Euclidian distance from that pixel to the nearest training data pixel in n −dimensional feature space (Schowengerdt & Schowengerdt, 2006). For KNN, a user defines the k-parameter which is the number of training pixels. Thus, the algorithm searches away from the pixel to be classified in all directions until it meets k pixels. Then, the pixel is assigned to the class with the majority of pixels encountered. The traditional KNN classifier was the most popular among the ones used in OBIA approach. However, from 2011, SVM and RF classifiers attracted great attention of many researchers due to the high performance of these algorithms (Ma et al., 2017).

The SVM is a powerful technique for classification and regression problems based on a statistical learning theory (Vapnik, 2000). The basic idea of support vector machines for pattern classification is to construct an optimal hyperplane using a training sample subset to act as the support vectors and maximize the margin of separation. In other words, the SVM classifier finds the support vectors and the separation hyperplane for each pair of classes. It allows for the maximization of the margin between classes. It also provides a powerfully modern supervised

classification method that does not require an assumption of a normal distribution of data and needs many fewer samples than traditional MLC (Y. Wang, 2010).

Some researchers found the superior performance of the SVM algorithm over traditional ML, minimum distance, and parallelepiped classifiers (Mountrakis et al., 2011), as well as over the advanced classifiers, such as Classification and Regression Trees (CART) and RF (Foody & Mathur, 2004; Nitze et al., 2012; Shao & Lunetta, 2012).

Decision tree (DT) methods constitute another category of non-parametric pattern recognition techniques. In contrast to traditional statistical methods like KNN, which use all feature space covariates simultaneously, the DT methods are based on the partitioning of the dataset by constructing the chain of decisions.

One of the most well-known DT classification algorithms is Classification and Regression Trees, which splits the training data into smaller sub-sets based on an attribute value test. The subsets created by the splits are called nodes. The subsets that are not split are called terminal nodes assigned to classes (Breiman et al., 1984). As a result, CART constructs a binary decision tree with homogeneous and pure nodes (Simioni et al., 2018). The complexity of the model is defined by the parameters of the maximum depth and the number of child nodes. In general, the larger depth, the more complex the decision tree and the greater potential to achieve a higher classification accuracy. However, if too many nodes are created, the model may become over-fitted (Qian et al., 2015). Pruning techniques are often used to reduce the likelihood of overfitting. Pruning allows reducing the size of decision trees by trimming the parts of the tree that do not provide power for the classification.

The random forest (RF) classifier, developed by Breiman (2001a), uses a group of decision trees instead of one decision tree, which leads to improved classification results (Polikar, 2006).

Each decision tree is constructed using a sample with replacement from the training data using the bagging approach. The sample contains around 64% of instances, which appear in this sample at least one time. These instances are also called “in-bag instances.” The other 36% of instances remain “out-of-bag” (Fawagreh et al., 2014). When a large number of decision trees is generated, the most popular class is determined for each pixel via a majority voting procedure based on the votes obtained from the decision trees (Breiman, 2001a).

The RF classifier has demonstrated its ability to increase the quality of land cover maps in various applications (Belgiu & Drăguţ, 2016; Hao et al., 2015; Novelli et al., 2016; Pelletier et al., 2016). For example, Zhang et al. (2019) achieved 94.78% OA for in Yellow River Delta wetland classification using RF, while the OA of 67.09 % was obtained by using SVM. Moreover, the RF performance's computational time is considerably lower compared to other classifiers such as DT or SVM (Pelletier et al., 2016). However, it is worth noting that the accuracy and computational time depend on the number of input features.

In general, RF was found to be most suitable for OBIA and found to achieve the highest mean classification accuracy, followed by the SVM and the DT classifiers (Li et al., 2016; Ma et al., 2017). Moreover, it was suggested that RF was less affected by the redundant data than other algorithms, including SVM (Li et al., 2016). Breiman (2001) identifies the following advantages of the RF algorithm: robustness to outliers and noise, fast speed of processing, the ability to generate valuable estimates of error, strength, and correlation. Last but not least, RF also provides information on the importance of the variables, which can be used as a means of feature selection and weighting of explanatory variables. Considering all these advantages of the RF, this algorithm was chosen to classify shoreline types in this study. The implementation of the RF allowed us to use highly dimensional data from a variety of sources, including the satellite data obtained from Sentinal-1 and -2 and DEM, achieving a considerably high overall accuracy.

2.3 Satellite-Based Shoreline Classification

Most of the work on shoreline classification was done through the traditional manual interpretation of helicopter videography. The most extensive work to classify the Canadian Arctic shoreline using helicopter videography was done by Wynja (2014). As a result of this work, the coastal information of the following regions has been mapped: the Beaufort Sea region, Resolute Bay, Victoria Strait, Hudson Bay, James Bay, and the Labrador coast. However, realizing the limitations of the helicopter videography method as related to time processing, financial expenses, and logistics, several studies were conducted as a part of the eSPACE project to assess the potential of satellite images to classify coastal land types (Z. Chen et al., 2017; Banks et al., 2015; Demers et al., 2015; Banks et al., 2014a, 2014b; Demers et al., 2013).

Satellite imagery has been used to map a variety of shoreline features (Brebbia, 2008). Satellite-based methods are becoming more successful as sensors are being developed with greater capabilities, and the data is getting to be more easily and widely accessible. The development of an automated algorithm to process satellite data would allow for a more cost- and time-effectively mapping, covering larger areas in comparison with the one conducted by the traditional helicopter videography method.

Only a few studies assessed the potential of satellite data for shoreline sensitivity mapping. The majority of these studies were done for the Canadian coastline. These studies are summarized in Table 2.2 and discussed in this chapter.

Banks et al. (2014a) focused on assessing the potential of using radar imagery for mapping coastal and near-shore land cover types. The images obtained from RADARSAT-2 were used as the main dataset. Various image acquisition parameters, including incidence angle and polarization, were explored to determine the most optimal for shoreline classification. Besides the

RADARSAT data, pan-sharpened SPOT-4 spectral bands were tested to investigate the potential of using multidimensional data for the improvement in classification results.

Table 2.5. Satellite-based shoreline classification studies over the Canadian coastline

Article	Sensor	Number of classes	Study area	Classifier	Input variables	OA
(Banks et al., 2014a)	RADARSAT-2 SPOT-4	16	West Point, Richard Island, Beaufort Sea, NWT Tuktoyaktuk Harbour, Beaufort Sea, NWT	PB MLC	Shallow angle HH, HV, and VV backscatter values	52.9% and 59.1%
					Shallow angle HH, HV, and VV backscatter values; green, red, NIR, and MID bands	86.1% and 76.2%
					green, red, NIR, and MID bands	82.5% and 59.1%
(Banks et al., 2014b)	RADARSAT-2	16	West Point, Richard Island, Beaufort Sea, NWT Tuktoyaktuk Harbour, Beaufort Sea, NWT	Unsupervised polarimetric SAR classifiers: Wishart-entropy/alpha, Wishart-entropy/anisotropy/alpha, Freeman-Wishart	Shallow, medium, and steep incidence angle SLC fine Quad- Pol images	OA was not assessed
(Demers et al., 2015)	RADARSAT-2, Spot 4-5	9	Richards Island, NWT Ivvavik, Yukon Territory	PB MLC	FQ15, FQ30, green, red, NIR, and SWIR bands; slope grid	73% and 73%
				OB hierarchical classification		74% and 63%

[Continued on the next page]

Table 2.5. Satellite-based shoreline classification studies over the Canadian coastline [continue]

Article	Sensor	Number of classes	Study area	Classifier	Input variables	OA
(Banks et al., 2015)	RADARSAT-2 Landsat-5	7	Dease Strait, Coronation Gulf, and Bathurst Inlet, NU	RF	Green, Red, NIR, SWIR-1 and -2, NDVI; Freeman-Durden decompositions: double-bounce and volume scattering; Touzi Decomposition: secondary and tertiary eigenvalues HV Intensity, DEM and Slope	91%
(Z. Chen et al., 2017)	Pléiades-HR	9	Tuktoyaktuk Harbour, Beaufort Sea, NWT	P-B MLC	PAN, red, green, blue, IR NDVI, NDWI, DEM, slope	87%
				P-B RF		81%
				O-B MLC		86%
				O-B RF		88%

The authors conducted a deep analysis of the backscatter characteristics of various shoreline types and found that a larger difference in incident angle affects backscatter substantially. Shallow angle images were found to be the most useful for interclass separability. However, other features, which could be extracted from SAR data (e.g., texture or band ratios), were not investigated, and only backscatter values were used as an input. As a result, the use of SAR data alone provided the worst OA (52.9% and 59.15%) in comparison with the accuracies obtained when only SPOT-4 data was used (82.5% and 59.1%) or when the combination of SPOT-4 and RADARSAT-2 data was used (86.1% and 76.2%). Moreover, focusing on assessing the RADARSAT potential, Banks (2014a) did not analyze the spectral characteristics of SPOT-4 data. However, the extraction of spectral indices and their incorporation in the classification process might improve the results significantly.

Banks et al. (2014b) applied unsupervised polarimetric SAR classifiers, namely Wishart-entropy/alpha, to improve an understanding of the scattering behavior of coastal land covers at various incidence angles Wishart-entropy/anisotropy/alpha, and Freeman-Wishart to Fine Quad-Pol RADARSAT-2 data. The OA was not assessed in this study. Instead, the results were evaluated through the analysis of whether the obtained clusters represented particular shoreline features. The results demonstrated a greater potential of shallow and medium angles data for class discrimination, which agreed with the previous study (Banks et al., 2014a). The results of this study are useful to improve the understanding of which SAR data features are the most useful for shoreline classification. However, the effect of using features must also be compared when used in combination with other data, including optical images and a DEM. The integration of radar and optical data might be beneficial as these sensors contain different information: optical sensors collect data associated with reflectance and emissivity, while radar data provide structural, textural,

and dielectric characteristics of land objects (Feng et al., 2019). For example, Demersh et al. (2015) developed a classification scheme using combined data obtained from multiple sources. Based on the findings from Banks et al. (2014a and 2014b), Demersh et al. (2015) used medium-to-shallow incidence angles Fine-Quad (FQ) fully polarimetric RADARSAT-2 data along with SPOT-4/-5 and slope grid data for a supervised classification. Aiming to assess the pixel-based (P-B) and object-based (O-B) algorithms for shoreline classification, MLC and hierarchical classification were applied. Although researchers compared the results obtained from P-B and O-B approaches, it is worth noting that the input parameters varied both between the methods and between the two study areas. For example, the standard deviation VV feature and the mean SPOT NIR band were used to classify the study areas at Ivvavik. However, these features were not used for the classification in the Richard Island area. Also, the resolutions of slope grid data were different in each study (30 m and 40 m). These factors indicate the absence of consistency in the classifications in this research.

The resolutions of DEMs used in Demers et al. (2015) were low, 30m and 40 m. However, accurate elevation data are essential for coastal mapping, especially in the Arctic, where the coastal zone is usually narrow. As a result of using the slope grid with coarse resolution, jagged edges at the land-water interface appeared in the final map obtained by P-B classification.

Besides an assessment of different classification algorithms, Demers et al. (2015) explored the potential for classifier transferability by applying classification models trained on data from the Richards Island site to the Ivvavik site. The overall accuracy of 71% and 78% for the pixel- and object-based methods demonstrated the ability to classify shore classes using satellite data, allowing for the creation of the classification map along the whole Canadian coastline in the future. However, Demers et al. (2015) also formulated one of the main obstacles of using satellite imagery

for shoreline mapping which was the low probability of acquiring the data from multiple sources during the low tide period. This obstacle is critical as the shoreline classification focuses on intertidal zone, which is open during the low tide.

The highest shoreline classification OA results were achieved by Banks et al. (2015). The RF Forest algorithm was used to classify the shoreline along the Dease Strait, Coronation Gulf, and Bathurst Inlet, Nunavut. Multiple RADARSAT-2 and Landsat 5 images were used along with the DEM data. Forty-nine predictor variables were analyzed, whereas only 14 of them were used in the final classification. The most important variables included Landsat-5 Green, Red, NIR, SWIR-1, SWIR-2 bands, NDVI values, Freeman-Durden double bounce and volume scattering, pedestal height, and secondary and tertiary eigenvalues of the Touzi decomposition, HV intensity, DEM values, and slope. The optimized model reached an OA accuracy of 91%, classifying the shoreline into seven types, demonstrating the ability to classify coastal land cover types at acceptable levels. However, although the authors noted that optical data are the most important for the classification, only seven variables extracted from the Landsat-5 data were analyzed. These variables were the six spectral bands and NDVI. The effects of other spectral indices, texture measures, or Principal Components (PCs) were not assessed.

One of the main limitations of all previously discussed papers is the use of low- or medium-resolution satellite images, which leads to misclassification between the coastal land covers. Chen et al. (2017) used very high-resolution optical Pléiades satellite imagery to classify the shoreline of Tuktoyaktuk Harbour (same study areas as in Banks et al. (2014b, 2014a)), applying a hybrid object-based approach which included semi-automatic water/land separation, texture analysis based on local binary pattern (LBP), and RF classification.

Although the resolution of panchromatic and spectral bands is very high (0.5 m and 2 m, respectively), the obtained OA was 88%, which is only 2% higher than obtained by Banks et al. (2014a) using RADARSAT-2 and SPOT-4 data. Moreover, Chen et al. (2017) classified the shore into seven classes, while the number of classes used by Banks et al. (2014a) is 16. Since the classification accuracy decreases with an increase in the number of classes (Ma et al., 2017), the statement that the Pléiades High Resolution (HR) optical imagery provided more accurate information about the shore types was questionable. The accuracy was not significantly improved when using the higher resolution data. The Pléiades HR satellite provides images only in panchromatic and four spectral bands, including the blue, green, red, and IR. The lack of other bands outside the visible spectrum does not allow the construction of many spectral indices that might improve the separability between the classes.

The major limitation of most of the studies discussed above is shoreline width relative to image resolution. Therefore, providing such detailed discrimination of classes following the SCAT methodology is not possible. The more general classes had to be adapted from the SCAT classes to avoid interclass confusion, which might be caused by the lower spatial resolution of satellite imagery in comparison to helicopter videography. For example, Demers et al. (2015) combined the Sand beach/flat, Mud tidal flat, and Mixed fine sediment beach/tidal flat into Fine sediment class; while Pebble/Cobble beach, Boulder beach or bank, mixed coarse sediment tidal flat were merged into Coarse sediment class. As a result, there was no consistency in the number of shoreline classes between the studies. For instance, the number of classes in Banks et al. (2015), Chen et al. (2017), and Banks et al. (2014) were 7, 9, and 18, respectively. The number of classes that can be extracted from satellite data depends on the spatial and spectral characteristics of the sensor and the nature of the shoreline. For example, in this research, it was impossible to differentiate between

bedrock ramp, which has a steep slope, and *bedrock cliff* classes due to their similar spectral characteristics and the low DEM resolution.

3. Study Area and Data

3.1 Study Area

The area of interest for this investigation is located in the Avalon Peninsula, Newfoundland and Labrador (NL), covering approximately 1190 linear km of shoreline, as shown in Figure 3.1. The Avalon Peninsula is home to more than 260,000 residents, approximately 51% of the total population of Newfoundland (Government of Canada, 2012).

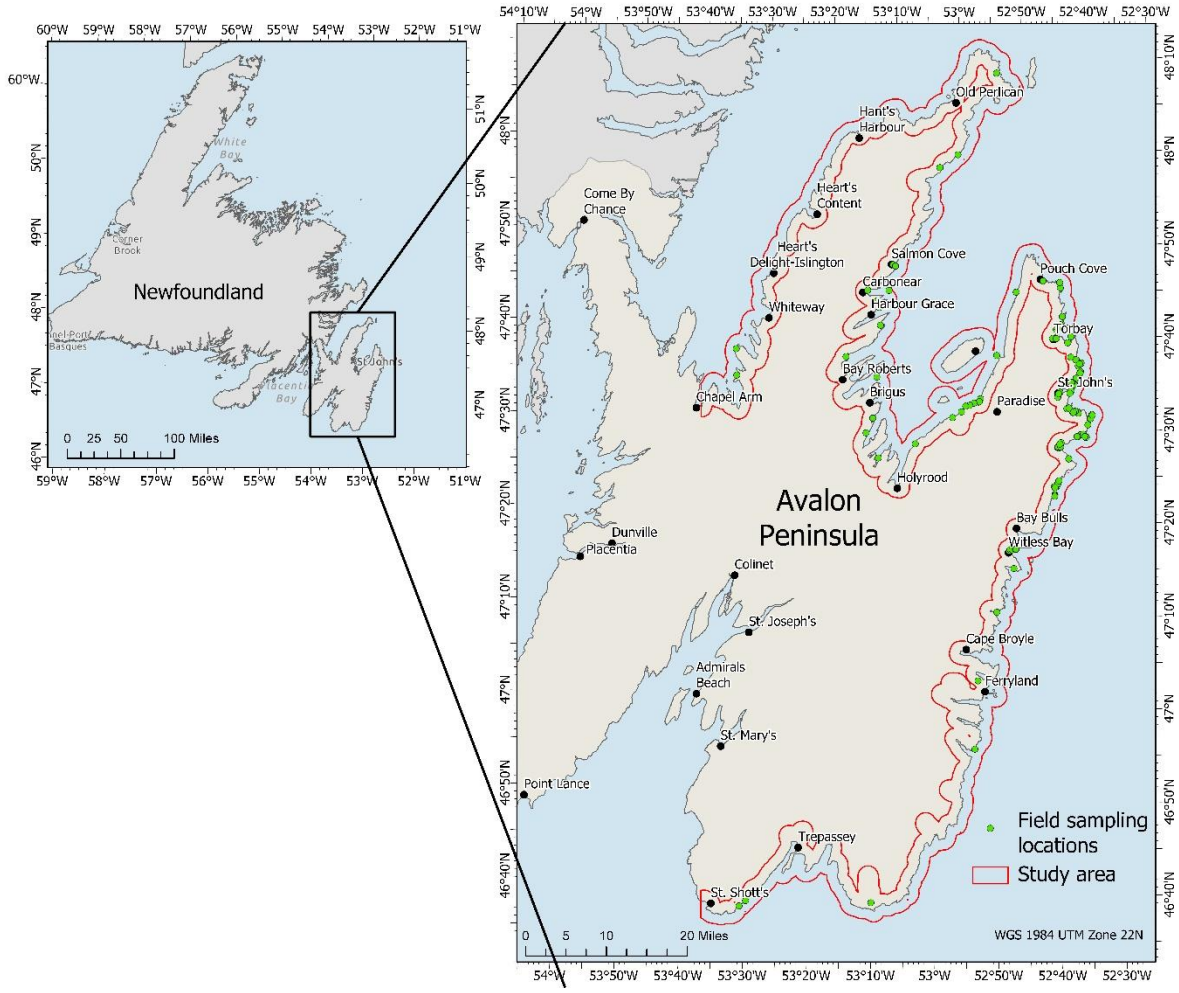

Figure 3.1. Study area.

The Avalon Peninsula is located at the meeting point of warm North Atlantic Current and cold Labrador Current. The mixing of warm and cold waters creates a nearly continual presence of moist air and fog, especially during spring to early summer (Darack, 2006).

Newfoundland's coastal communities have traditionally relied on the harvesting of fish resources as a source of livelihood (Burella et al., 2021). Nowadays, the local fishing industry is represented mostly by small-scale enterprises owned by a single skipper or operating on one vessel (Murray et al., 2007). However, fisheries for cod, flatfish, herring, shellfish, and capelin spawning on gravel beaches of Newfoundland are still of high cultural and economic importance (Byron & Doyle, 2003; Catto & Etheridge, 2006). Also, the coastline of the Avalon Peninsula is recognized as one of the world's most attractive tourism destinations (National Geographic, 2010).

The Avalon Peninsula has one of Canada's most dynamic and physically variable coastlines (Catto, 2011). The dominant shoreline type is the bedrock cliff. The cliffs are habitats for various sessile organisms, such as sponges, corals, and anemones, which attach themselves to the substrate. The study area includes several ecologically valuable areas, provincial parks, and reserves, including Mistaken Point Ecological Reserve (MPER), nominated for the United Nations Educational, Scientific and Cultural Organization (UNESCO) World Heritage Site Status (UNESCO, 2010). MPER, established in 1987, contains some of the oldest and architecturally complex Ediacaran fossils (Narbonne & Gehling, 2003).

The area includes islands that provide essential habitats for seabirds, such as gulls, puffins, and northern gannets, etc. These islands are often characterized by distinct plant and animal communities (NCC, 2020). A potential oil spill occurring near sensitive cliff and island habitats poses a significant risk to sea birds leading to their mortality.

The Avalon Peninsula is located adjacent to the major trans-Atlantic shipping lanes, which connect eastern North America and northwestern Europe. International vessel traffic and local fishery ship traffic result in the potential for oil spill accidents and deliberate discharge of oiled bilge water (Catto & Etheridge, 2006).

Another potential source of an oil spill is the development of offshore oil platforms. The provincial capital, the city of St. John's, is the center of the oil and gas industry in Eastern Canada and is one of 19 World Energy Cities (WECP, n.d.). Four offshore oil-producing projects, including Hibernia, Terra Nova, White Rose, and Hebron, Newfoundland and Labrador produce 25 percent of Canada’s conventional light crude. Oil production operations and the necessary vessel traffic are potential sources of an oil spill. The risk of accidental oil discharges during refinery and tanker operations is also of a big concern.

3.2 Data

3.2.1 Satellite Data

The primary sources of satellite data for this research include imagery from the Sentinel-2 and Sentinel-1 missions operated by the European Space Agency.

Sentinel-2 provides multispectral imagery with a spatial resolution ranging from 10 to 60 m. The imagery was acquired in 13 spectral bands with a swath width of 290 km. The visible and near-infrared (NIR) bands are collected with a spatial resolution of 10 m. The short-wave infrared (SWIR) bands are provided at 20 m, while the coastal aerosol, water vapor, and SWIR-cirrus bands have a spatial resolution of 60 m. Sentinel-2 comprises a constellation of two identical satellites (Sentinel-2A and 2B) flying on the same orbit with a phase difference of 180 degrees and collecting imagery with a nominal revisit schedule of five days. The spectral and spatial characteristics of Sentinel-2 are shown in Table 3.1. Since bands 1, 9, and 10 are primarily designed to support atmospheric correction, they were not used in any subsequent analysis of shoreline types.

Table 3.1. Sentinel-2 sensor characteristics (ESA, n.d.)

Description		Sentinel-2 sensors				Spatial Resolution (m)
		S2A		S2B		
		Central wavelength (nm)	Bandwidth (nm)	Central wavelength (nm)	Bandwidth (nm)	
Band 1	Coastal aerosol	442.7	21	442.3	21	60
Band 2	Blue	492	66	492.1	66	10
Band 3	Green	559.8	36	559.0	36	
Band 4	Red	664.6	31	665.0	31	
Band 5	Vegetation red edge	704.1	15	703.8	16	20
Band 6	Vegetation red edge	740.5	15	739.1	15	
Band 7	Vegetation red edge	782.8	20	779.7	20	
Band 8	NIR	832.8	106	833.0	106	10
Band 8a	Narrow NIR	864.7	21	864.0	22	20
Band 9	Water vapor	945.1	20	943.2	21	60
Band 10	SWIR – Cirrus	1373.5	31	1376.9	30	
Band 11	SWIR	1613.7	91	1610.4	94	20
Band 12	SWIR	2202.4	175	2185.7	185	

Sentinel-2 images are available in two processing levels: Level-1C and Level-2A, corresponding to the top-of-atmosphere and bottom-of-atmosphere (or surface) reflectance in cartographic geometry. For this study, the Level-2A products were used, which was the mission Analysis Ready Data (ARD), i.e., radiometrically, geometrically, and atmospherically corrected, and can be used directly for the analysis.

Three Sentinel-2A scenes (Figure 3.2) were acquired on June 5, 2020. They cover an area of 33,750 square km that includes a shoreline of 1150 km in length. The satellite images were selected based on several criteria, including image acquisition during the vegetation period, low cloud coverage, and low tides at the time of image acquisition. The satellite data were captured in clear weather conditions with minimal cloud coverage (0.06, 0.28, and 0.02 %).

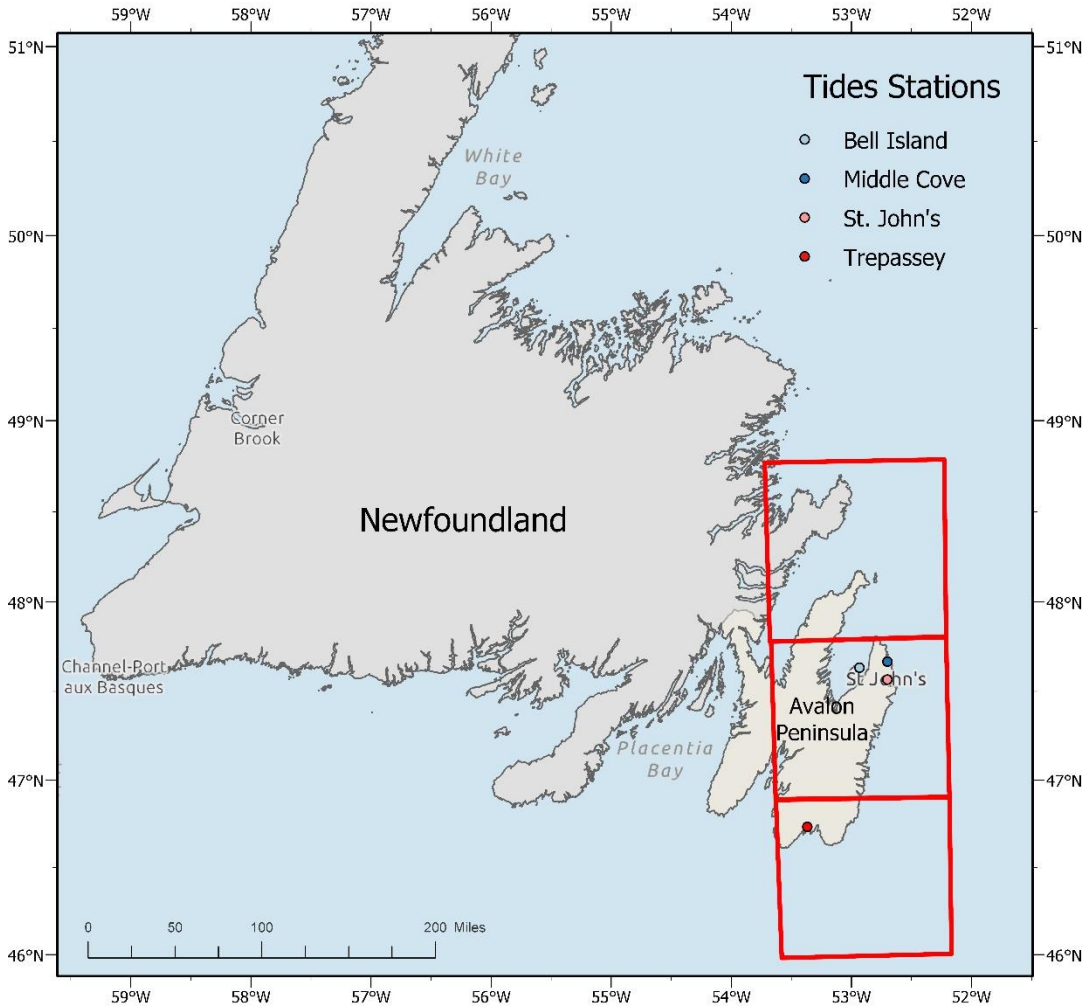

Figure 3.2. Sentinel-2 image coverage.

The Sentinel- 2 data was acquired at 12:08 pm Newfoundland Standard Time (NST), just around an hour before low tide, determined by Fisheries and Oceans Canada (2021) (Table 3.2). That was beneficial for the research as it allows the classification of the intertidal zone, which was considered the most vulnerable to oil spills (ECCC, 2018). At the time of image acquisition, the average water level was approximately 0.3-0.4 m, while the lowest and the highest water levels varied from 0.1 m to 1.5 m during the day. Table 3.2 demonstrates the low water levels closest to the image acquisition time.

Table 3.2. Low water level around the time of Sentinel-2 image acquisition.

	Low water level (m)	Low tide time (NST)
Bell Island	0.1	12:58
St. John's	0.3	13.04
Middle Cove	0.2	12:55
St. Anthony	0.3	12:17
Trepassey	0.2	13:15
Data source: (Fisheries and Oceans Canada, 2021)		

The Sentinel-1 mission comprises two satellites, Sentinel-1A and Sentinel-1B, which carry a C-band SAR able to collect data regardless of weather conditions. The Sentinel-1 SAR instrument, operating at 5.405 GHz, supports four imaging modes (Yagüe-Martínez et al., 2016). In this research, the Level-1 Ground Range Detected (GRD) Interferometric Wide (IW) swath mode products were used. The imagery have a medium resolution of 20 m, and the two-satellite constellation offers a repeat cycle of 6 days on average.

Two dual-polarized (HH+HV) scenes were acquired on June 6, 2020, at around 9:40 am NST (Figure 3.3). At the time of acquisition of Sentinel-1 imagery, the water level was relatively high, which was disadvantageous for the classification results and was taken into consideration (Table 3.3). It was suggested that HH and HV are the best polarizations for differentiating substrates based on surface roughness (Holah et al., 2005). Therefore, the images with both HH and HV polarizations were used in this project.

Table 3.3. Water level around the time of Sentinel-1 image acquisition

	Low water level (m)	Time (NST)
Bell Island	0.8	08:28
St. John's	1.2	07:58
Middle Cove	1.0	07:48
St. Anthony	1.2	07:16
Trepassey	1.4	08:17
Data source: (Fisheries and Oceans Canada, 2021)		

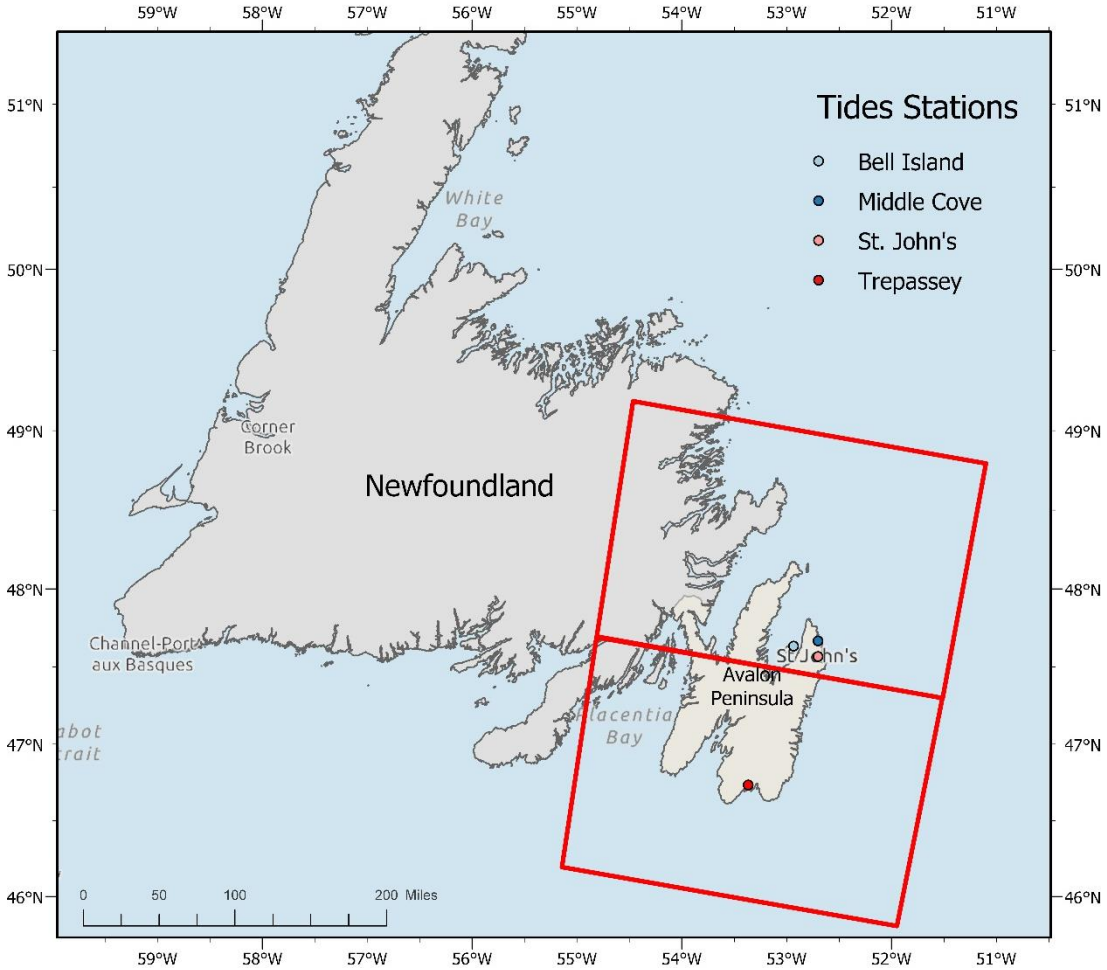

Figure 3.3. Sentinel-1 image coverage.

3.2.2 Auxiliary Data

Auxiliary data used in this investigation included Canadian Digital Elevation Models (CDEMs) datasets as well as aerial photography. CDEM dataset was downloaded from the Government of Canada website (Government of Canada., n.d.). CDEM forms part of the elevation system designed by Natural Resources Canada (NRCan, 2016). The CDEM with the highest available resolution (20 m) was used for this research as the elevation data was considered critical for identifying shoreline types (Demers et al., 2015).

Aerial photography collected in red, green, and blue bands and having the spatial resolution of 0.5 m were also used as reference data to aid in interpreting satellite imagery. This dataset was acquired by the Government of Newfoundland and Labrador Surveys and Mapping Services Division during the summer of 2008 (Government of Newfoundland and Labrador, n.d.). In addition to aerial photography, Google Earth imagery was used for visual analysis of suitable training sample sites.

3.2.3 Field Data

A field survey to collect training and validation data was carried out in August 2020. Prior to any fieldwork, the study area was visually analyzed using high-resolution aerial photography and Google Earth imagery. The potential training sites were selected based on their representativeness of different shoreline types, as well as their accessibility.

The SCAT classification scheme described in Chapter 2.1 was adapted in this research to reflect the scheme currently used by ECCC for shoreline classification (ECCC, 2018; Wynja et al., 2014). This classification has been the common standard for the physical description of shoreline types, backshore types, coastal character, and substrate types for national oil spill response in Canada. Additional classes, which were not used in SCAT methodology, were added

to the classification scheme in this research. These classes include water, forest, and grass. Due to the narrow character of the intertidal zone for *bedrock cliffs*, the *forest* and the *grass* classes are vegetation layers located over the cliffs. Thus, technically the intertidal zones of these classes are represented by cliffs, not vegetation. However, the decision to keep these classes separate and not merge them with the *bedrock cliff* class was made because the difference between these land cover types affects the choice of an appropriate oil spill response technique and provides valuable information about accessibility to the areas.

The field observations were collected in areas of homogeneous land cover. At each site, detailed information, including geographic coordinates, description of dominant land cover(s), and surrounding landscape, was collected, and on-site photographs were taken.

The reference data polygons were defined in a geographic information system (GIS) based on the data collected in-situ as well as satellite, aerial, and Google Earth imagery. The locations of the samples are shown in Figure 3.1. The reference data were split into two datasets. Half of the polygons were used to train the classifiers, and the other half remained for the accuracy assessment of the classified coastal land maps.

Two factors were considered in terms of the selection of sampling location areas. On the one hand, the site should be large enough to capture the characteristics of each class and avoid spectral mixing. On the other hand, the area had to be small enough to prevent high variations between pixel values and to increase class separability. The main concern was that the polygons had to be drawn in such a way that their boundaries did not include transition areas between different land cover types. However, the shorelines in the study area are often very narrow, especially in the case of *bedrock cliffs*. Therefore, in some cases, it was not possible to find a training site with an area wider than four pixels.

Figure 3.4 shows all categories identified during the fieldwork. Some of them were later merged to avoid interclass confusion. For example, the samples of man-made buildings and roads were used as separate subclasses for building learning databases, as they have different spectral characteristics. However, they were combined for the final classification due to the similarity of oil spill response techniques (ECCC, 2018). Similarly, *bedrock high* and *low cliffs* were merged into one category. Also, bedrock platforms having flat and rough surfaces forming the *bedrock platform* class. Table 3.4 summarizes the shoreline classes initially identified during the fieldwork, the generalized categories used for the final classification, and the corresponding pre-spill SCAT shoreline types as described in Chapter 2.1.

Class		Area (m^2)
Bedrock Low Cliff		11945
Bedrock High Cliff		17472
Bedrock Ramp		1669
Bedrock Platform		9152
Platform & Boulders		9303

Class		Area (m^2)
Forest		30090
Grass		15037
Man-Made		26507
Road		10549
Pebble/ Cobble		27772
Sand		13467

Figure 3.4. Initial shoreline types identified during fieldwork.

Table 3.4. Shoreline types used in this study and corresponding SCAT classes

Shoreline classes identified during the fieldwork	Generalized Shoreline Classes used for final classification in this study	Corresponding SCAT Classes
Man-Made structures/ buildings	Man-Made	Man-Made Solid; Man-Made Permeable
Roads		
Bedrock flat platforms	Bedrock Platform	Bedrock
Bedrock platform with rough bouldery surface		
Bedrock high cliffs	Bedrock Cliff	
Bedrock low cliffs		
Pebble/Cobble Beach or Bank	Pebble/Cobble Beach or Bank	Pebble/Cobble Beach or Bank
Sand beach or bank	Sand beach or bank	Sand beach or bank
Forest	Forest	-
Grass	Grass	-
Water	Water	-

4. Methodology

This chapter describes the methodology implemented in this study. The methodological workflow is provided in Figure 4.1.

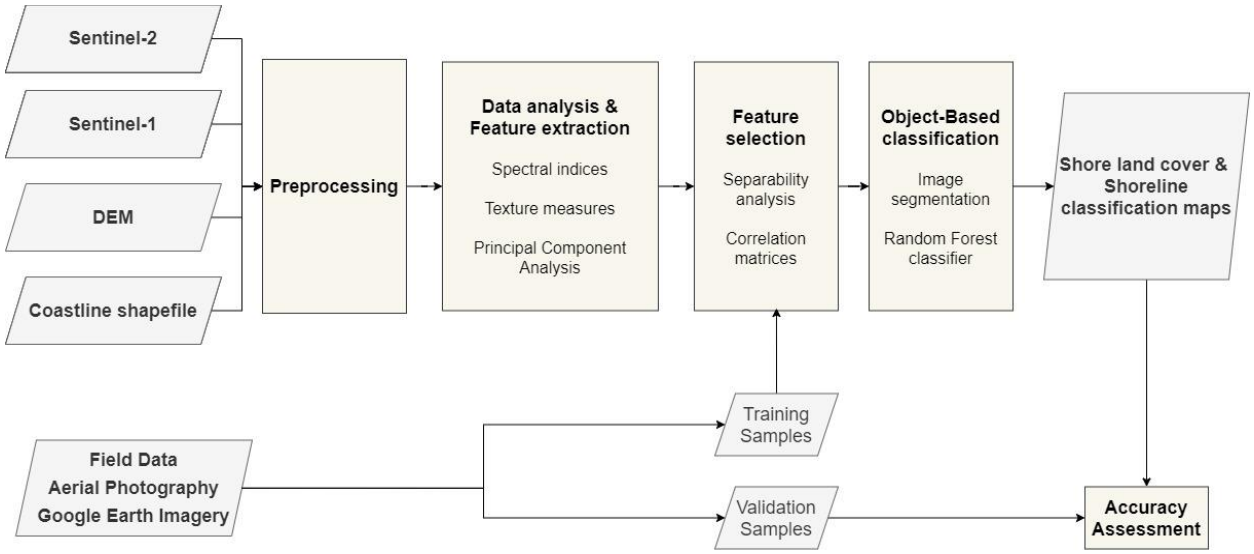

Figure 4.1. Methodology.

First, preprocessing was implemented to ensure that all datasets have the same projection and cover the same area. This was achieved by applying the following steps: reprojection, mosaicking, and clipping. The following additional operations had to be performed with satellite data: calibration, orthorectification, speckle reduction for Sentinel-1 images, and spatial resolution enhancement for Sentinel-2 data. Next, several features, including spectral indices, band ratios, texture measures, and PCs, were generated. This was followed by an additional processing step, namely correlation matrices and box-and-whiskers plots, to identify the most useful features for classification. Finally, an object-based classification, which included image segmentation and applying RF classifier, was implemented. This was followed by the final accuracy assessment analysis. These major steps are discussed in more detail in the following subsections.

4.1 Image Preprocessing

Sentinel-2 products in Level-2A were used in this study. Level-2A images correspond to the bottom-of-atmosphere reflectance in cartographic geometry and are utilized as the Analysis Ready Data mission, i.e., radiometrically, geometrically, and atmospherically corrected, meaning that they can be directly used for the analysis. However, some additional preprocessing steps were still required for this study. They included mosaicking and spatial resolution enhancement.

Sentinel-2 imagery collected in visible and NIR bands had 10 m spatial resolution, while red-edge and SWIR bands data had the resolution of 20 m. The spectral bands with a 20 m spatial resolution were resampled to a pixel size of 10 m to maintain the spatial resolution integrity. For this purpose, a super-resolution (SuperRes) method introduced by Brodu (2017) was applied. This technique relies on the assumption that the proportion of objects within a pixel area is the same across the bands. However, the reflectance of each element depends on the spectral band at which it is observed, and thus, varies from band to band. Starting from the highest resolution bands, this technique separates band-dependent spectral information, i.e., reflectance, from information that is common across all bands. i.e., the geometry of scene elements. Then, the model unmixes the low-resolution bands such that they are consistent with those band-independent scene elements while preserving their overall reflectance. The subsets of resulting products obtained by the super-resolution algorithm implementation compared with original Sentinel-2 and resampled images are demonstrated in Appendix A.

The preprocessing steps for Sentinel-1 data included calibration, orthorectification, speckle reduction, and image mosaicking. First, digital pixel values were converted to radiometrically calibrated SAR backscatter coefficient, which provides a backscatter ratio estimate per given reference area. The reference area can be defined to be in the slant range plane (Beta Naught

backscatter), locally tangent to an ellipsoidal model of the ground surface (Sigma Naught), or in the plane perpendicular to the line of sight from the sensor to an ellipsoidal model of the ground surface (Gamma Naught) (Small, 2011). In this research, the Sentinel-1 imagery was calibrated to the Sigma Naught σ° using the procedure introduced by Filipponi (2019) implemented in the PCI Geomatica 2018 software.

Speckle is one of the main SAR data drawbacks, which negatively affects the visual appearance of images and the accuracy of further image analysis (Lee, 1981). In this study, the enhanced Lee adaptive filter was selected to suppress the effect of speckle noise because of its ability to preserve edges, linear features, and texture information (Lee et al., 1994). A 5 x 5 window was selected due to the small size of shoreline features to be classified in this study. This allowed maintaining the boundaries between natural objects.

Orthorectification of de-speckled Sentinel-1 data was performed using the rational function model (Zhang et al., 2011; Habib et al., 2007) based on the external DEM previously obtained from the Government of Canada website (Government of Canada., n.d.).

A two-km buffer was created along the eastern part of the Avalon Peninsula coastline to define the boundaries of the study area. All datasets were projected to the Universal Transverse Mercator (UTM) Zone 22 N coordinate system using the WGS84 reference ellipsoid, mosaicked and clipped by the previously obtained study area polygon. The classification was applied only to the area inside this polygon to reduce computational expenses.

4.2 Feature Extraction & Selection

First, original spectral bands were extracted and used to inspect the spectral characteristics of shoreline features by constructing spectral profiles and box-and-whisker plots of pixel

distributions of classes in each band. During the exploratory analysis, spectral evaluation for the unique characteristics of some features has been performed.

Spectral profiles were produced for the shoreline classes using the training sample polygons. Means of pixels for each class were derived after applying the SuperRes algorithm. The spectral response exploratory analysis allowed examining the separation capacity of the Sentinel-2 data and generated additional predictable variables, such as band ratios and spectral indices. Next, 39 spectral features were extracted to assess their influence on classification performance. These spectral indices included soil (brightness-related), water, and vegetation indices which were sensitive to soil texture, moisture, and changes in organic matter content (Gholizadeh et al., 2018). A summary of the derived indices is presented in Table 4.1.

Table 4.1. Derived indices and band ratios details

Index	Definition	Reference
Normalized Difference Built-up Index	$NDBI = \frac{SWIR1 - NIR}{SWIR1 + NIR}$	(Zha et al., 2003)
Second Brightness Index	$BI2 = \frac{\sqrt{Red^2 + Green^2 + NIR^2}}{3}$	(Escadafal, 1989)
Redness Index	$RI = \frac{Red^2}{Green^3}$	(Pouget et al., 1991)
Brightness Index	$BI = \frac{\sqrt{Red^2 + Green^2}}{2}$	(Escadafal, 1989)
Color Index	$CI = \frac{Red - Green}{Red + Green}$	(Pouget et al., 1991)
Difference Vegetation Index	$DVI = NIR - Red$	(Tucker, 1979)
Green Normalized Difference Vegetation Index	$GNDVI = \frac{NIR - Green}{NIR + Green}$	(Gitelson et al., 1996)
Infrared Percentage Vegetation Index	$IPVI = \frac{NIR}{NIR + RED}$	(Crippen, 1990)
Inverted Red-Edge Chlorophyll Index	$IRECI = \frac{NIR - Red}{RE1/RE2}$	(Frampton et al., 2013)
Modified Soil Adjusted Vegetation Index	$MSAVI = \frac{(NIR - Red) * (1 + L)}{NIR + Red + L}$, $where\ L = 1 - 2\mathrm{a} * \mathrm{NDVI} * \mathrm{WDVI}$, a is the slope of the soil line	(Qi et al., 1994)
Normalized Difference Pigment Index	$NDPI = \frac{SWIR - Green}{SWIR + Green}$	(Lacaux et al., 2007)
Normalized Differential Turbidity Index	$NDTI = \frac{Red - Green}{Red + Green}$	(Lacaux et al., 2007)
Modified Normalized Difference Water Index	$MNDWI = \frac{Green - SWIR}{Green + SWIR}$	(Xu, 2006)
Normalized Difference Water Index	$NDWI = \frac{Green - NIR}{Green + NIR}$	(McFeeters, 1996)
Pigment Specific Simple Ratio (Cholophyll a)	$PSSRA = \frac{NIR}{Red}$	(Blackburn, 1998)
Perpendicular Vegetation Index	$PVI = NIR - Red$	(Major et al., 1990)
Transformed NDVI	$TNDVI = \sqrt{\frac{NIR - Red}{NIR + Red} + 0.5}$	(Tucker, 1979)
Weighted Difference Vegetation Index	$WDVI = NIR - \alpha Red$, where α is the slope of the soil line	(Clevers & Verhoef, 1993)
Aerosol-free Vegetation Index	$AFRI = \frac{NIR - 0.66SWIR1}{NIR + 0.66SWIR1}$	(Karnieli et al., 2001)

[Continued on the next page]

Table 4.1. Derived indices and band ratios details [continue]

Index	Definition	Reference
Aerosol-free Vegetation Index 21	$AFRI21 = \frac{NIR - 0.5SWIR2}{NIR + 0.5SWIR2}$	(Karnieli et al., 2001)
Red Edge Chlorophyll Index	$CIRedEdge = \frac{RE1}{RE2} - 1$	(Clevers & Gitelson, 2012)
Two-band Enhanced Vegetation Index	$EVI2 = \frac{2.5(NIR - Red)}{NIR + 2.4Red + 1}$	(Jiang et al., 2008)
Enhanced Vegetation Index	$EVI = \frac{2.5(NIR - Red)}{1 + NIR + 6Red - 7.5Blue}$	(A. Huete et al., 2002)
Global Environment Monitoring Index	$GEMI = \frac{\eta(1 - 0.25\eta) - (Red + 0.125)}{1 - Red}$, $where\ \eta = \frac{2(NIR^2 - Red^2) + 1.5NIR + 0.5Red}{NIR + Red + 0.5}$	(Pinty & Verstraete, 1992)
Greenness Index	$GI = \frac{Green}{Red}$	(Main et al., 2011)
Green-Red Vegetation Index	$\mathrm{GRVI} = \frac{Green - Red}{Green + Red}$	(Motohka et al., 2010)
Leaf Area Index	$LAI = (3.618 \times EVI) - 0.118$	(Boegh et al., 2002)
Modified Chlorophyll Absorption Ratio Index Improved	$MCARI2 = \frac{1.5\big(2.5(NIR - Red)\big) - (1.3(NIR - Green))}{\sqrt{(2NIR + 1)^2 - (6NIR - 5\sqrt{Red} - 0.5}}$	(Haboudane et al., 2004)
Modified Chlorophyll Absorption in Reflectance Index	$MCARI = \big((RE - Red) - 0.2(RE - Green)\big) * \frac{RE}{Red}$	(Daughtry et al., 2000)
Modified Soil Adjusted Vegetation Index	$MSAVI2 = 0.5(2(NIR + 1) - \sqrt{2NIR + 1^2 - 8(NIR - Red)}$	(Qi et al., 1994)
Modified Triangular Vegetation Index	$MTVI = 1.2(1.2(NIR - Green) - 2.5(Red - Green))$	(Haboudane et al., 2004)
Normalized Differences Vegetation Index	$NDVI = \frac{NIR - Red}{NIR + Red}$	(Tucker, 1979)
Normalized Multi-band Drought Index	$NMDI = \frac{NIR - (SWIR1 - SWIR2)}{NIR + (SWIR1 - SWIR2)}$	(L. Wang & Qu, 2007)
Optimized soil-adjusted vegetation index	$OSAVI = \frac{(NIR - Red)}{NIR + Red + 0.16}$	(Rondeaux et al., 1996)
Red Edge Normalized Difference Vegetation Index	$RENDVI = \frac{RE - NIR}{RE + NIR}$	(Gitelson et al., 1996)
Ratio Vegetation-Index	$RVI = \frac{Red}{NIR}$	(Pearson & Miller, 1972)
Soil Adjusted Vegetation Index	$SAVI = \frac{(NIR - Red) * (1 + L)}{NIR - Red + L}$, $where\ L = 0{,}5$	(A. R. Huete, 1988)

Principal component analysis was applied to Sentinel-2 data to create and explore the predictable variables for classification. Ten Sentinel-2 bands (i.e., B2 to B8a, B11, and B12) were used as an input for PCA analysis, creating ten principal components.

Several textural features were calculated based on the GLCM (Haralick et al., 1973) for visible and NIR bands of the satellite image, including contrast, dissimilarity, and homogeneity, ASM, energy, entropy, mean, variance, and GLCM correlation were also extracted (Table 4.2). Image texture was analyzed using a window size of 5 x 5, which correspond to the area of 2500 m² on the ground. This window size was the smallest window size available in ESA Sentinel Application Platform v8.0.0. It was chosen due to the nature of shorelines, which are generally narrow along the coastline in the study area. Therefore, having a smaller window size allowed maintaining the boundaries between various land cover types.

Table 4.2. GLCM texture measures and their equations.

GLCM Texture Variable		Equation	
Contrast	Contrast	$CON = \sum_{i,j=0}^{N-1} P_{i,j}(i-j)^2$	(4-1)
	Dissimilarity	$DISS = \sum_{i,j=0}^{N-1} P_{i,j} \left\lvert i-j \right\rvert$	(4-2)
	Homogeneity	$HOM = \sum_{i,j=0}^{N-1} \frac{P_{i,j}}{1+(i-j)^2}$	(4-3)
Orderliness	Angular Second Moment	$ASM = \sum_{i,j=0}^{N-1} {P_{i,j}}^2$	(4-4)
	Energy	$E = \sqrt{ASM}$	(4-5)
	Entropy	$ENT = \sum_{i,j=0}^{N-1} P_{i,j}(-\ln P_{i,j})$	(4-6)
	Maximum Probability	$MAX = max_{ij}\, P_{i,j}$	(4-7)
Statistics	Mean	$\mu_i = \sum_{i,j=0}^{N-1} i(P_{i,j})$ $\mu_j = \sum_{i,j=0}^{N-1} j(P_{i,j})$	(4-8)
	Variance	$\sigma_i^2 = \sum_{i,j=0}^{N-1} P_{i,j}(i-\mu_i)^2$ $\sigma_j^2 = \sum_{i,j=0}^{N-1} P_{i,j}(j-\mu_j)^2$	(4-9)
	Correlation	$COR = \sum_{i,j=0}^{N-1} P_{i,j}[\frac{(i-\mu_i)(j-\mu_j)}{\sqrt{(\sigma_i^2)(j)}}]$	(4-10)

i and ***j*** are the labels of the GLCM columns and rows, respectively.
$\boldsymbol{P_{i,j}}$ is the probability of values ***i*** and ***j*** occurring in neighboring pixels in the original image within the user-defined window.

In total, 76 potential predictor variables were generated, including 10 spectral, 44 spectral indices, ten principal components, 40 texture measures, and two radar backscattering features. Training sample statistics were collected from each imagery for feature selection to identify the most useful features for classification.

Feature selection was conducted based on the visual analysis of box-and-whisker plots, as this type of analysis provides a better understanding compared to the statistical analysis (Jensen, 2016).

To exclude the bands with redundant spectral information, correlation matrices were produced. In particular, a feature from a pair of features with an absolute correlation value higher than 0.9 was excluded from further analysis. This reduced the data dimensionality and, thus, minimized the image classification processing time without affecting the accuracy.

4.3 Segmentation

Following preprocessing, the satellite image was partitioned into non-overlapping homogeneous regions using the MRS algorithm. Image segmentation was performed in the Trimble eCognition Developer 9.5.0. In particular, the MRS approach creates a hierarchical network of image objects by implementing the segmentation at different levels with various parameters. Each object is encoded with its neighbors, super-object, and sub-objects (Göttsche & Olesen, 2002). In this study, a two-level hierarchical network of objects was created. Since a DEM and slope parameters play a key role in defining shoreline classes, these variables were used to create the first segmentation level. The second level was generated based on the VNIR bands, as they have the highest spatial resolution among Sentinel-2 images. Notably, using a DEM and slope parameters is not very common in remote sensing for the image segmentation process. However, several studies proved the efficiency of segmentation using different terrain attributes for various purposes, such as identification of different landscape types (Eisak et al., 2014; Iwahashi et al., 2018; Iwahashi & Pike, 2007; Stepinski & Bagaria, 2009) or building localization and classification (Miliaresis & Kokkas, 2007; Woestyne et al., 2004).

Three parameters of scale, shape, and compactness must be determined for using MRS. Since there are no generally accepted segmentation criteria for shoreline classification, several combinations of parameters were examined. For shape and compactness parameters, the lowest values were chosen due to the nature of Newfoundland's coastal zone, which is generally narrow. The optimal segmentation parameters were assessed visually through an iterative process. Various scale parameters from 10 to 50 were tested. The scale parameter determines the maximum standard deviation of the homogeneity with regard to the image layers' weights. In general, smaller values of the scale parameter produce smaller image objects. The scale parameters from 30 to 40 demonstrated the most acceptable results during visual analysis. Then, several classifications were implemented using the scales of 30 to 40, and the segmentation model that produced the best classification results was selected for further analysis. As a result, the values of 35, 0.1, and 0.1 were chosen for scale, shape, and compactness, respectively.

4.4 Random Forest Classification

The Random Forest (RF) classifier described by Breiman (2001a) was used in this research as it demonstrated advantages (such as robustness to outliers and noise, high processing speed, and the ability to generate useful estimates of error) over other algorithms in many satellite-based land cover classification studies, including robustness to outliers and noise, high processing speed, the ability to generate useful estimates of error, strength, and correlation (Belgiu & Drăguţ, 2016; Pelletier et al., 2016; Pal, 2005; Breiman, 2001b; Breiman et al., 1984). Some studies suggested that RF was less affected by redundant data compared to the other algorithms, such as K-nearest neighbor (KNN) and support vector machine (SVM) (Li et al., 2016).

In general, the RF classifier is an ensemble learning method that generates a number of trees from training samples and their subsets (Breiman, 2001b). The dataset is classified several

times using a random subselection of training pixels. This results in creating multiple decision trees. The final decision is made based on a vote of each tree, i.e., the most frequent tree output is used as the final one (Gislason et al., 2006).

Considering all these advantages, RF was chosen to classify shoreline types in this study. Also, the implementation of RF allowed using high dimensional data from a variety of sources, including satellite data obtained from Sentinel-1 and -2, as well as topographical features.

RF classifiers require several parameters that should be determined by a user, including the number of trees (N) and the number of variables for splitting at each tree node (M). The M parameter was set as the square root of the number of the available layers, as suggested by previous related research (Belgiu & Drăguţ, 2016; Gislason et al., 2006). Increasing the N parameter leads to higher accuracy rates, although this improvement levels off eventually. In this study, 1000 trees have been generated in the forest. The decision about the number of trees was based on previous studies where fewer than 1000 trees reduced the classification accuracy, while more trees did not improve results (Reese et al., 2014; Guan et al., 2013; Millard & Richardson, 2013).

Ten classification scenarios were tested to find the best combination of input variables producing the highest classification results. The tested scenarios contained various combinations of input variables including original Sentinel-2 bands, principal components, textural measures, spectral indices, SAR backscatter data, and terrain parameters. The results obtained from the best coastal land classification model were used to create the shoreline classification map. The polyline shapefile representing the shoreline was divided into 0.5 km long segments. Then, each segment was assigned to a class based on the information of the closest polygon of the coastal land classification map.

As a result, the two classification maps are created: shoreline and coastal land cover maps. The coastal land cover map shows the polygons representing different types of surfaces within a two km buffer from the shoreline. This area covers both foreshore and backshore zones. The shoreline classification map depicts the line representing various sediment types of a coastline, i.e., a line that forms the boundary between the land and the ocean.

4.5 Accuracy Assessment

The classification accuracies were assessed for each scenario to investigate the degree of 'correctness' of the resulting maps (Campbell & Wynne, 2011). An accuracy assessment was performed using a confusion (error) matrix, a cross-tabulation of the assigned class against the corresponding class observed in the field (Canters, 1997).

Global and class-dependent measures of accuracy, including overall accuracy (OA), producer's accuracy (PA), user's accuracy (UA), and Cohen's Kappa statistic, were derived from an error matrix. The model with the highest OA was considered the one that produced the best classification results.

The description of these measures is presented in Table 4.3. To obtain OA, the number of correctly classified pixels was divided by the total number of test pixels. The total number of correct pixels in a class was divided by the total number of pixels of the corresponding class identified during the fieldwork to calculate PA. UA was obtained by dividing the total number of correct pixels in a class by the total number of pixels classified in that class. The Kappa index was calculated as the number of correctly classified pixels by the model divided by the number of correctly classified pixels by random chance (Camps-Valls et al., 2011; Zhenku & Redmond, 1995).

Table 4.3. The accuracy measures calculated in this research

Description	Equation	
Overall accuracy (OA) is obtained from the matrix by dividing the number of pixels correctly classified by the total number of test pixels.	$OA = \frac{\sum_{j=1}^{q} n_{jj}}{N}$	(4-11)
User's accuracy (UA) of a class is the proportion of the pixels classified as a class i that has reference class i. UA is a measure of commission error (errors of inclusion) and indicates the probability of a classified pixel on the map to represent that category on the ground	$U_i = \frac{n_{ii}}{\sum_{j=1}^{q} n_{ij}}$	(4-12)
Producer's accuracy (PA) of a class represents the probability that a pixel belonging to class j in the reference dataset is correctly classified. PA is the total number of correct pixels in a class divided by the total number of pixels of the corresponding class identified from the ground-truth data (i.e., the column total). PA is a measure of omission error (errors of exclusion) and shows the probability of reference pixels correctly classified.	$P_j = \frac{n_{jj}}{\sum_{i=1}^{q} n_{ij}}$	(4-13)
Kappa coefficient, or the Kappa index of agreement (KIA), reflects the difference between actual agreement and the agreement expected by chance.	$KIA = \frac{\frac{\sum_{j=1}^{q} n_{jj}}{N} - \sum_{i=1}^{q} P_{i+}P_{+j}}{1 - \sum_{i=1}^{q} P_{i+}P_{+j}}$	(4-14)
n is the number of pixels, q is the number of classes, N is the total number of test pixels, i and j are $\{1,2, \dots q\}$ and represent the classified on the map and the reference (ground truth) classes represented by rows and columns, respectively, in an error matrix.		

The evaluation of whether the differences between the accuracies obtained from various scenarios are statistically significant was done to ensure that the accuracies are similar in a statistical sense.

The non-parametric McNemar's test was used in this study because it is designed to assess the statistical significance of the difference between two proportions when samples are not independent (McNemar, 1947). First, a 2 × 2 dimension confusion matrix of the number of correctly and wrongly classified pixels for each pair of scenarios was calculated. The following elements were computed from an error classification matrix: f_{12} is the number of samples correctly classified by the first scenario but misclassified by the second one; f_{21} is the number of samples wrongly classified by the first scenario but correctly classified by the second one; f_{11} and f_{22} are the numbers of samples correctly classified and misclassified by both scenarios, respectively.

Table 4.4. The matrix of correctly and incorrectly classified pixels for classifications used for McNemar's test

Allocation		Classification 2		
		Correct	Incorrect	Sum
Classification 1	Correct	f_{11}	f_{12}	
	Incorrect	f_{21}	f_{22}	
	Sum			

Then, z score was also calculated as:

$$z = \frac{f_{12} - f_{21}}{\sqrt{f_{12} + f_{21}}} \tag{4-15}$$

The null hypothesis H_0 of no significant difference was rejected at 5% level if $|z|$ is less than 1.96 (Kumar et al., 2017). Also, the chi-square (X^2)-test was calculated to assess whether the difference between classifications is significant using the following equation:

$$X^2 = \frac{(f_{12} - f_{21})^2}{f_{12} + f_{21}} \tag{4-16}$$

The obtained X^2 value was compared against the tabulated chi-squared values. The H_0, of no significant difference, was rejected if the obtained X^2 was less the tabulated chi-squared value at a particular level of significance with one degree of freedom (de Leeuw et al., 2006).

Similar to the coastal land classification map, the assessment of the shoreline classification map was performed through the computation of a confusion matrix. The samples for accuracy assessment were generated by the creation of randomly distributed points within the previously collected polygons for validation. The points among each class were allocated proportionally to the total area of polygons of each shoreline type (i.e., the shoreline type having a larger total area of polygons gets more points). The confusion matrix was used to calculate accuracy assessment matrices, including OA, PA, UA, and Kappa statistics.

5. Results

5.1 Selection of Predictor Variables

During the preprocessing and the feature extraction steps, 10 Sentinel-2 bands were enhanced and unified by 10 m resolution by utilizing a SuperRes method (Brodu, 2017). De-speckled Sigma Naught σ° backscatter values were extracted for dual-polarized HH and HV Sentinel-1 bands.

Thirty-nine spectral indices were extracted following the equations in Table 4.1. These spectral indices included soil (brightness-related), water, and vegetation indices, which were sensitive to soil texture, moisture, and changes in organic matter content (Gholizadeh et al., 2018). In addition, 40 textural features were extracted using the equations shown in Table 4.2. The list of all extracted variables is shown in Table 5.1.

The feature selection process involved the exclusion of redundant bands based on the analysis of correlation matrices and box-and-whiskers plots. The detailed description of the results obtained during the feature extraction and selection steps is presented in the following subsections.

Table 5.1. Extracted features from Sentinel-2 and Sentinel-1.

Sentinel-2 bands	
B2 - Blue	B7 - Vegetation red edge-3
B3 - Green	B8-NIR
B4 - Red	B8a-Narrow NIR
B5 - Vegetation red edge-1	B11-SWIR-1
B6 - Vegetation red edge-2	B12-SWIR-2
Sentinel-1 bands	
Sigma Naught σ° backscatter values extracted from HH band	
Sigma Naught σ° backscatter values extracted from HV band	
Spectral Indices	
Normalized Difference Built-up Index (NDBI)	Aerosol-free Vegetation Index 21 (AFRI 21)
Second Brightness Index (BI2)	Red Edge Chlorophyll Index (CIRedEdge)
Redness Index (RI)	Two-band Enhanced Vegetation Index (EVI2)
Brightness Index (BI)	Enhanced Vegetation Index (EVI)
Color Index (CI)	Global Environment Monitoring Index (GEMI)
Difference Vegetation Index (DVI)	Greenness Index (GI)
Green Normalized Difference Vegetation Index (GNDVI)	Green-Red Vegetation Index (GRVI)
Infrared Percentage Vegetation Index (IPVI)	Leaf Area Index (LAI)
Inverted Red-Edge Chlorophyll Index (IRECI)	Modified Chlorophyll Absorption Ratio Index Improved (MCARI2)
Modified Soil Adjusted Vegetation Index (MSAVI)	Modified Chlorophyll Absorption in Reflectance Index (MCARI)
Normalized Difference Pigment Index (NDPI)	Modified Soil Adjusted Vegetation Index (MSAVI2)
Normalized Differential Turbidity Index (NDTI)	Modified Triangular Vegetation Index (MTVI)
Modified Normalized Difference Water Index (MNDVWI)	Normalized Differences Vegetation Index (NDVI)
Normalized Difference Water Index (NDWI)	Normalized Multi-band Drought Index (NMDI)
Pigment Specific Simple Ratio (Cholophyll a) (PSSRA)	Optimized soil-adjusted vegetation index (OSAVI)
Perpendicular Vegetation Index (PVI)	Red Edge Normalized Difference Vegetation Index (RENDVI)
Transformed NDVI (TNDVI)	Ratio Vegetation-Index (RVI)
Weighted Difference Vegetation Index (WDVI)	Soil Adjusted Vegetation Index (SAVI)
Aerosol-free Vegetation Index (AFRI)	
Texture measures - extracted for B2, B3, B4, and B8	
Contrast (CON)	Entropy (ENT)
Dissimilarity (DISS)	Maximum Probability (MAX)
Homogeneity (HOM)	Mean
Angular Second Moment (ASM)	Variance (VAR)
Energy (E)	Correlation (COR)

5.1.1 Spectral Bands and Indices

Spectral profiles (Figure 5.1) were constructed for the eleven shoreline classes defined based on the training sample polygons to examine the separation capacity of the Sentinel-2 data. These classes are *low bedrock cliff, high bedrock cliff, bedrock ramp, bedrock platform/low ramp,*

bedrock boulder platform, *forest*, *grass*, *man-made*, *road*, *pebble/cobble*, and *sand*. The lines in the figure represent the average pixel value for each class.

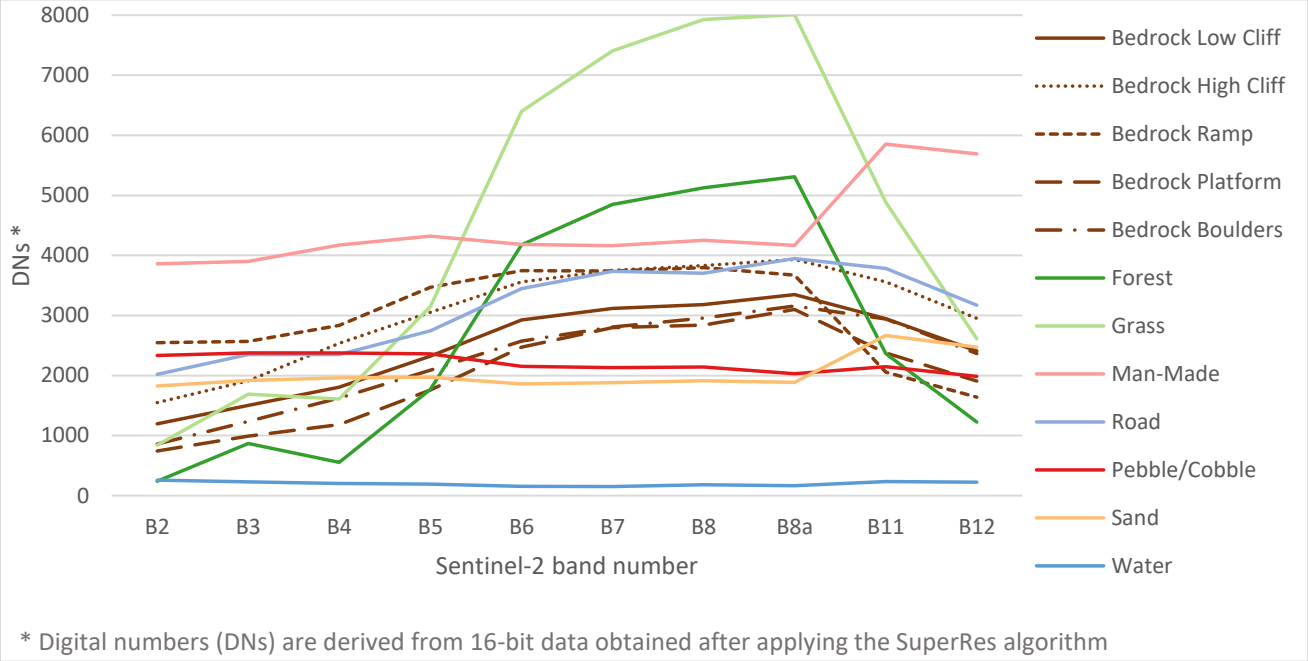

Figure 5.1. Spectral profiles of shoreline types using Sentinel-2A data.

All bedrock classes demonstrated a similar spectral response. They were characterized by a slight increase in spectral responses from visible bands to the narrow NIR, followed by a slight decrease in the SWIR spectrum. *Road* and *pebble/cobble* classes followed similar curves across the bands. This similarity may also be observed in the box-and-whisker plots constructed for all ten Sentinel-2 bands shown in Appendix C (Figure C.1 to Figure C.10). In general, the potential of visible bands to differentiate between non-vegetated classes is low. The largest separability potential among these classes is found between the *high bedrock cliff* and *bedrock platform*.

A noticeable increase of spectral reflectance from red-edge to NIR bands may be easily observed for the vegetation classes, i.e., forest and grass. These characteristics are widely used for the computation of different vegetation indices, which were also calculated in this study.

While the DN of the *man-made* class, which mostly includes buildings and structures, does not dramatically change from visible to NIR bands, the values significantly rise from NIR to SWIR bands. This can be explained by the fact that roofs usually contain a strong iron-oxide component, which is characterized by absorption at visible and NIR (Herold et al., 2004). The reflectance increasing towards longer wavelengths may be also related to the absence of water features in roofs' material (Heiden et al., 2001). This difference between the reflectance values of man-made features in NIR and SWIR is usually used to compute NDBI, which helps to distinguish built-up areas from the other classes. In this study, it was found that the narrow NIR band has lower mean values for the *man-made* class, and computed an index using B8a and SWIR to discriminate *man-made* class from the others. It is worth noting that the *sand* class also rises from B8a to B11. Therefore, confusion between the *man-made* and *sand* classes may occur. *Pebble/cobble* pixel values slightly decreased between visible and NIR bands. This distinctive feature was used to compute another spectral index using B4 and B8a bands.

In addition to these proposed indices, the other 39 existing spectral indices described in Chapter 4.2 were examined. The correlation matrix (Appendix B) was also constructed to find the highly correlated indices. A feature from a pair with an absolute correlation value higher than 0.9 was excluded from further analysis. The remaining indices were further analyzed for the ability to separate different shoreline types using the visual interpretation of box-and-whisker plots. The products, for which the boxes in box-and-whisker plots were overlapping for multiple classes, were considered insignificant and were excluded from further analysis. The indices initially incorporated for classification were NDPI, MNDWI, IRECI, GNDVI, IPVI, NDWI, CI, NDBI, $\frac{(B4-B8a)}{(B4+B8a)}$ (further refer to as Ratio 1), $\frac{(B8a-B2)}{(B8a+B2)}$ (further refer to as Ratio 2), $\frac{(B11-B8a)}{(B11+B8a)}$ (further refer to as Ratio 3). However, only four of them (NDBI, MNDWI, Ratio 1, and Ratio 2) were selected

for the final classification during the next feature selection step, which was implemented using the trial and error method. The box-and-whisker plots of these products are shown in Appendix C (Figure C.11 to Figure C.14).

5.1.2 Principal Component Analysis

Ten principal components were obtained from the PCA. An exploratory analysis was conducted to examine the usefulness of these components for shoreline classification. The first principal component describes 96.05% of the variance in the ten Sentinel-2 bands used for this research. The second principal component accounts for 3.13% of the remaining variance, while the third one explains another 0.65%, bringing the total of the first three components to 99.82% (Table 5.2). This was in agreement with the visual inspection, which found the best image quality of the first principal component that is decreasing sequentially with each subsequent remaining principal component, as it is shown in Appendix D (Figure D.1).

Table 5.2. Percent and Accumulative of Eigenvalues

Principal Component	Variance Explained [%]	Cumulative Variance Explained [%]
PC1	96.7729	96.7729
PC2	2.481	99.254
PC3	0.580	99.834
PC4	0.059	99.893
PC 5	0.041	99.934
PC 6	0.021	99.955
PC 7	0.018	99.973
PC 8	0.012	99.985
PC 9	0.008	99.993
PC 10	0.007	100

The first principal component is highly correlated with the NIR, Red Edge, and SWIR bands, while the second principal component's highest correlation was found with the blue band (Appendix B). Box-and-whisker plots of all principal components are presented in Appendix C

(Figure C.14 to Figure C.24). Like the visible bands, principal components do not provide a strong separability between non-vegetated classes. However, the use of several variables may help in successful discrimination between different shoreline types. For example, while the first principal component shows a similar distribution between *pebble/cobble* and *platform*, these classes were separable using principal components 2, 3, and 7. Likewise, the box-and-whisker plots for both principal components 1, 2, and 6 demonstrate the difference between the distribution of the values of *platform* and *cliff*. At the same time, other principal components have similar values for these classes. The best separability of *water* from other classes was found for the first principal component product.

As shown in Table 5.2, the first three principal components explain a large proportion of the variance, and subsequent principal components explain much less. With the decrease of information contained in each subsequent PC, the interclass separability potential of these components is also declining. Therefore, principal components 8-10 products were removed from the final classification as they did not provide interclass separability.

5.1.3 Texture Features

As a result of texture analysis, 10 GLCM measures were created for each of the blue, red, green, and NIR Sentinel-2 bands (Table 5.3). First, the correlation matrix was computed for all 40 texture features (Figure B.2). Many of these measures were highly correlated because of the calculation method, as it agrees with Hall-Beyer (2016). One of the texture measures within a pair with an absolute correlation value higher than 0.9 was excluded from further analysis. The decision to exclude a feature for a pair was made based on the corresponding box-and-whisker plots. The box-and-whisker plots of the remaining measures are represented in Appendix C (Figure C.25 to Figure C.30). However, not all of them were included in the final classification. RF was

implemented in the Trimble eCognition Developer 9.5.0 software, which also produced variable importance estimations, providing qualitative analysis of the variable contribution. During the trial and error approach, the least important variables were excluded from the classification scenario and the resulted OA was checked. If the resulted OA increased, these features were excluded from further analysis. If the OA did not increase, the features were returned to the classification scenario. The improvement of the OA (from 84.2% in scenario 5 to 85.6% in scenario 8) was observed when B3 CON, B3 DISS, and B4 ASM were not used. As a result, only six texture features, including B2 CON, B2 E, B2 VAR, B2 ENT, B4 COR, and B3 contrast (Figure 5.2), were employed in the final classification. Table 5.3 summarizes a list of textural features extracted and employed for shoreline classification in this study.

To conclude, only 18 features remained during the feature selection process, which was performed through box-and-whisker plots, correlation matrices, and classification accuracy assessment. The correlation matrix of these features is shown in Figure 5.3.

Table 5.3. Texture measures extracted in the study

Texture measures	Sentinel-2 bands			
	B2	B3	B4	B8
Contrast (CON)	✓	o	×	×
Dissimilarity (DISS)	×	o	×	×
Homogeneity (HOM)	×	×	×	×
Angular Second Moment (ASM)	×	✓	o	×
Energy (E)	✓	×	×	×
Entropy (ENT)	✓	×	×	×
Maximum Probability (MAX)	×	×	×	×
Mean	×	×	×	×
Variance (VAR)	✓	×	×	×
Correlation (COR)	×	×	✓	×

✓	the measures included in the final classification
o	the measures, which were left after analysis of correlation matrix and box-and-whisker plots, but not included in the final classification
×	the measures which were excluded after correlation matrix and box-and-whisker analysis

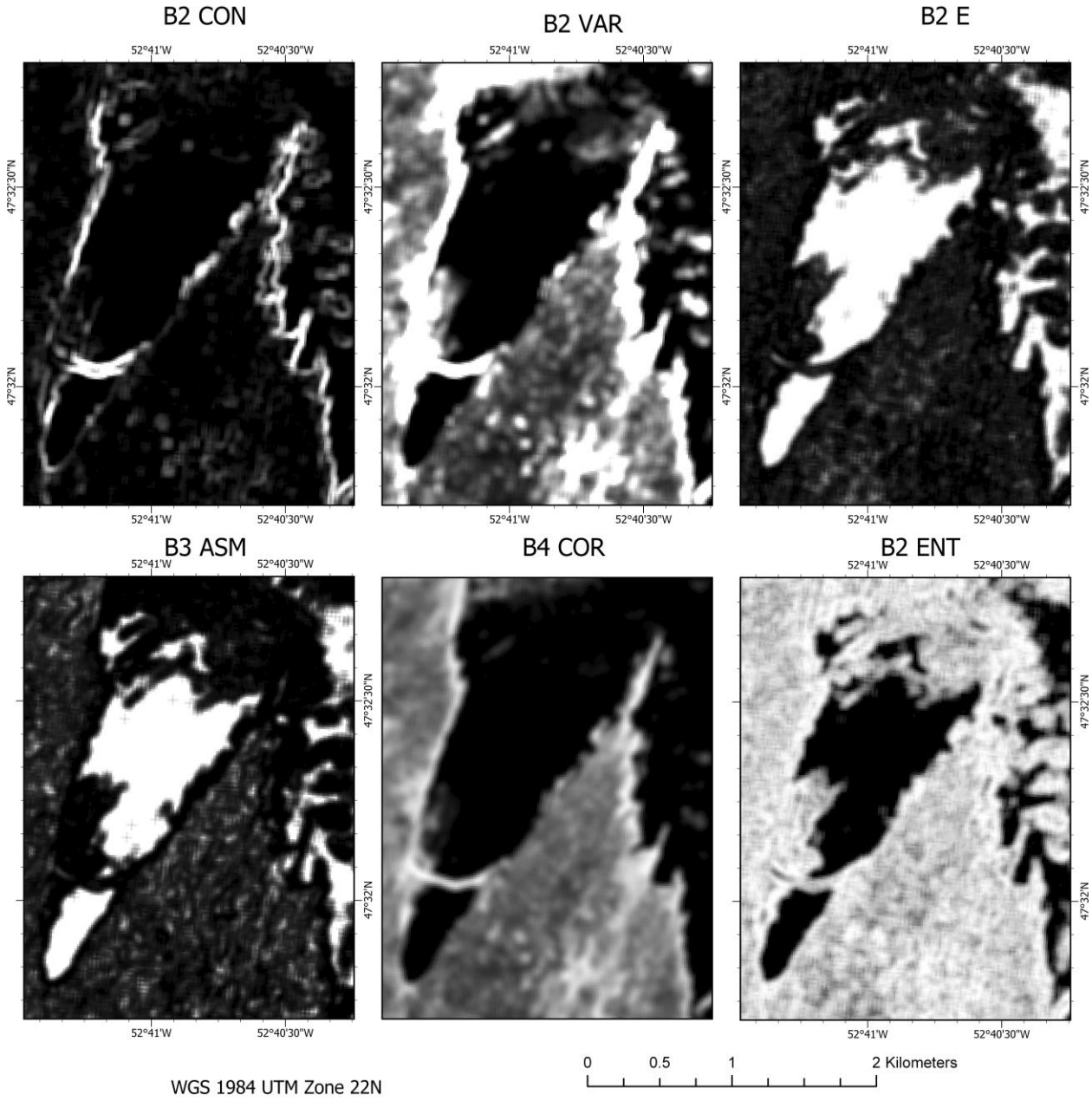

Figure 5.2. The most important GLCM texture measures.

Variable	σ°_{HH}	B4 COR	B3 ASM	B2 ENT	B2 VAR	B2 E	B2 CON	MNDWI	NDBI	Ratio 1	Ratio 2	PC7	PC6	PC5	PC4	PC3	PC2	PC1
σ°_{HH}	1.00	0.06	-0.04	0.04	0.00	-0.03	0.03	0.00	0.01	0.00	0.00	0.02	0.03	-0.04	0.03	-0.01	0.02	0.09
B4 CORR	0.06	1.00	0.46	0.75	0.80	0.55	0.53	-0.02	-0.01	0.00	0.00	-0.03	-0.05	-0.15	0.24	-0.01	-0.54	0.90
B3 ASM	-0.04	0.46	1.00	0.17	0.66	0.88	0.07	-0.01	0.01	0.00	0.00	-0.02	-0.02	-0.06	0.11	0.03	-0.45	0.39
B2 ENT	0.04	0.75	0.17	1.00	0.80	0.35	0.74	-0.01	0.00	0.00	0.00	-0.03	-0.07	-0.16	0.27	-0.04	-0.18	0.71
B2 VAR	0.00	0.80	0.66	0.80	1.00	0.83	0.50	-0.02	0.00	0.00	0.00	-0.06	-0.08	-0.18	0.30	-0.09	-0.39	0.72
B2 E	-0.03	0.55	0.88	0.35	0.83	1.00	0.22	-0.02	0.00	0.00	0.00	-0.04	-0.05	-0.15	0.23	-0.12	-0.43	0.47
B2 CON	0.03	0.53	0.07	0.74	0.50	0.22	1.00	-0.01	0.00	0.00	0.00	0.05	0.05	-0.15	0.21	-0.05	-0.16	0.48
MNDWI	0.00	-0.02	-0.01	-0.01	-0.02	-0.02	-0.01	1.00	0.00	0.00	0.00	0.00	0.00	0.01	0.00	-0.01	0.00	-0.02
NDBI	0.01	-0.01	0.01	0.00	0.00	0.00	0.00	0.00	1.00	0.00	0.00	-0.02	-0.02	0.01	0.01	0.01	0.08	0.04
Ratio 1	0.00	0.00	0.00	0.00	0.00	0.00	0.00	0.00	0.00	1.00	0.00	0.00	0.00	0.00	0.00	0.00	0.01	0.00
Ratio 2	0.00	0.00	0.00	0.00	0.00	0.00	0.00	0.00	0.00	0.00	1.00	0.00	0.00	0.00	0.00	0.00	0.00	0.00
PC7	0.02	-0.03	-0.02	-0.03	-0.06	-0.04	0.05	0.00	-0.02	0.00	0.00	1.00	0.00	0.01	-0.01	0.00	0.02	-0.03
PC6	0.03	-0.05	-0.02	-0.07	-0.08	-0.05	0.05	0.00	-0.02	0.00	0.00	0.00	1.00	0.01	-0.02	0.01	0.03	-0.06
PC5	-0.04	-0.15	-0.06	-0.16	-0.18	-0.15	-0.15	0.01	0.01	0.00	0.00	0.01	0.01	1.00	-0.06	0.02	0.07	-0.13
PC4	0.03	0.24	0.11	0.27	0.30	0.23	0.21	0.00	0.01	0.00	0.00	-0.01	-0.02	-0.06	1.00	-0.03	-0.11	0.22
PC3	-0.01	-0.01	0.03	-0.04	-0.09	-0.12	-0.05	-0.01	0.01	0.00	0.00	0.00	0.01	0.02	-0.03	1.00	0.03	-0.07
PC2	0.02	-0.54	-0.45	-0.18	-0.39	-0.43	-0.16	0.00	0.08	0.01	0.00	0.02	0.03	0.07	-0.11	0.03	1.00	-0.27
PC1	0.09	0.90	0.39	0.71	0.72	0.47	0.48	-0.02	0.04	0.00	0.00	-0.03	-0.06	-0.13	0.22	-0.07	-0.27	1.00

Figure 5.3. Correlation matrix of features selected for the final classification.

5.2 Classification

This Chapter presents the detailed description of results obtained during the object-based classification. Several classification scenarios were tested, and the model that produced the highest classification score was used to create the coastal land classification map. Finally, the results obtained from the coastal land classification map were further used to create a shoreline cover map. As a result, two classification maps were created: shoreline and coastal land cover maps. The coastal land cover map shows the polygons representing the surface types of the area within a two-km buffer from the shoreline, including foreshore and backshore zones. The shoreline cover map depicts the types of coastline, i.e., a line where land meets the ocean.

5.2.1 Segmentation

Setting the segmentation parameters has a major influence on the classification results. Several combinations of parameters were examined to find the optimal model with the best classification results. A two-level nested objects network was created using the MRS segmentation algorithm in the Trimble eCognition Developer 9.5.0. DEM and slope parameters were used for the first level segmentation, while the second level was generated based on the 10 m resolution VNIR bands.

Several parameter combinations were investigated to find the best model that allowed for creating the most meaningful real-world objects and ensuring the objects are internally homogenous, i.e., all pixels within an object should belong to one class.

In this research, the first segmentation level was constructed at a very fine scale, with the scale, shape, and compactness parameters of 10, 0.1, and 0.1, respectively. These parameters were determined by visual interpretation of the image segmentation results. It was essential to identify the borders of the shoreline zone, which allowed coastal zone separation from the other areas

during the next segmentation step. As an example, the superiority of using smaller scale parameters is demonstrated in Figure 5.4 (a) and (b). When the scale parameter was set to 20, the segments were too large and included not only the coastline zone but water and backshore zone. When the scale parameter of 10 was used, the polygons were narrower and followed the shoreline better. However, the second level of segmentation was still necessary to ensure that a segment belonged to a shoreline class and did not include water.

For the second segmentation level, the lowest values for shape and contrast parameters were chosen because Newfoundland's coastal zone is generally narrow. In some cases, it might be less than one pixel (10 m), especially for cliffs. As an example, Figure 5.4 (c) demonstrates the results when shape and compactness were set equal to 0.5. In this case, the objects become less extruded, which contradicts the nature of the shoreline feature. The use of weighting equal to 0.1 for these parameters produced better results (Figure 5.4 f).

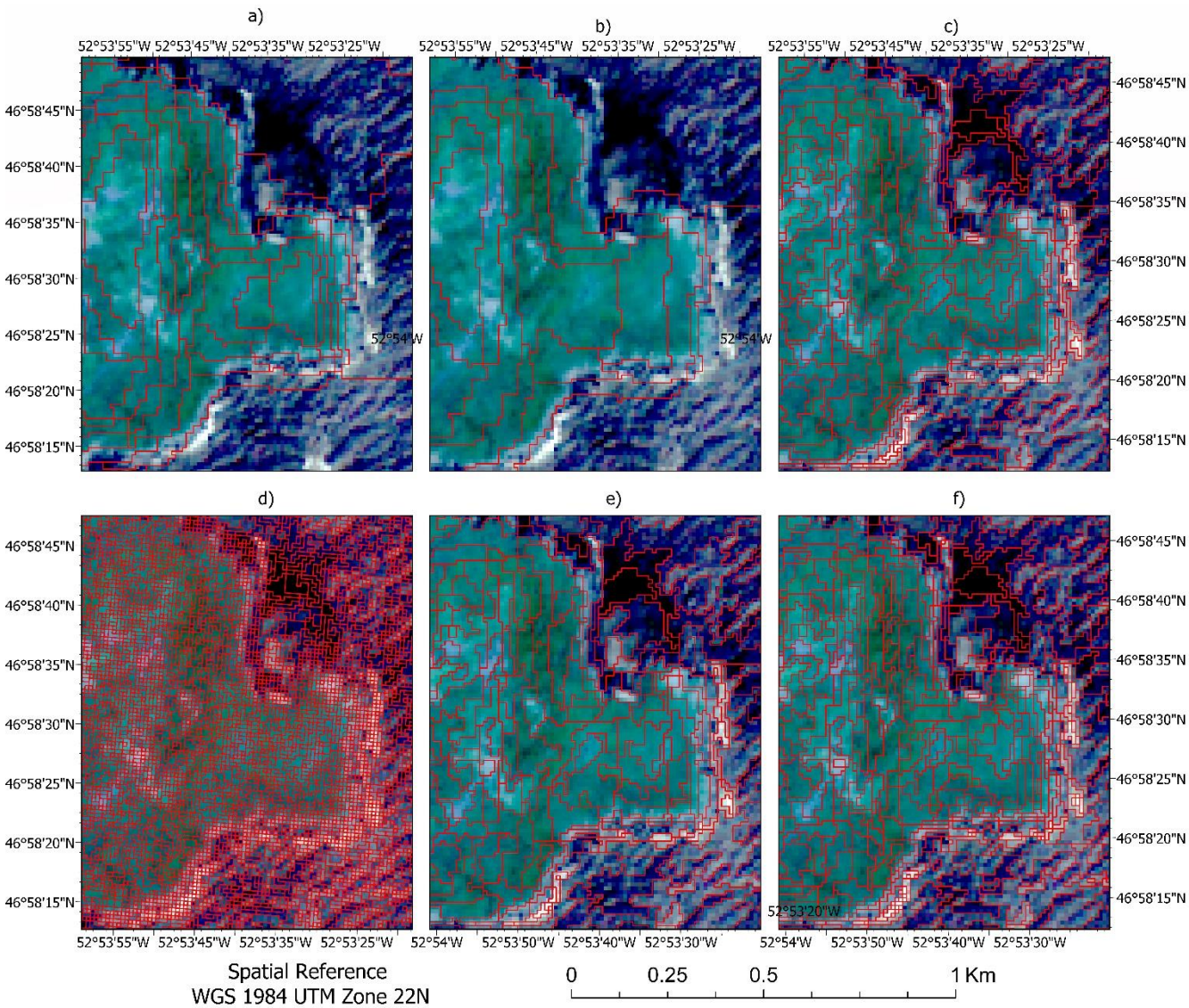

	Segmentation Level	Variables	Scale, Shape, and Compactness Parameters
a)	1	DEM, Slope	10, 0.1, 0.1
b)	1	DEM, Slope	20, 0.1, 0.1
c)	2	DEM, Slope	10, 0.1, 0.1
		VNIR	35, 0.5, 0.5
d)	2	DEM, Slope	10, 0.1, 0.1
		VNIR	10, 0.1, 0.1
e)	2	DEM, Slope	10, 0.1, 0.1
		VNIR	50, 0.1, 0.1
f)	2	DEM, Slope	10, 0.1, 0.1
		VNIR	35, 0.1, 0.1

Figure 5.4. Sentinel-2 image segmentation results obtained by applying various variables and parameters.

During visual image interpretation, it was found that the scale parameters between 30 and 40 produced the most meaningful results. Figure 5.4 (d) shows that the scale parameter of 10 results in too small objects, while the parameter of 50 (Figure 5.4 e) produces too large features, which may include several classes. The scale parameter of 30 demonstrates more acceptable results (Figure 5.4 f). Several classifications with various scale values were tested to find the combination of segmentation parameters leading to the best classification accuracy. As a result, the values of 35, 0.1, and 0.1 were chosen for scale, shape, and compactness, respectively.

Table 5.4. Shoreline classification accuracy and Kappa coefficients of segmented images with various scale parameters

Segmentation Scale Parameter	Overall Accuracy	Kappa Coefficient
10	0.522	0.454
15	0.612	0.554
20	0.705	0.660
25	0.731	0.692
30	0.773	0.740
35	0.774	0.741
40	0.741	0.703

5.2.2 Classification Scenarios

Table 5.5 shows various classification scenarios tested to find the best combination of input variables producing the highest classification results. The effect of principal components was explored by testing the scenarios with and without principal components (scenarios 2 and 1). The effect of using textural measures was assessed in scenarios 3 (when only the measures remained after the feature selection process) and 5 (when texture measures were applied along with the spectral indices, principal components, and Sentinel-1 data). Spectral indices were included in scenarios 4 (where the selected indices were used along principal components and terrain parameters), 6 and 7 (where indices were utilized along with texture features and Sentinel-1 data), and 10 (where only a reduced amount of indices were used). The effect of adding Sentinel-1 data

to the classification model was also investigated in scenarios 8 (where only HH data were used) and 10 (where only HV data were utilized). Also, it should be noted that since a DEM and slope parameters play a crucial role in defining shoreline class, these variables were used in all of the scenarios.

Table 5.5. Classification scenarios tested in this research

Classification Scenario	Description	Predictor variables	
		Mean	St. dev.
Scenario 1	Sentinel-2 bands Terrain parameters	B2-B8a, B11-B12; DEM, slope	B2-B4
Scenario 2	Sentinel-2 bands Principal components Terrain parameters	B2-B8a, B11-B12; PC1-PC10; DEM, slope	B2-B4, PC1-PC3
Scenario 3	Principal components Terrain parameters Texture measures	PC1-PC10; DEM, slope; B2 CON, E, VAR, ENT; B3 CON, ASM, DISS; B4 COR, ASM	PC1-PC3
Scenario 4	Principal components Terrain parameters Spectral indices	PC1-PC10; DEM, slope; NDPI, MNDWI, IRECI, GNDVI, IPVI, NDWI, CI	PC1-PC3
Scenario 7	Principal components Terrain parameters Spectral indices Texture measures SAR	PC1-PC10; DEM, slope; NDPI, MNDWI, IRECI, GNDVI, IPVI, NDWI, CI; B2 CON, E, VAR, ENT; B3 CON, ASM, DISS; B4 COR, ASM; $\overset{\circ}{\sigma}_{HH}$, $\overset{\circ}{\sigma}_{HV}$	PC1-PC3
Scenario 6	Principal components Terrain parameters Spectral indices SAR	PC1-PC10, DEM, slope, NDPI, MNDWI, IRECI, GNDVI, IPVI, NDWI, CI; $\overset{\circ}{\sigma}_{HH}$, $\overset{\circ}{\sigma}_{HV}$	PC1-PC3
Scenario 5	Principal components Terrain parameters Texture measures SAR	PC1-PC10; DEM, slope; B2 CON, E, VAR, ENT; B3 CON, ASM, DISS; B4 COR, ASM; $\overset{\circ}{\sigma}_{HH}$, $\overset{\circ}{\sigma}_{HV}$	PC1-PC3
Scenario 9		PC1-PC10, DEM, slope, B2 CON, E, VAR, ENT; B3 ASM; B4 COR; $\overset{\circ}{\sigma}_{HV}$	PC1-PC3
Scenario 8		PC1-PC10, DEM, slope, B2 CON, E, VAR, ENT; B3 ASM; B4 COR; $\overset{\circ}{\sigma}_{HH}$	PC1-PC3
Scenario 10	Principal components Terrain parameters Spectral indices Texture measures SAR	PC1-PC7, DEM, slope; NDBI, $\frac{B4-B8a}{B4+B8a}$, $\frac{B8a-B2}{B8a+B2}$, MNDWI; B2 CON, E, VAR, ENT; B3 ASM; B4 CORR; $\overset{\circ}{\sigma}_{HH}$	PC1-PC3

Error matrices were created for each model to assess the results and to determine the most accurate model. The lowest OA of 77.42% was achieved using a DEM and Sentinel- 2 bands,

including VIS, two NIR, three RE, and two SWIR bands (scenario 1). The lowest UA and PA were found for the *bedrock platform* and *man-made* classes. As seen in Table 5.6, the *man-made* class was misclassified with *sand*, *bedrock platform*, and *pebble/cobble*. High omission errors were also found for *bedrock cliff* and *pebble/cobble*, which were misclassified with *bedrock platform* and *sand*, respectively.

Table 5.6. Confusion matrix obtained from the classification scenario 1

Classified \ Reference Data	Water	Forest	Sand	Man-Made	Grass	Pebble Cobble	Bedrock Cliff	Bedrock Platform	Total
Water	340	0	0	0	0	3	3	0	346
Forest	0	158	0	0	1	0	3	11	173
Sand	0	0	279	83	0	78	0	15	455
Man-Made	0	0	3	132	3	1	9	0	148
Grass	0	0	0	15	291	0	17	3	326
Pebble Cobble	0	0	0	22	6	140	3	0	171
Bedrock Cliff	0	0	8	16	4	11	161	15	215
Bedrock Platform	0	33	0	32	3	0	82	155	305
Total	340	191	290	300	308	233	278	199	
PA	1	0.827	0.962	0.440	0.945	0.601	0.579	0.779	
UA	0.983	0.913	0.613	0.892	0.893	0.819	0.749	0.508	
OA	0.774								
KIA	0.741								

PA represents the Producer's Accuracy,
UA represents the User's Accuracy
OA is Overall Accuracy,
KIA is the Kappa index of agreement.

Scenario 1 results were improved by adding the principal components to input variables (scenario 2). In this case, the achieved OA was 79.66%. Although most of the PAs were slightly improved, the PA of *bedrock cliff* was decreased, and this class appeared to have the highest omission error. *Bedrock cliff* was misclassified with *bedrock platform* mostly as well as *sand* and *man-made*.

Table 5.7. Confusion matrix obtained from the classification scenario 2

Classified \ Reference Data	Water	Forest	Sand	Man-Made	Grass	Pebble Cobble	Bedrock Cliff	Bedrock Platform	Total
Water	340	0	0	0	0	0	6	0	346
Forest	0	184	0	0	1	0	0	6	191
Sand	0	0	279	66	0	71	21	0	437
Man-Made	0	0	3	148	0	12	25	0	188
Grass	0	0	0	11	294	0	15	3	323
Pebble Cobble	0	0	0	35	6	150	4	0	195
Bedrock Cliff	0	0	8	4	4	0	134	15	165
Bedrock Platform	0	7	0	36	3	0	73	175	294
Total	340	191	290	300	308	233	278	199	
PA	1	0.963	0.962	0.493	0.955	0.644	0.482	0.879	
UA	0.983	0.963	0.638	0.787	0.910	0.769	0.812	0.595	
OA	0.797								
KIA	0.767								

PA represents the Producer's Accuracy,
UA represents the User's Accuracy
OA is Overall Accuracy,
KIA is the Kappa index of agreement.

Scenarios 3 and 4 were tested to assess the importance of textural and spectral indices along with principal components and DEM. The use of texture measures (scenario 3) resulted in an increased OA, achieving 81.90%. In this case, the following texture variables were used: CON, E, VAR, ENT of the red band; CON, ASM, DISS of the green band; and COR and ASM of the blue band. The greatest improvement of PAs was found for *forest* and *pebble/cobble* classes, which were 17% and 20% higher, respectively, compared to that of scenario 1 (Table 5.8). This indicates that adding textural features to input variables improves the resulting accuracy. However, the use of more textural images cannot further improve classification accuracy because of the high correlation between them. In contrast, the score was even lower (81.40%) when attempting to incorporate all 30 texture measures for the visible bands (scenario 3).

Table 5.8. Confusion matrix obtained from the classification scenario 3

Classified \ Reference Data	Water	Forest	Sand	Man-Made	Grass	Pebble Cobble	Bedrock Cliff	Bedrock Platform	Total
Water	340	0	0	0	0	0	10	0	350
Forest	0	191	0	0	2	0	0	0	193
Sand	0	0	277	70	0	34	27	0	408
Man-Made	0	0	3	165	27	12	0	0	207
Grass	0	0	0	8	267	0	0	0	275
Pebble Cobble	0	0	0	16	11	187	4	0	218
Bedrock Cliff	0	0	0	0	0	0	186	60	246
Bedrock Platform	0	0	10	41	1	0	51	139	242
Total	340	191	290	300	308	233	278	199	
PA	1	1	0.955	0.550	0.867	0.803	0.669	0.698	
UA	0.971	0.990	0.679	0.797	0.971	0.858	0.756	0.574	
OA	0.819								
KIA	0.792								

PA represents the Producer's Accuracy,
UA represents the User's Accuracy
OA is Overall Accuracy,
KIA is the Kappa index of agreement.

Scenario 4, containing spectral indices along with principal components and DEM data, also demonstrated improved results (Table 5.9). However, the obtained OA of 81.25% was lower than that of scenario 3, in which texture measures were used. The most significant omission error in scenario 4 was achieved by the *man-made* class, which was misclassified with *sand* and *pebble/cobble*. The highest omission error was obtained for the *bedrock platform*, which was misclassified with the *bedrock cliff*.

The incorporation of SAR data with texture measures resulted in the OA of 84.20% (Table 5.10), while the combination of SAR data and spectral indices led to the OA of 84.71% (Table 5.11). In both scenarios 5 and 6, the lowest PA was obtained for the *man-made* class, which was mainly misclassified with *bedrock cliff* and *pebble/cobble*, while the lowest UAs were found for *bedrock cliff* and *platform*.

Table 5.9. Confusion matrix obtained from the classification scenario 4

Classified \ Reference Data	Water	Forest	Sand	Man-Made	Grass	Pebble Cobble	Bedrock Cliff	Bedrock Platform	Total
Water	340	0	0	0	0	1	10	0	351
Forest	0	184	0	0	15	0	0	0	199
Sand	0	0	269	79	0	17	0	9	374
Man-Made	0	3	11	157	0	12	0	0	183
Grass	0	0	0	8	279	0	0	0	287
Pebble Cobble	0	0	0	44	7	203	4	0	258
Bedrock Cliff	0	4	10	4	1	0	172	56	247
Bedrock Platform	0	0	0	8	6	0	92	134	240
Total	340	191	290	300	308	233	278	199	
PA	1	0.963	0.928	0.523	0.906	0.871	0.619	0.673	
UA	0.969	0.925	0.719	0.858	0.972	0.787	0.696	0.558	
OA	0.813								
KIA	0.785								

PA represents the Producer's Accuracy,
UA represents the User's Accuracy
OA is Overall Accuracy,
KIA is the Kappa index of agreement.

Table 5.10. Confusion matrix obtained from the classification scenario 5

Classified \ Reference Data	Water	Forest	Sand	Man-Made	Grass	Pebble Cobble	Bedrock Cliff	Bedrock Platform	Total
Water	340	0	10	0	1	0	10	0	361
Forest	0	188	0	0	2	0	0	0	190
Sand	0	0	269	0	0	0	1	0	270
Man-Made	0	0	11	168	27	12	0	0	218
Grass	0	0	0	19	267	0	0	0	286
Pebble Cobble	0	0	0	26	6	218	5	0	255
Bedrock Cliff	0	0	0	46	0	3	212	60	321
Bedrock Platform	0	3	0	41	5	0	50	139	238
Total	340	191	290	300	308	233	278	199	
PA	1	0.984	0.928	0.560	0.867	0.936	0.763	0.698	
UA	0.942	0.989	0.996	0.771	0.934	0.855	0.660	0.584	
OA	0.842								
KIA	0.819								

PA represents the Producer's Accuracy,
UA represents the User's Accuracy
OA is Overall Accuracy,
KIA is the Kappa index of agreement.

Table 5.11. Confusion matrix obtained from the classification scenario 6

Classified \ Reference Data	Water	Forest	Sand	Man-Made	Grass	Pebble Cobble	Bedrock Cliff	Bedrock Platform	Total
Water	340	0	10	0	1	0	10	0	361
Forest	0	184	0	0	0	0	0	0	184
Sand	0	0	269	20	0	0	1	0	290
Man-Made	0	0	11	203	0	12	0	0	226
Grass	0	0	0	8	294	0	0	0	302
Pebble Cobble	0	0	0	27	6	221	5	0	259
Bedrock Cliff	0	7	0	34	0	0	171	69	281
Bedrock Platform	0	0	0	8	7	0	91	130	236
Total	340	191	290	300	308	233	278	199	
PA	1	0.963	0.928	0.677	0.955	0.948	0.615	0.653	
UA	1	0.960	0.916	0.638	0.947	0.941	0.557	0.610	
OA	0.847								
KIA	0.825								

PA represents the Producer's Accuracy,
UA represents the User's Accuracy
OA is Overall Accuracy,
KIA is the Kappa index of agreement.

Adding all features, including spectral indices, texture, SAR data, Principal components, and DEM data, to the classification scheme lead to OA of 83.54% (Table 5.12), which was less than the ones obtained from scenario 6 and 5 (84.71% and 84.20%, respectively).

Table 5.12. Confusion matrix obtained from the classification scenario 7

Classified \ Reference Data	Water	Forest	Sand	Man-Made	Grass	Pebble Cobble	Bedrock Cliff	Bedrock Platform	Total
Water	340	0	10	0	1	0	10	0	361
Forest	0	184	0	0	0	0	0	0	184
Sand	0	0	269	29	0	0	1	0	299
Man-Made	0	0	11	172	9	12	0	0	204
Grass	0	0	0	8	285	0	0	0	293
Pebble Cobble	0	0	0	45	6	221	5	0	277
Bedrock Cliff	0	0	0	46	0	0	186	69	301
Bedrock Platform	0	7	0	0	7	0	76	130	220
Total	340	191	290	300	308	233	278	199	
PA	1	0.963	0.928	0.573	0.925	0.948	0.669	0.653	
UA	0.942	1	0.900	0.843	0.973	0.798	0.618	0.591	
OA	0.835								
KIA	0.811								

PA represents the Producer's Accuracy,
UA represents the User's Accuracy
OA is Overall Accuracy,
KIA is the Kappa index of agreement.

Scenarios 8 and 9 used HH and HV separately. The overall accuracies were 85.60% (Table 5.13) and 84.34% (Table 5.14), respectively. It is worth noting that the result was lower when both HH and HV data were used (scenario 5) compared to the results obtained by using HH channel data. It might be explained by that HH and HV contain similar information and the exclusion of HV could reduce the degree of correlation amongst individual trees in the RF, which improved the classification OA.

Table 5.13. Confusion matrix obtained from the classification scenario 8

Classified \ Reference Data	Water	Forest	Sand	Man-Made	Grass	Pebble Cobble	Bedrock Cliff	Bedrock Platform	Total
Water	340	0	10	0	1	0	10	0	361
Forest	0	188	0	0	2	0	0	0	190
Sand	0	0	269	0	1	0	1	0	271
Man-Made	0	0	3	190	27	1	0	0	221
Grass	0	0	0	12	267	0	0	0	279
Pebble Cobble	0	0	8	26	6	229	5	0	274
Bedrock Cliff	0	0	0	50	0	3	212	64	329
Bedrock Platform	0	3	0	22	4	0	50	135	214
Total	340	191	290	300	308	233	278	199	
PA	1	0.984	0.928	0.633	0.867	0.983	0.763	0.678	
UA	0.942	0.989	0.993	0.860	0.957	0.836	0.644	0.631	
OA	0.856								
KIA	0.834								

PA represents the Producer's Accuracy,
UA represents the User's Accuracy
OA is Overall Accuracy,
KIA is the Kappa index of agreement.

Table 5.14. Confusion matrix obtained from the classification scenario 9

Classified \ Reference Data	Water	Forest	Sand	Man-Made	Grass	Pebble Cobble	Bedrock Cliff	Bedrock Platform	Total
Water	340	0	0	0	1	0	10	0	351
Forest	0	187	0	0	2	0	0	0	189
Sand	0	0	279	31	1	0	26	0	337
Man-Made	0	0	3	183	27	1	0	0	214
Grass	0	0	0	19	267	0	0	0	286
Pebble Cobble	0	0	8	26	6	232	5	0	277
Bedrock Cliff	0	0	0	0	0	0	186	69	255
Bedrock Platform	0	4	0	41	4	0	51	130	230
Total	340	191	290	300	308	233	278	199	
PA	1	0.979	0.962	0.610	0.867	0.996	0.669	0.653	
UA	0.969	0.989	0.828	0.855	0.934	0.838	0.729	0.565	
OA	0.843								
KIA	0.820								

PA represents the Producer's Accuracy,
UA represents the User's Accuracy
OA is Overall Accuracy,
KIA is the Kappa index of agreement.

The best results were obtained by applying scenario 10, which included the following input layers: PC1-PC7, spectral indices (NDVI, MNDWI, Ratio 1, and Ratio 2), texture measures (CON, E, VAR, ENT of red; ASM of green; and CORR of blue bands), σ_{HH}°. In this case, the OA reached 87.10%.

Table 5.15 demonstrated the error matrix of the classification scenario 10, achieving the highest OA score. The minor omission errors were obtained for the *water* class, while commission errors were minimal for vegetated classes, including *grass* and *forest*. PA for the *man-made* class was low, achieving only 64.7%. This indicated the misclassification of *man-made* class with other classes, mostly with *bedrock cliff*, *pebble/cobble*, and *sand*.

Table 5.15. Confusion matrix obtained from the classification scenario 10

Classified\ Referenced data	Water	Forest	Sand	Man-Made	Grass	Pebble Cobble	Bedrock Cliff	Bedrock Platform	Total
Water	340	0	10	0	1	0	10	0	361
Forest	0	184	0	0	0	0	0	5	189
Sand	0	0	269	31	0	0	0	0	300
Man-Made	0	0	11	194	0	12	0	0	217
Grass	0	0	0	8	296	0	0	0	304
Pebble Cobble	0	0	0	10	6	221	1	0	238
Bedrock Cliff	0	0	0	48	0	0	212	47	307
Bedrock Platform	0	7	0	9	5	0	55	147	223
Total	340	191	290	300	308	233	278	199	
PA	1	0.963	0.928	0.647	0.961	0.948	0.763	0.739	
UA	0.942	0.974	0.897	0.894	0.974	0.929	0.691	0.659	
OA	0.871								
KIA	0.852								

PA represents the Producer's Accuracy,
UA represents the User's Accuracy
OA is Overall Accuracy,
KIA is the Kappa index of agreement.

The final coastal land classification map is presented in Figure 5.5, and the subsets of zoomed areas can be seen in Figure 5.6.

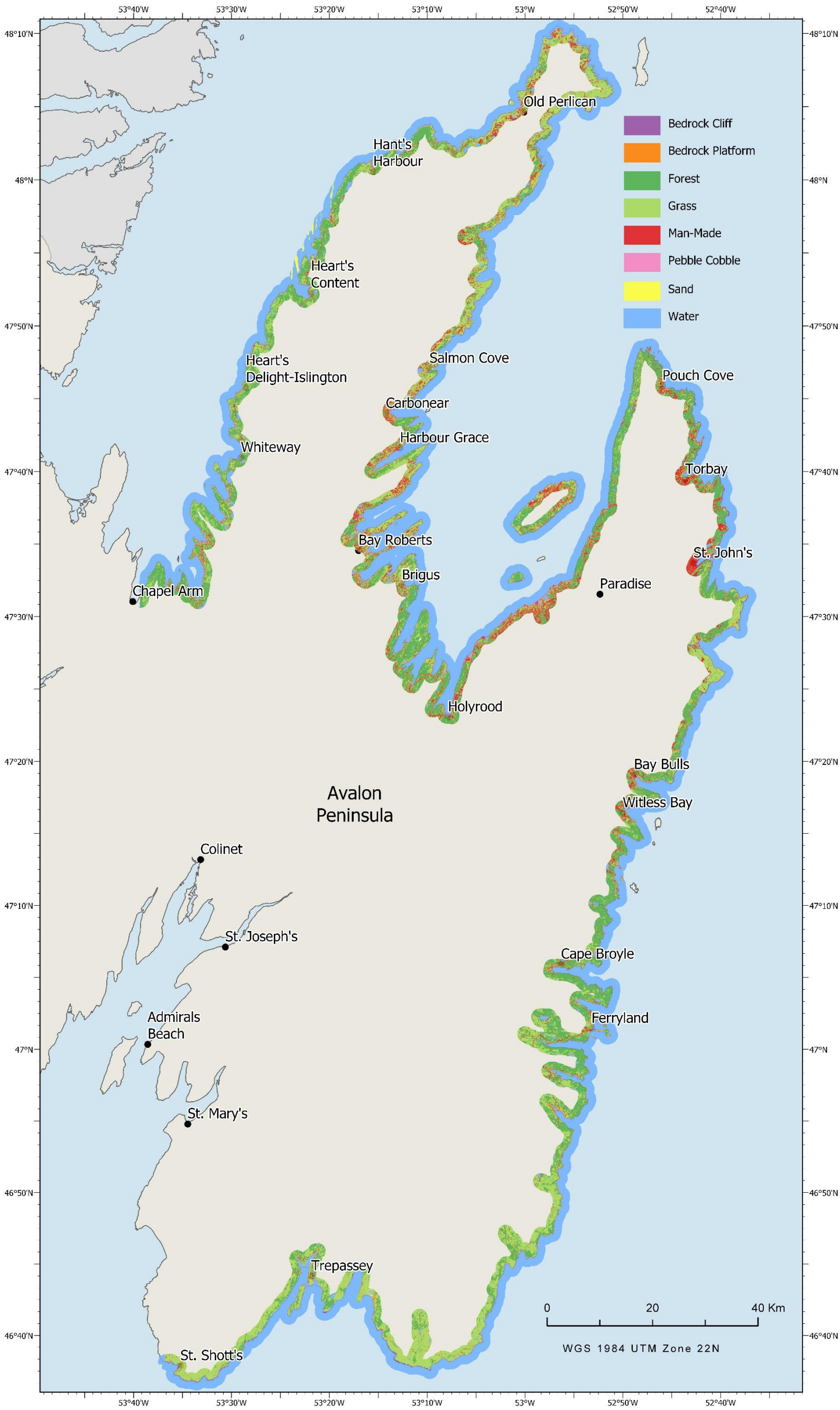

Figure 5.5. Coastal land classification.

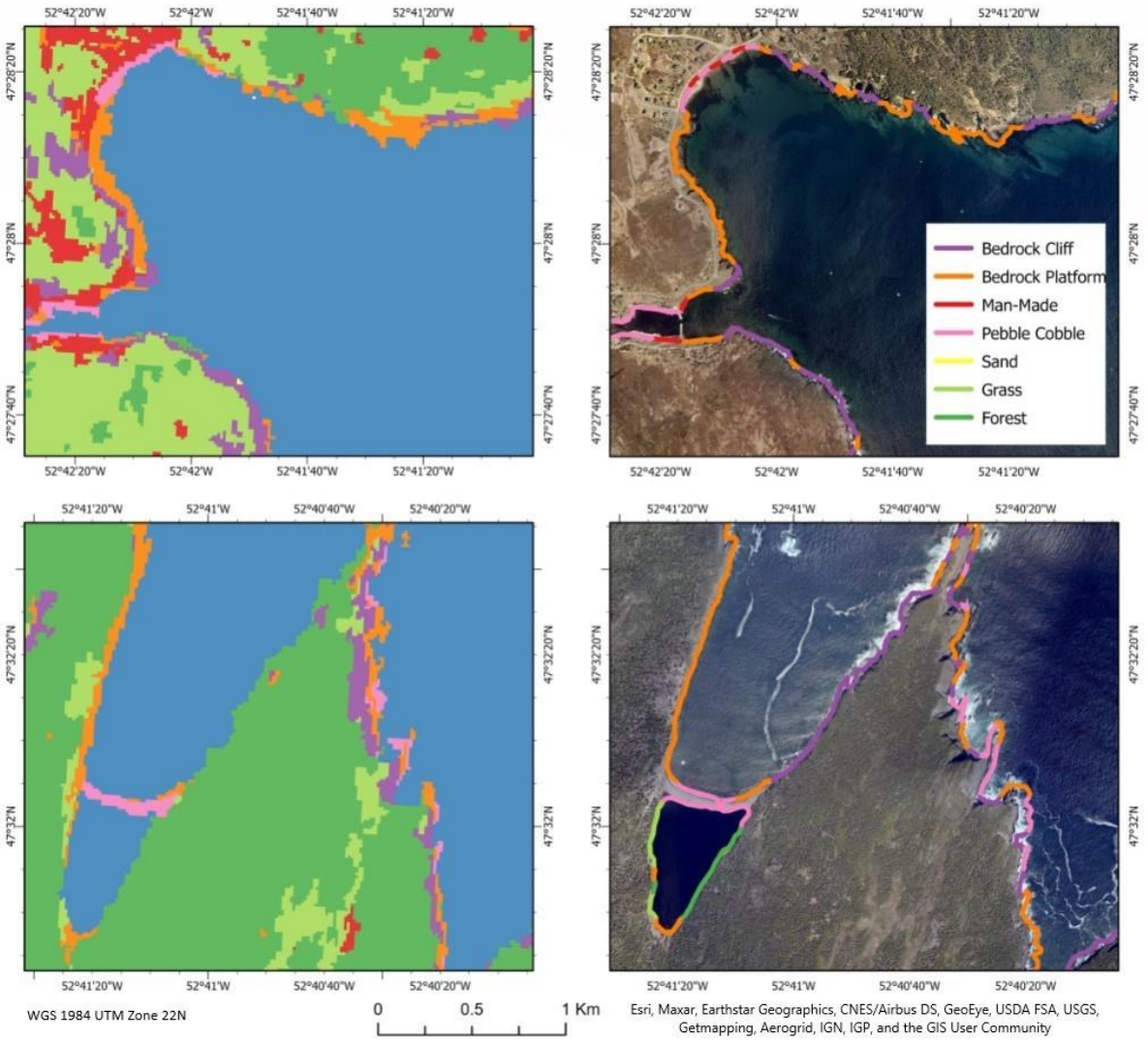

Figure 5.6. The subsets of coastal land cover map and shoreline classification on aerial photography.

Summarizing the results obtained from all the scenarios (Figure 5.7 and Figure 5.8), *water* and *forest* classes were classified best by all the models. In contrast, *man-made* and *bedrock platform* features had the lowest PAs (57.06%) and UAs (58.5%), respectively, on average in all the models. The average PAs and UAs of all classes varied from 76.66% to 86.86% and 79.63% to 87%. The lowest OA (74.42%) was obtained in scenario 1, while the highest OA (87.10%) was achieved by scenario 10.

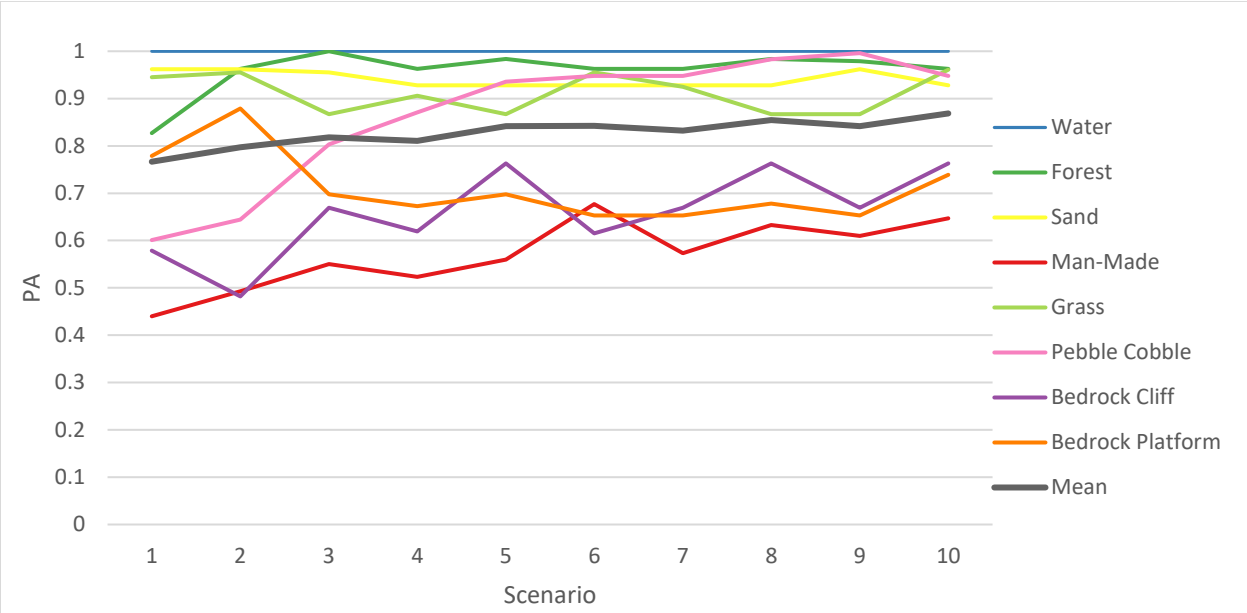

Figure 5.7. PAs for coastal land cover types obtained in different scenarios.

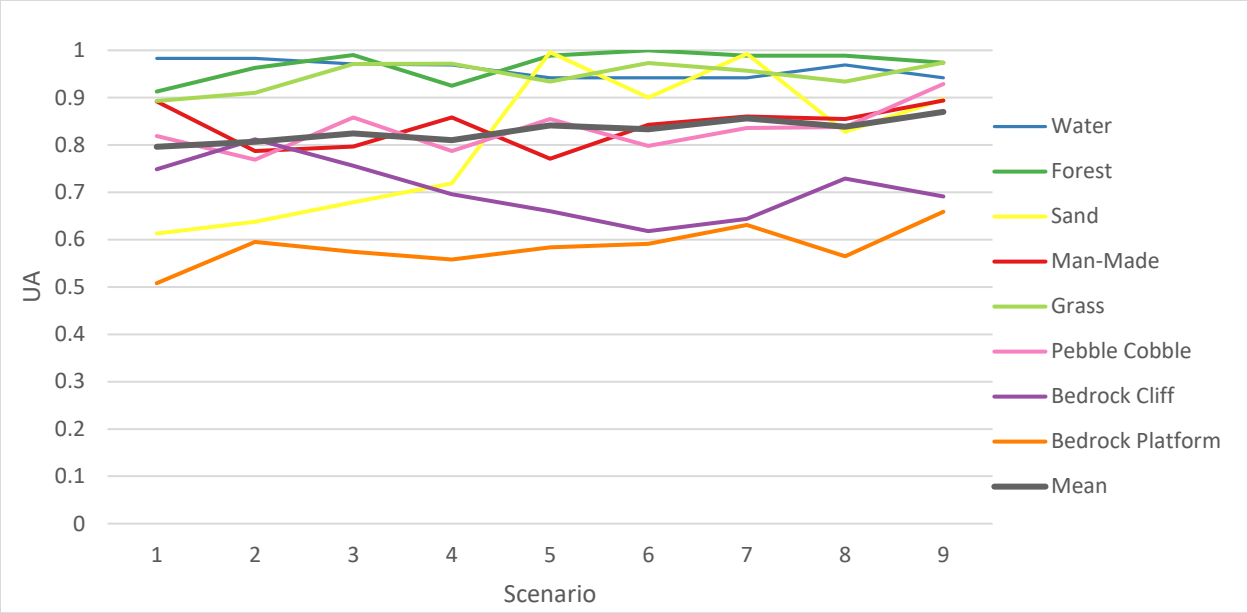

Figure 5.8. UAs for coastal land cover types obtained in different scenarios.

The evaluation of whether the differences between classification accuracies obtained from various scenarios are statistically significant was conducted through the calculation of z score and X^2 values described previously in Chapter 4.5.

The obtained X^2 value is compared against the tabulated chi-squared values. In our case, the appropriate critical value for the 5% level (with one degree of freedom) is 3.841. Thus, the decision to reject the H_0 (of no significant difference) was taken if X^2 less than 3.841 or if $|z|$ is less than 1.96. The resulting z score presented in Table 5.17 demonstrated that H_0 was rejected for the majority of the combinations of classification scenarios. However, the differences between scenarios 3 and 4, 5 and 6, 5 and 7, 5 and 9, 6 and 8, and 6 and 9 were not found statistically significant.

Table 5.16. *z* score obtained from comparison accuracies from different classification scenarios

		Classification scenario									
		1	2	3	4	5	6	7	8	9	10
Classification scenario	1										
	2	4.75									
	3	7.16	3.60								
	4	6.33	2.64	1.67							
	5	9.26	6.22	5.82	6.75						
	6	10.38	7.31	5.11	8.07	1.01					
	7	8.98	5.71	3.84	6.49	1.75	3.37				
	8	10.36	7.53	7.51	8.54	4.77	1.82	4.84			
	9	9.44	6.40	5.89	6.67	0.35	0.86	2.34	3.61		
	10	13.28	10.37	9.35	11.18	7.41	6.14	8.72	4.37	5.70	

- the null hypothesis of no significant difference is rejected

- the null hypothesis of no significant difference is not rejected

The results obtained from scenario 10 were used to create the shoreline classification map. The polyline shape file representing the shoreline was divided into 50 m long segments. Each segment was then assigned to a class based on the information of the closest polygon of the previously obtained coastal land classification map shown in Figure 5.5.

Since *forest* and *grass* are located over the *cliffs*, technically, these classes' intertidal zones are represented by cliffs, not vegetation. Therefore, these classes were collapsed and assigned as the *bedrock cliff* class. As a result, a map depicting five shoreline types was created (Figure 5.9). These classes included *bedrock cliff*, *bedrock platform*, *man-made*, *sand*, and *pebble/cobble*. OA of the final shoreline classification map achieved 84.75% (Table 5.17).

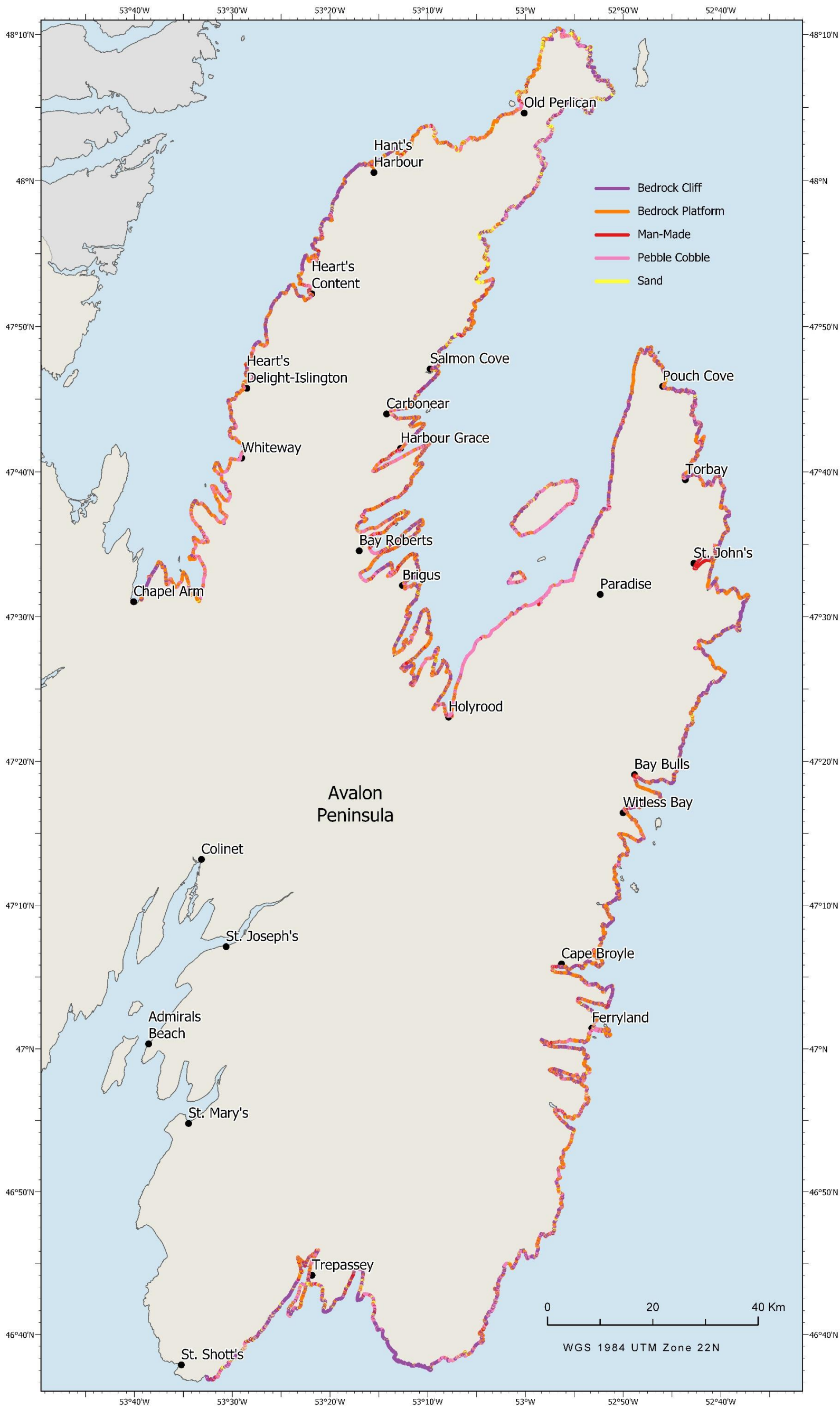

Figure 5.9 Shoreline classification map.

Table 5.17 Shoreline classification confusion matrix

Classified\ Referenced data	Bedrock Cliff	Bedrock Platform	Man-Made	Sand	Pebble Cobble	Total
Bedrock Cliff	105	6	0	0	0	111
Bedrock Platform	7	26	0	0	0	33
Man-Made	0	0	36	0	0	36
Sand	0	0	0	25	4	29
Pebble Cobble	6	0	9	13	58	86
Total	118	32	45	38	62	295
PA	0.890	0.813	0.800	0.658	0.935	
UA	0.946	0.788	1.000	0.862	0.674	
OA	0.847					
KIA	0.795					

PA represents the Producer's Accuracy,
UA represents the User's Accuracy
OA is Overall Accuracy,
KIA is the Kappa index of agreement.

The lowest PA (65.79%) and UA (67.44%) were obtained by *sand* and *pebble/cobble* classes Table 5.17, which were misclassified with each other due to the similarity of their spectral characteristics and were discussed in Figure 5.1.

According to the shoreline classification map, the *bedrock cliffs* and *platform* were found to be the most dominating shoreline types in the study area (Figure 5.10). They covered around 387 km and 369 km out of a total of 1089 km of the shoreline. In contrast, *sand* and *man-made* were the least common, covering only 49 km and 57 km respectively.

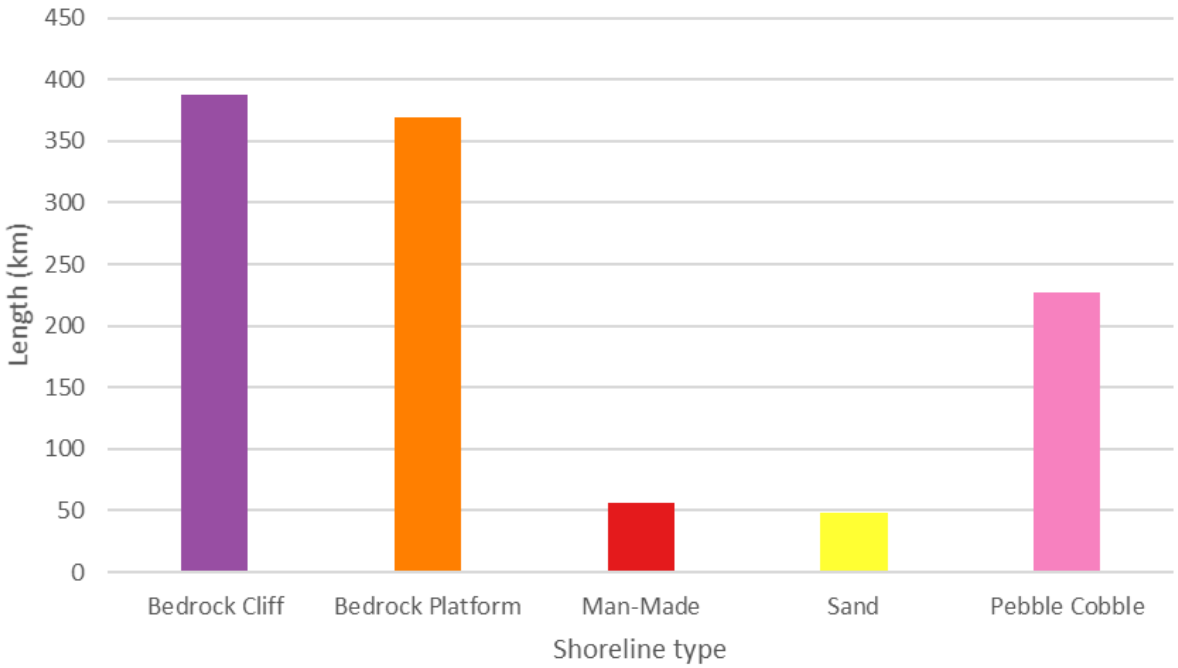

Figure 5.10. The distribution of classified shoreline classes along the study area.

6. Discussion

The following chapters discuss the findings of this research, with special emphasis on classification scheme, feature extraction and selection, and classification results.

6.1 Classification Scheme

In this research, two classification maps were created: shoreline and coastal land cover maps. The coastal land cover map depicts the polygons representing different types of surfaces within a two km buffer from the shoreline. This area covers foreshore and backshore zones. The shoreline cover map depicts the line representing various sediment types of a coastline, i.e., a line that forms the boundary between the land and the ocean.

For both maps, the ECCC SCAT classification scheme was adapted. The ECCC classification scheme includes 25 shoreline types representing the full range of substrates and shoreline form (Demers et al., 2015; Wynja et al., 2014). Since satellite data have a coarser spatial resolution compared to helicopter videography data, such detailed discrimination used in SCAT was not possible for the satellite-based discrimination in this research. The more general classes had to be adapted from the SCAT to avoid interclass confusion while maintaining a useful level of shoreline type's differentiation in terms of their sensitivity to oil spills. As was demonstrated in previous studies (Y. Chen et al., 2007; Banks et al., 2014b, 2015; Demers et al., 2015), the number of classes that can be extracted from satellite data depends on the spatial and spectral characteristics of the sensor and the nature of the shoreline. Since this research is the first attempt at using Sentinel-1 and -2 data for shoreline classification for oil spill response in Newfoundland, the SCAT classification scheme was adapted based on the exploratory analysis of spectral signatures of shore and near-shore features.

Additional classes, such as *water*, *forest*, and *grass*, were added to the classification scheme. The intertidal zone for *bedrock cliffs* is generally narrow in the study area. Therefore, the *forest* and the *grass* classes were used as proxies for the *cliffs* as vegetation layers are located over the cliffs intertidal zone. The decision to keep vegetation classes for a coastal zone classification was made because the difference between these land cover types affects the choice of an appropriate oil spill response technique and provides valuable information about backshore areas. However, the *forest* and *grass* classes were merged with the *bedrock cliff* class for the final shoreline classification.

Also, *man-made* and *roads* were used as separate subclasses for building learning databases, as they have different spectral characteristics, as shown in Figure 5.1. However, they were later combined for the final classification due to the similarity of oil spill response techniques (ECCC, 2018). Similarly, bedrock high and low cliffs were merged into one category. Also, bedrock platforms having flat and rough surfaces forming the *bedrock platform* class.

In total, the coastal land classification map included eight classes, such as *man-made*, b*edrock platform*, b*edrock cliff*, *pebble/cobble beach or bank*, s*and beach or bank*, f*orest*, g*rass*, and w*ater*. The final shoreline classification map depicts five classes, including *bedrock cliff*, *bedrock platform*, *man-made*, *sand*, and *pebble/cobble*.

6.2 Feature Extraction & Selection

The analysis of Sentinel-2 bands box-and-whiskers plots demonstrated the similarity of non-vegetation classes' pixel distribution in one band. Also, large variability of *man-made* features was observed in all the bands. This happened because the *man-made* class was not spectrally homogeneous and includes features, e.g., roofs, with different colors. The *water* class was the most easily distinguished from all the other classes due to its small variability and low pixel values.

The smallest variability in the visible spectral bands was found for *forest* class with low pixel values due to chlorophyll's properties. Chlorophyll strongly absorbs light at blue and red; therefore, the lowest forest pixel values were found in B2 and B4. The reflection of chlorophyll is higher in a green light, which can also be seen with Figure 5.3. However, healthy plants have a high reflectance in the near-infrared. This agrees with Figures 5.8. and 5.9, which presents the distribution of pixels in NIR and near-NIR, where the pixel values of the forest are much higher than in visible bands shown in Figures 5.2-5.4.

As a result of the spectral profile and box-and-whisker plots investigation, it was found that the *man-made* category had a different response than the *road* class. An increased difference between these features' responses may be observed in visible and SWIR bands (Figures 5.1, 5.10, and 5.11). This is likely due to different spectral characteristics of features that represent these classes: the *man-made* class includes mostly buildings and structures having roofs of various colors, while the *road* is represented by homogenous gray asphalt.

In general, the box-and-whisker plots demonstrated that Sentinel-2 bands did not provide a good capability to separate between non-vegetated classes. The largest separability potential among these classes was found between the *high bedrock cliff* and *bedrock platform*. Therefore, the generation of additional features, including spectral indices and band ratios, was implemented. This suppresses the topographic variation and enhances the spectral difference between bands (Rajendran et al., 2012; Jensen, 2016).

The correlation matrix (Appendix B) demonstrates a high correlation between the Sentinel-2 visible bands. This agrees with the box-and-whisker plots, which demonstrate similar pixel distribution of coastal land classes. A high correlation was also observed between the bands 5-8a and 11-12. Such an extensive inter-band correlation problem frequently occurs in multispectral

image data analysis due to the similarity of information generated from various wavelength bands (Lillesand & Kiefer, 2000). Therefore, PCA was applied to address the problem of inter-band correlation and generate additional features that might be useful for further classification.

In total, 40 texture features, 29 spectral indices, and four band ratios were extracted. Analysis of these features' correlation matrices (Figures B1 and B2) showed that many of them were highly correlated. This may be explained by the similar calculation methods used to generate these measures as it agrees with Hall-Beyer (2016). Therefore, the high correlation measures with an absolute correlation value higher than 0.9 were excluded.

Only four out of all extracted spectral indices and band ratios (NDBI, MNDWI, Ratio 1, and Ratio 2) were left for the final classification. NDBI was left for further analysis as it demonstrated the potential to differential *pebble/cobble* from other classes (Figure 5.12 a). Good separability potential for *sand* and *platform* classes also was shown by the box-and-whisker plots of Ratio 1 and 2 (Figure 5.12 a and d). The MNDWI product was left for further steps due to its ability to discriminate water features from other classes, as shown in Figure 5.12 d.

The texture is considered one of the most valuable characteristics used to extract meaningful information for different purposes (Haralick et al., 1973). In this research, GLCM texture characteristics were found more useful than spectral indices for shoreline type discrimination, as the overall accuracy obtained from scenario 3 (82.25%) was higher than the one from scenario 4 (81.9%).

Most of the extracted GLCM texture features were highly correlated. This was expected because of the similarity of calculation of these measures. Some studies claim that correlation is usually expected to be high between entropy and the angular second moment, dissimilarity and

contrast, homogeneity and contrast, and homogeneity and dissimilarity (Hall-Beyer, 2016). However, the correlation cannot be predicted as it also depends on the features' characteristics in a particular area. In this study, while a high correlation between dissimilarity and contrast was found in each band, no correlation was observed between entropy and the angular second moment, homogeneity and contrast, and homogeneity and dissimilarity, which disagrees with Hall-Beyer (2016). Since it is impossible to predict which texture measures are highly correlated, it was decided to extract all ten measures for four VNIR bands; then, remove highly correlated measures based on the correlation matrix and consider the analysis of box-and-whisker plots. In this study, a high correlation was generally found between:

- Homogeneity, energy, GLCM maximum values, and variance;
- Mean, correlation, and variance; and
- Contrast and dissimilarity (Appendix B).

31 out of 40 measures were excluded after correlation matrix and box-and-whisker analysis, as demonstrated in Table 5.4. The box-and-whisker plots of the remaining measures are represented in Figure C.25 - Figure C.30. These measures were left for further analysis as they demonstrated the potential for discrimination between various classes. For example:

- *Bedrock high cliff* and *platform* have different pixel distribution in B2 entropy measure;
- *Bedrock platform* and *ramp* have the potential to be differentiated using B2 entropy and B2 variance;
- Good separability of *sand* from other non-vegetated classes may be observed in B2 energy and B2 entropy; and

- B3 contrast and B3 dissimilarity demonstrated the potential to differentiate between *road* and *pebble coble*.

However, not all of these measures were included in the final classification. It was found that the classification OA was improved (from 84.2% in scenario 5 to 85.6% in scenario 8) when B3 contrast, B3 dissimilarity, and B4 angular second moment were not used. As a result, only six texture features, including B2 contrast, B2 energy, B2 variance, B2 entropy, B4 correlation, and B3 contrast (Table 5.4), were left in the final classification.

The extraction of PCA components solved the inter-band correlation problem (Appendix B); however, similarly to the visible bands, principal components did not provide a strong separability between non-vegetated classes, as shown in Figure 5.14. The trial and error approach was implemented to decide what components should remain for the final classification. It was observed that the classification results were slightly improved from 85.50% when all the principal components were used to 85.97% when the principal components 8-10 products were removed.

6.3 Classification

Various classification scenarios (Table 5.5) were tested to find the best combination of input variables producing the highest classification results. In general, the use of additional inputs, including spectral indices, texture measures, and principal components, improves the resulting classification accuracy and is in agreement with other previous studies (Coburn & Roberts, 2004; Dash et al., 2007; Lu et al., 2008; Jolliffe & Cadima, 2016; Yengoh et al., 2016; Lever et al., 2017).

Several studies proved the enhancement of land cover classification by incorporating a DEM and its derivatives (Ricchetti, 2000; Geerling et al., 2007; Sluiter & Pebesma, 2010; Hoshikawa & Umezaki, 2014). Moreover, elevation and slope information are considered highly

important for coastal mapping (Demers et al., 2015). Therefore, a DEM and slope data were used in all classification scenarios in this research.

The lowest overall accuracy was obtained in scenario 1 when only Sentinel-2 spectral bands were used. The incorporation of additional features allowed for the improvement of results from 77.4% (scenario 1) to 87.1% (scenario 10). This difference was found to be statistically significant, as demonstrated in Table 5.17.

It was found that texture characteristics are more useful for shoreline type discrimination in comparison with spectral indices. This was found by comparing the results from scenarios 4 and 3, where spectral indices and texture measures were used, respectively. These results agree with the other studies that demonstrated the effectiveness of using textures in optical imagery (Coburn & Roberts, 2004; Dell'Acqua & Gamba, 2006; Lu et al., 2008; Singh et al., 2014)

HH and HV variables were found to be of high importance. The incorporation of SAR data with texture measures resulted in increased results from 81.90% (scenario 3) to 84.20% (scenario 10.4). In comparison, the combination of SAR data and spectral indices led to improved results from 81.25% (Scenario 4) to 84.71% (Scenario 6) (Table 5.11). These results agree with the ones obtained by Banks et al. (2014a), who found that the use of a combination of both SAR and optical data resulted in better scores.

Although the results of scenarios 6 and 5 demonstrate the superiority of using combined data (SAR with spectral indices and SAR with texture measures, respectively, along with PCs and DEM data), the use of all the measures together, including spectral indices, texture, SAR data, principal components, and DEM data, in scenario 7 leads to the lower overall accuracy of 83.54% (Table 5.12) than the ones obtained from scenario 6 and 5 (84.71% and 84.20%, respectively). The

reason for this may be an insufficient number of input variables overfitting the model. Therefore, a further feature selection step was performed using the trial and error method.

The results of scenarios 8 and 9 demonstrated the superiority of using HH data over that of HV. Thus, the overall accuracies were 85.60% (Table 5.13) and 84.34% (Table 5.14) when incorporating the HH and HV data, respectively. This agrees with other studies that suggested HH is the best single-polarization for discriminating soil and rock types (P. Dong & Leblon, 2004; Holah et al., 2005).

Scenario 10 achieved the highest overall accuracy score of 87.10%. The following input layers were used: PC1-PC7, NDVI, MNDWI, Ratio 1, Ratio 2, B2 CON, B2 E, B2 VAR, B2 ENT, B3 ASM, B4 COR, and $\overset{\circ}{\sigma}_{HH}$. This result is comparable with the other satellite-based shoreline classification studies (Demers et al., 2013; Banks et al., 2014a; Demers et al., 2015). *Bedrock platform* and *cliff* achieved comparable low PA and UA. These bedrock classes were misclassified, which can be explained by the similar spectral response of these classes. Also, as was discussed earlier, the shoreline in the study area is very narrow. Thus, it was often impossible to collect the training samples with an appropriate width, especially for the *bedrock cliff* class. Therefore, the spectral mixing of pixels could occur and cause a large portion of errors.

The overall accuracy of the final shoreline classification map was less than the one obtained for the final coastal land classification map. There may be several reasons for this. First, the water class used in coastal land classification obtained a high PA and UA as this class has different spectral and backscatter characteristics from all the land classes used in the study. That is why having a water class leads to the higher overall accuracy of the resulted coastal land map compared to one of the shoreline maps. Also, the final polyline consisted of segments with a length of 50 m. Therefore, one segment of the shoreline could correspond to several coastal land polygons. To

assign a particular class to a segment, the data of the closest classified polygon were used. Therefore, the shoreline classification map results are generally coarser than those of the coastal land classification map, and this affected the final overall accuracy results.

7. Conclusions

This research presents the first efforts to implement a shoreline classification using Sentinel satellites for oil spill response in Newfoundland. The high potential of using freely available Sentinel-1 and Sentinel-2 satellite data for coastal land and shoreline classifications was demonstrated. As a result of the implementation of the object-based approach, high accuracies of 87.10% and 84.75% were achieved.

A significant gap was found in the literature in assessing the potential of optical data for shoreline classification. Most of the research focused on assessing the potential of using SAR data, while no research investigating various parameters extracted from optical data was found. This study addressed the existing gap in the literature. One hundred and four features were extracted from Sentinel-2 data and analyzed using box-and-whisker plots, correlation matrices, and a classification accuracy assessment. A comparative assessment of the various classification models with different combinations of input variables was conducted. The optimal classification model includes the following input variables: PC1-PC7, spectral indices (NDVI, MNDWI, normalized difference between B4 and B8a, and the normalized difference between B8a and B2), GLCM texture measures (contrast, energy, variance, the entropy of red; the angular second moment of green; and correlation of blue bands), terrain features (DEM and slope), and SAR imagery (σ°_{HH}). However, some confusion occurred between the classes. The lowest producer's accuracy was obtained by the *man-made* class, which was misclassified with *bedrock cliff*, *pebble/cobble*, and *sand* due to similar spectral characteristics and the spatial resolution of satellite data. In contrast, *water* and vegetated classes were classified with the highest accuracies.

The optimal amount of shoreline types that can be discriminated by using Sentinel-1 and -2 images were found. Seven types were identified for coastal land classification, and five classes

were used to create the final shoreline classification map. The effect of incorporating multi-features and multi-source data was investigated. It was found that the use of both principal components, spectral indices, GLCM texture measures, and SAR data improved the resulting accuracy.

The major limitation of the study is the shoreline width relative to image resolution, which hinders the discrimination of classes. For example, it was often impossible to collect training samples with an appropriate width, especially for the *bedrock cliff* class. As a result, the spectral mixing of pixels occurred, which caused a high misclassification between *bedrock cliff* and *platform* classes.

8. Future Work

The developed algorithm demonstrated promising results for automated shoreline classification. Further work should focus on implementing the developed method for shoreline classification in other areas across the Canadian coastline.

This study incorporated optical and SAR data for shoreline classification. However, it was primarily focused on the extraction and analysis of Sentinel-2 features. Therefore, future work needs to explore the potential of predictor variables extracted from Sentinel-2. It is recommended to investigate the effect of incorporating polarimetric decomposition and backscatter band ratio features along with the most important predictor variables identified in this study.

One of the major limitations of this work is shoreline width relative to image resolution. Future work should address this challenge by implementing fusion techniques on Sentinel-2 images in order to obtain an image with higher resolution.

In this study, the enhanced Lee adaptive filter was used to suppress the effect of speckle noise in SAR imagery. It was selected due to its ability to preserve edges, linear features, and texture information. However, the effect of the Lee filter was not compared to other filters. Moreover, the size of the filter's window was set to 5 x 5, which correspond to the area of 2500 m^2 on the ground. Considering the nature of coastal zones, which are generally narrow, especially for cliffs, a smaller window size could be beneficial and maintain the boundaries between various land cover types better. The effect of using different windows sizes and filtering techniques might be investigated in further work as well.

Finally, one of the challenges during the field collection phase was the inability to access shorelines due to their remoteness and safety reasons. Due to these difficulties, not all of the sites could be visited. Instead, the classes at some locations were manually interpreted from Google Earth imagery and aerial photography. However, it was not always possible to distinguish between the different shoreline types due to the image resolution. Therefore, collecting more field samples in the future will be beneficial and will lead to more accurate results.

References

Alcantara, C., Kuemmerle, T., Prishchepov, A. V., & Radeloff, V. C. (2012). Mapping abandoned agriculture with multi-temporal MODIS satellite data. *Remote Sensing of Environment*, *124*, 334–347. https://doi.org/10.1016/j.rse.2012.05.019

Alesheikh, A. A., Ghorbanali, A., & Nouri, N. (2007). Coastline change detection using remote sensing. *International Journal of Environmental Science and Technology*, *4*(1), 61–66. Scopus. https://doi.org/10.1007/BF03325962

Ali, M. Z., Qazi, W., & Aslam, N. (2018). A comparative study of ALOS-2 PALSAR and Landsat-8 imagery for land cover classification using maximum likelihood classifier. *The Egyptian Journal of Remote Sensing and Space Science*, *21*, S29–S35. https://doi.org/10.1016/j.ejrs.2018.03.003

Al-Khudhairy, D. H. A., Caravaggi, I., & Giada, S. (2005). Structural Damage Assessments from Ikonos Data Using Change Detection, Object-Oriented Segmentation, and Classification Techniques. *Photogrammetric Engineering & Remote Sensing*, *71*(7), 825–837. https://doi.org/10.14358/PERS.71.7.825

Anderson, M. G., Judd, C., & Marcoe, K. (2012). Rapid Characterization of Shorelines Using a Georeferenced Video Mapping System. *Journal of Coastal Research*, *28*(5), 1289–1296. https://doi.org/10.2112/JCOASTRES-D-10-00186.1

Baatz, M., & Schäpe, A. (2000). *Multiresolution Segmentation: An optimization approach for high-quality multi-scale image segmentation*.

Banks, S., King, D., Merzouki, A., & Duffe, J. (2014a). Assessing RADARSAT-2 for Mapping Shoreline Cleanup and Assessment Technique (SCAT) Classes in the Canadian Arctic. *Canadian Journal of Remote Sensing*, *40*(3), 243.

Banks, S., King, D., Merzouki, A., & Duffe, J. (2014b). Characterizing Scattering Behaviour and Assessing Potential for Classification of Arctic Shore and Near-Shore Land Covers with Fine Quad-Pol RADARSAT-2 Data. *Canadian Journal of Remote Sensing*, *40*(4), 291–314. https://doi.org/10.1080/07038992.2014.979487

Banks, S., Millard, K., Pasher, J., Richardson, M., Wang, H., & Duffe, J. (2015). Assessing the Potential to Operationalize Shoreline Sensitivity Mapping: Classifying Multiple Wide Fine Quadrature Polarized RADARSAT-2 and Landsat 5 Scenes with a Single Random Forest Model. *Remote Sensing*, *7*(10), 13528–13563. https://doi.org/10.3390/rs71013528

Baztan, J., Chouinard, O., Jorgensen, B., Tett, P., Vanderlinden, J.-P., & Vasseur, L. (2015). Introduction. In J. Baztan, O. Chouinard, B. Jorgensen, P. Tett, J.-P. Vanderlinden, & L. Vasseur (Eds.), *Coastal Zones* (pp. xxi–xxiii). Elsevier. https://doi.org/10.1016/B978-0-12-802748-6.02001-5

Beijma, S., Comber, A., & Lamb, A. (2014). Random forest classification of salt marsh vegetation habitats using quad-polarimetric airborne SAR, elevation and optical RS data. *Remote Sensing of Environment*, *149*, 118–129. https://doi.org/10.1016/j.rse.2014.04.010

Belgiu, M., & Csillik, O. (2018). Sentinel-2 cropland mapping using pixel-based and object-based time-weighted dynamic time warping analysis. *Remote Sensing of Environment*, *204*, 509–523. https://doi.org/10.1016/j.rse.2017.10.005

Belgiu, M., & Drăguţ, L. (2016). Random forest in remote sensing: A review of applications and future directions. *ISPRS Journal of Photogrammetry and Remote Sensing*, *114*, 24–31. https://doi.org/10.1016/j.isprsjprs.2016.01.011

Benz, U. C., Hofmann, P., Willhauck, G., Lingenfelder, I., & Heynen, M. (2004). Multi-resolution, object-oriented fuzzy analysis of remote sensing data for GIS-ready information. *ISPRS*

Journal of Photogrammetry and Remote Sensing, *58*(3–4), 239–258. https://doi.org/10.1016/j.isprsjprs.2003.10.002

Berberoğlu, S., Akin, A., Atkinson, P. M., & Curran, P. J. (2010). Utilizing image texture to detect land-cover change in Mediterranean coastal wetlands. *International Journal of Remote Sensing*, *31*(11), 2793–2815. https://doi.org/10.1080/01431160903111077

Berry, H. D., Harper, J. R., Mumford, T. F., Bookheim, B. E., Sewell, A. T., & Tamayo, L. J. (2001). *The Washington State ShoreZone Inventory User's Manual*. Nearshore Habitat Program Washington State Department of Natural Resources.

Blackburn, G. A. (1998). Spectral indices for estimating photosynthetic pigment concentrations: A test using senescent tree leaves. *International Journal of Remote Sensing*, *19*(4), 657–675. https://doi.org/10.1080/014311698215919

Blaschke, T. (2010). Object-based image analysis for remote sensing. *ISPRS Journal of Photogrammetry and Remote Sensing*, *65*(1), 2–16. https://doi.org/10.1016/j.isprsjprs.2009.06.004

Blaschke, T., Hay, G. J., Kelly, M., Lang, S., Hofmann, P., Addink, E., Queiroz Feitosa, R., van der Meer, F., van der Werff, H., van Coillie, F., & Tiede, D. (2014). Geographic Object-Based Image Analysis – Towards a new paradigm. *ISPRS Journal of Photogrammetry and Remote Sensing*, *87*, 180–191. https://doi.org/10.1016/j.isprsjprs.2013.09.014

Boegh, E., Soegaard, H., Broge, N., Hasager, C. B., Jensen, N. O., Schelde, K., & Thomsen, A. (2002). Airborne multispectral data for quantifying leaf area index, nitrogen concentration, and photosynthetic efficiency in agriculture. *Remote Sensing of Environment*, *81*(2), 179–193. https://doi.org/10.1016/S0034-4257(01)00342-X

Bouzekri, S., Lasbet, A. A., & Lachehab, A. (2015). A New Spectral Index for Extraction of Built-Up Area Using Landsat-8 Data. *Journal of the Indian Society of Remote Sensing*, *43*(4), 867–873. https://doi.org/10.1007/s12524-015-0460-6

Brebbia, C. A. (Ed.). (2008). *Environmental problems in coastal regions VII*. WIT Press.

Breiman, L. (2001a). Random Forests. *Machine Learning*, *45*(1), 5–32. https://doi.org/10.1023/A:1010933404324

Breiman, L. (2001b). Random Forests. *Machine Learning*, *45*(1), 5–32. https://doi.org/10.1023/A:1010933404324

Breiman, L., Friedman, J., Olshen, R., & Stone, C. (1984). Classification And Regression Trees. In *Classification and Regression Trees* (p. 358). https://doi.org/10.1201/9781315139470

Brodu, N. (2017). Super-resolving multiresolution images with band-independant geometry of multispectral pixels. *IEEE Transactions on Geoscience and Remote Sensing*, 1–8. https://doi.org/10.1109/TGRS.2017.2694881

Burella, G., Moro, L., & Neis, B. (2021). Is on-board noise putting fish harvesters' hearing at risk? A study of noise exposures in small-scale fisheries in Newfoundland and Labrador. *Safety Science*, *140*, 105325. https://doi.org/10.1016/j.ssci.2021.105325

Byron, R., & Doyle, A. (2003). *Retrenchment and Regeneration in Rural Newfoundland*. University of Toronto Press. https://doi.org/10.3138/9781442679320

Cable, J. W., Kovacs, J. M., Shang, J., & Jiao, X. (2014). Multi-Temporal Polarimetric RADARSAT-2 for Land Cover Monitoring in Northeastern Ontario, Canada. *Remote Sensing*, *6*(3), 2372–2392. http://dx.doi.org/10.3390/rs6032372

Campbell, J. B., & Wynne, R. H. (2011). *Introduction to Remote Sensing, Fifth Edition*. Guilford Press.

Camps-Valls, G., Tuia, D., Gómez-Chova, L., Jiménez, S., & Malo, J. (2011). Remote Sensing Image Processing. *Synthesis Lectures on Image, Video, and Multimedia Processing*, *5*(1), 1–192. https://doi.org/10.2200/S00392ED1V01Y201107IVM012

Canada, E. and C. C. (2020, April 27). *International Convention on Oil Pollution Preparedness, Response, and Cooperation*. Aem. https://www.canada.ca/en/environment-climate-change/corporate/international-affairs/partnerships-organizations/convention-oil-pollution-preparedness-response-cooperation.html

Canters, F. (1997). *Evaluating the Uncertainty of Area Estimates Derived from Fuzzy Land-Cover Classification*. 12.

Castillejo-González, I. L., López-Granados, F., García-Ferrer, A., Peña-Barragán, J. M., Jurado-Expósito, M., de la Orden, M. S., & González-Audicana, M. (2009). Object- and pixel-based analysis for mapping crops and their agro-environmental associated measures using QuickBird imagery. *Computers and Electronics in Agriculture*, *68*(2), 207–215. https://doi.org/10.1016/j.compag.2009.06.004

Catto, N. (2011). *Coastal Erosion in Newfoundland*. Department of Geography, Memorial University \. http://nlhfrp.ca/wp-content/uploads/2015/01/Coastal-Erosion-in-Newfoundland.pdf

Catto, N., & Etheridge, B. (2006). Sensitivity, Exposure, And Vulnerability Of Gravel Beaches To Petroleum Pollution, Avalon Peninsula, Newfoundland, Canada. *WIT Transactions on Ecology and the Environment*, *88*. http://dx.doi.org.qe2a-proxy.mun.ca/10.2495/CENV060221

Chatziantoniou, A., Psomiadis, E., & Petropoulos, G. P. (2017). Co-Orbital Sentinel 1 and 2 for LULC Mapping with Emphasis on Wetlands in a Mediterranean Setting Based on Machine Learning. *Remote Sensing*, *9*(12), 1259. https://doi.org/10.3390/rs9121259

Chen, S.-Y., Lin, W.-C., & Chen, C.-T. (1991). Split-and-merge image segmentation based on localized feature analysis and statistical tests. *CVGIP: Graphical Models and Image Processing*, *53*(5), 457–475. https://doi.org/10.1016/1049-9652(91)90030-N

Chen, Y., He, X., Wang, J., & Xiao, R. (2014). The Influence of Polarimetric Parameters and an Object-Based Approach on Land Cover Classification in Coastal Wetlands. *Remote Sensing*, *6*(12), 12575–12592. http://dx.doi.org/10.3390/rs61212575

Chen, Y., Shi, P., Fung, T., Wang, J., & Li, X. (2007). Object-oriented classification for urban land cover mapping with ASTER imagery. *International Journal of Remote Sensing*, *28*(20), 4645–4651. https://doi.org/10.1080/01431160500444731

Chen, Z., Pasher, J., Duffe, J., & Behnamian, A. (2017). Mapping Arctic coastal ecosystems with high-resolution optical satellite imagery using a hybrid classification approach. *Canadian Journal of Remote Sensing*, *43*(6), 1–15. https://doi.org/10.1080/07038992.2017.1370367

Chuvieco, E., Cocero, D., Riaño, D., Martin, P., Martínez-Vega, J., de la Riva, J., & Pérez, F. (2004). Combining NDVI and surface temperature for the estimation of live fuel moisture content in forest fire danger rating. *Remote Sensing of Environment*, *92*(3), 322–331. https://doi.org/10.1016/j.rse.2004.01.019

Clevers, J. G. P. W., & Gitelson, A. (2012). Using the red-edge bands on Sentinel-2 for retrieving canopy chlorophyll and nitrogen content. *European Space Agency, (Special Publication) ESA SP*, *707*.

Clevers, J. G. P. W., & Verhoef, W. (1993). LAI estimation by means of the WDVI: A sensitivity analysis with a combined PROSPECT-SAIL model. *Remote Sensing Reviews*, *7*(1), 43–64. https://doi.org/10.1080/02757259309532165

C-NLOPB. (2020, February 6). *Spill Frequency and Volume Annual Summary*. Https://Www.Cnlopb.ca/Information/Statistics/. https://www.cnlopb.ca/wp-content/uploads/spill/sumtab.pdf

Coburn, C. A., & Roberts, A. C. B. (2004). A multiscale texture analysis procedure for improved forest stand classification. *International Journal of Remote Sensing*, *25*(20), 4287–4308. https://doi.org/10.1080/0143116042000192367

Corcoran, J. M., Knight, J. F., & Gallant, A. L. (2013). Influence of Multi-Source and Multi-Temporal Remotely Sensed and Ancillary Data on the Accuracy of Random Forest Classification of Wetlands in Northern Minnesota. *Remote Sensing*, *5*(7), 3212–3238. http://dx.doi.org/10.3390/rs5073212

Crippen, R. E. (1990). Calculating the vegetation index faster. *Remote Sensing of Environment*, *34*(1), 71–73. https://doi.org/10.1016/0034-4257(90)90085-Z

Crossland, C. J., Kremer, H. H., Lindeboom, H., Crossland, J. I. M., & Tissier, M. D. A. L. (2005). *Coastal Fluxes in the Anthropocene: The Land-Ocean Interactions in the Coastal Zone Project of the International Geosphere-Biosphere Programme*. Springer Science & Business Media.

Crósta, A. P., & Moore, J. M. (1988). *Enhancement of Landsat Thematic Mapper imagery for residual soil mapping in SW Minais Gerais State, Brazil: A prospecting case history in Greenstone belt terrain*. ResearchGate. https://www.researchgate.net/publication/284966233_Enhancement_of_Landsat_Themati

c_Mapper_imagery_for_residual_soil_mapping_in_SW_Minais_Gerais_State_Brazil_A_prospecting_case_history_in_Greenstone_belt_terrain

Darack, E. (2006, October). Avalon Peninsula, Canada. *Weatherwise*, *59*(5), 14–15.

Dash, J., Mathur, A., Foody, G. M., Curran, P. J., Chipman, J. W., & Lillesand, T. M. (2007). Land cover classification using multi-temporal MERIS vegetation indices. *International Journal of Remote Sensing*, *28*(6), 1137–1159. https://doi.org/10.1080/01431160600784259

Daughtry, C. S. T., Walthall, C. L., Kim, M. S., de Colstoun, E. B., & McMurtrey, J. E. (2000). Estimating Corn Leaf Chlorophyll Concentration from Leaf and Canopy Reflectance. *Remote Sensing of Environment*, *74*(2), 229–239. https://doi.org/10.1016/S0034-4257(00)00113-9

de Leeuw, J., Jia, H., Yang, L., Liu, X., Schmidt, K., & Skidmore, A. K. (2006). Comparing accuracy assessments to infer superiority of image classification methods. *International Journal of Remote Sensing*, *27*(1), 223–232. https://doi.org/10.1080/01431160500275762

Dell'Acqua, F., & Gamba, P. (2006). Discriminating urban environments using multiscale texture and multiple SAR images. *International Journal of Remote Sensing*, *27*(18), 3797–3812. https://doi.org/10.1080/01431160600557572

Dell'Acqua, F., & Gamba, P. (2012). Remote Sensing and Earthquake Damage Assessment: Experiences, Limits, and Perspectives. *Proceedings of the IEEE*, *100*(10), 2876–2890. https://doi.org/10.1109/JPROC.2012.2196404

Demers, A.-M., Banks, S., Duffe, J., Carriere, M., Torontow, V., Chaudhary, B., & Laforest, S. (2013). *eSPACE: Emergency spatial pre-SCAT for Arctic Coastal Ecosystem*. 1–6. https://doi.org/10.1109/RADAR.2013.6586151

Demers, A.-M., Banks, S. N., Pasher, J., Duffe, J., & Laforest, S. (2015). A Comparative Analysis of Object-Based and Pixel-Based Classification of RADARSAT-2 C–Band and Optical Satellite Data for Mapping Shoreline Types in the Canadian Arctic. *Canadian Journal of Remote Sensing*, *41*(1), 1–19. https://doi.org/10.1080/07038992.2015.1020361

Dinç, İ., Sigdel, M., Dinç, S., Sigdel, M. S., Pusey, M. L., & Aygün, R. S. (2014). Evaluation of Normalization and PCA on the Performance of Classifiers for Protein Crystallization Images. *Proceedings of IEEE Southeastcon / IEEE Southeastcon. IEEE Southeastcon, 2014*. https://www.ncbi.nlm.nih.gov/pmc/articles/PMC4409005/

Dong, P., & Leblon, B. (2004). Rock unit discrimination on Landsat TM, SIR-C and Radarsat images using spectral and textural information. *International Journal of Remote Sensing*, *25*(18), 3745–3768. https://doi.org/10.1080/01431160310001632675

Dong, T., Liu, J., Qian, B., He, L., Liu, J., Wang, R., Jing, Q., Champagne, C., McNairn, H., Powers, J., Shi, Y., Chen, J. M., & Shang, J. (2020). Estimating crop biomass using leaf area index derived from Landsat 8 and Sentinel-2 data. *ISPRS Journal of Photogrammetry and Remote Sensing*, *168*, 236–250. https://doi.org/10.1016/j.isprsjprs.2020.08.003

Duda, R. O., Hart, P. E., & Stork, D. G. (2012). *Pattern Classification*. John Wiley & Sons.

Dwivedi, R. S. (2017). *Remote Sensing of Soils*. Springer.

ECCC. (2016). *A Field Guide to Oil Spill Response on Marine Shorelines*. Environment and Climate Change Canada, Polaris Applied Sciences., and S3 Environmental Inc.

ECCC. (2018). *Shoreline Cleanup Assessment Technique (SCAT) manual*. Environment and Climate Change Canada, Third edition, prepared and provided by Triox Environmental Emergencies, Owens Coastal Consultants, Environmental Mapping Ltd.

https://buyandsell.gc.ca/cds/public/2019/01/17/11bcca72f6b0cb7b6a4b4aaf8684334d/scat_manual.pdf

Eichkitz, C., Groot, P., & Brouwer, F. (2013). *Visualizing Anisotropy in Seismic Facies Using Stratigraphically Constrained, Multi-Directional Texture Attribute Analysis*. ResearchGate. https://www.researchgate.net/publication/269333145_Visualizing_Anisotropy_in_Seismic_Facies_Using_Stratigraphically_Constrained_Multi-Directional_Texture_Attribute_Analysis

Eisak, C., Smith, M., & Hillier, J. (2014). Assessment of multiresolution segmentation for delimiting drumlins in digital elevation models. *Geomorphology (Amst), 214 (100):452-464*. https://doi.org/10.1016/j.geomorph.2014.02.028

ESA. (n.d.). *Sentinel-2—Missions—Sentinel Online—Sentinel*. Retrieved March 4, 2021, from https://sentinel.esa.int/web/sentinel/missions/sentinel-2

ESA. (2015). *Radiometric calibration of S-1 Level-1 products generated by the S-1 IPF*. file:///C:/Users/scco-stu11/Downloads/S1-Radiometric-Calibration-V1.0.pdf

Escadafal, R. (1989). Remote sensing of arid soil surface color with Landsat thematic mapper. *Advances in Space Research*, *9*(1), 159–163. https://doi.org/10.1016/0273-1177(89)90481-X

Fawagreh, K., Gaber, M. M., & Elyan, E. (2014). Random forests: From early developments to recent advancements. *Systems Science & Control Engineering*, *2*(1), 602–609. https://doi.org/10.1080/21642583.2014.956265

Feng, Q., Yang, J., Zhu, D., Liu, J., Guo, H., Bayartungalag, B., & Li, B. (2019). Integrating Multitemporal Sentinel-1/2 Data for Coastal Land Cover Classification Using a

Multibranch Convolutional Neural Network: A Case of the Yellow River Delta. *Remote Sensing*, *11*(9). http://dx.doi.org/10.3390/rs11091006

Filipponi, F. (2019). Sentinel-1 GRD Preprocessing Workflow. *Proceedings*, *18*(1), 11. https://doi.org/10.3390/ECRS-3-06201

Fingas, M. F. (2014). *Handbook of Oil Spill Science and Technology*. John Wiley & Sons, Incorporated. http://ebookcentral.proquest.com/lib/mun/detail.action?docID=1895871

Fisheries and Oceans Canada, G. of C. (2021). *2020 Tide Tables*. https://tides.gc.ca/eng/data/predictions/2020

Foody, G. M., & Mathur, A. (2004). A relative evaluation of multiclass image classification by support vector machines. *IEEE Transactions on Geoscience and Remote Sensing*, *42*(6), 1335–1343. https://doi.org/10.1109/TGRS.2004.827257

Frampton, W. J., Dash, J., Watmough, G., & Milton, E. J. (2013). Evaluating the capabilities of Sentinel-2 for quantitative estimation of biophysical variables in vegetation. *ISPRS Journal of Photogrammetry and Remote Sensing*, *82*, 83–92. https://doi.org/10.1016/j.isprsjprs.2013.04.007

Franklin, S. E., Skeries, E. M., Stefanuk, M. A., & Ahmed, O. S. (2018). Wetland classification using Radarsat-2 SAR quad-polarization and Landsat-8 OLI spectral response data: A case study in the Hudson Bay Lowlands Ecoregion. *International Journal of Remote Sensing*, *39*(6), 1615–1627. https://doi.org/10.1080/01431161.2017.1410295

Frantzen, M., Falk-Petersen, I.-B., Nahrgang, J., Smith, T. J., Olsen, G. H., Hangstad, T. A., & Camus, L. (2012). Toxicity of crude oil and pyrene to the embryos of beach spawning capelin (Mallotus villosus). *Aquatic Toxicology*, *108*, 42–52. https://doi.org/10.1016/j.aquatox.2011.09.022

French-McCay, D., Crowley, D., Rowe, J. J., Bock, M., Robinson, H., Wenning, R., Walker, A. H., Joeckel, J., Nedwed, T. J., & Parkerton, T. F. (2018). Comparative Risk Assessment of spill response options for a deepwater oil well blowout: Part 1. Oil spill modeling. *Marine Pollution Bulletin*, *133*, 1001–1015. https://doi.org/10.1016/j.marpolbul.2018.05.042

Gabr, S. S., Hassan, S. M., & Sadek, M. F. (2015). Prospecting for new gold-bearing alteration zones at El-Hoteib area, South Eastern Desert, Egypt, using remote sensing data analysis. *ResearchGate*, *71*. https://www.researchgate.net/publication/276129712_Prospecting_for_new_gold-bearing_alteration_zones_at_El-Hoteib_area_South_Eastern_Desert_Egypt_using_remote_sensing_data_analysis

Gallant, A. L. (2015). The Challenges of Remote Monitoring of Wetlands. *Remote Sensing*, *7*(8), 10938–10950. http://dx.doi.org/10.3390/rs70810938

Gamon, J. A., Field, C. B., Roberts, D. A., Ustin, S. L., & Valentini, R. (1993). Functional patterns in an annual grassland during an AVIRIS overflight. *Remote Sensing of Environment*, *44*(2), 239–253. https://doi.org/10.1016/0034-4257(93)90019-T

Geerling, G. W., Labrador-Garcia, M., Clevers, J. G. P. W., Ragas, A. M. J., & Smits, A. J. M. (2007). Classification of floodplain vegetation by data fusion of spectral (CASI) and LiDAR data. *International Journal of Remote Sensing*, *28*(19), 4263–4284. https://doi.org/10.1080/01431160701241720

Georganos, S., Grippa, T., Vanhuysse, S., Lennert, M., Shimoni, M., & Wolff, E. (2018). Very High Resolution Object-Based Land Use–Land Cover Urban Classification Using Extreme Gradient Boosting. *IEEE Geoscience and Remote Sensing Letters*, *15*(4), 607–611. https://doi.org/10.1109/LGRS.2018.2803259

Gholizadeh, A., Žižala, D., Saberioon, M., & Borůvka, L. (2018). Soil organic carbon and texture retrieving and mapping using proximal, airborne and Sentinel-2 spectral imaging. *Remote Sensing of Environment*, *218*, 89–103. https://doi.org/10.1016/j.rse.2018.09.015

Gislason, P. O., Benediktsson, J. A., & Sveinsson, J. R. (2006). Random Forests for land cover classification. *Pattern Recognition Letters*, *27*(4), 294–300. https://doi.org/10.1016/j.patrec.2005.08.011

Gitelson, A. A., Kaufman, Y. J., & Merzlyak, M. N. (1996). Use of a green channel in remote sensing of global vegetation from EOS-MODIS. *Remote Sensing of Environment*, *58*(3), 289–298. https://doi.org/10.1016/S0034-4257(96)00072-7

Giustarini, L., Hostache, R., Matgen, P., Schumann, G. J.-, Bates, P. D., & Mason, D. C. (2013). A Change Detection Approach to Flood Mapping in Urban Areas Using TerraSAR-X. *IEEE Transactions on Geoscience and Remote Sensing*, *51*(4), 2417–2430. https://doi.org/10.1109/TGRS.2012.2210901

Gonzalez, R. C., & Woods, R. E. (1992). *Digital Image Procassing*.

Göttsche, F.-M., & Olesen, F. (2002). *MULTI-SCALE SEGMENTATION OF SATELLITE DATA INTO IMAGE OBJECTS AND KNOWLEDGE-BASED DETECTION AND CLASSIFICATION OF CLOUDS*.

Government of Canada. (n.d.). *Geospatial Data Extraction*. Retrieved July 16, 2020, from https://maps.canada.ca/czs/index-en.html

Government of Canada, S. C. (2012, February 8). *Statistics Canada: 2011 Census Profile*. https://www12.statcan.gc.ca/census-recensement/2011/dp-pd/prof/details/page.cfm?Lang=E&Geo1=ER&Code1=1010&Geo2=PR&Code2=10&Da

ta=Count&SearchText=avalon%20peninsula&SearchType=Begins&SearchPR=01&B1=All&Custom=&TABID=1

Government of Newfoundland and Labrador. (n.d.). *Fisheries, Forestry and Agriculture, Surveys and Mapping Services*. Fisheries, Forestry and Agriculture. Retrieved August 7, 2021, from https://www.gov.nl.ca/ffa/lands/maps/

Guan, H., Li, J., Chapman, M., Deng, F., Ji, Z., & Yang, X. (2013). Integration of orthoimagery and lidar data for object-based urban thematic mapping using random forests. *International Journal of Remote Sensing*, *34*(14), 5166–5186. https://doi.org/10.1080/01431161.2013.788261

Guo, M., Li, J., Sheng, C., Xu, J., & Wu, L. (2017). A Review of Wetland Remote Sensing. *Sensors; Basel*, *17*(4), 777. http://dx.doi.org/10.3390/s17040777

Habib, A., Shin, S. W., Kim, K., Kim, C., Bang, K.-I., Kim, E.-M., & Lee, D.-C. (2007). Comprehensive Analysis of Sensor Modeling Alternatives for High Resolution Imaging Satellites. *Photogrammetric Engineering & Remote Sensing*, *73*(11), 1241–1251. https://doi.org/10.14358/PERS.73.11.1241

Haboudane, D., Miller, J. R., Pattey, E., Zarco-Tejada, P. J., & Strachan, I. B. (2004). Hyperspectral vegetation indices and novel algorithms for predicting green LAI of crop canopies: Modeling and validation in the context of precision agriculture. *Remote Sensing of Environment*, *90*(3), 337–352. https://doi.org/10.1016/j.rse.2003.12.013

Hajj, M. E., Baghdadi, N., Zribi, M., & Bazzi, H. (2017). Synergic Use of Sentinel-1 and Sentinel-2 Images for Operational Soil Moisture Mapping at High Spatial Resolution over Agricultural Areas. *Remote Sensing*, *9*(12), 1292. http://dx.doi.org/10.3390/rs9121292

Hall-Beyer, M. (2007). *GLCM Texture: A Tutorial v. 1.0 through 2.7*. https://doi.org/10.11575/PRISM/33280

Hall-Beyer, M. (2016). *Practical guidelines for choosing GLCM textures to use in landscape classification tasks over a range of moderate spatial scales*. ResearchGate. https://www.researchgate.net/publication/313234046_Practical_guidelines_for_choosing_GLCM_textures_to_use_in_landscape_classification_tasks_over_a_range_of_moderate_spatial_scales

Hansen, M. C., Potapov, P. V., Moore, R., Hancher, M., Turubanova, S. A., Tyukavina, A., Thau, D., Stehman, S. V., Goetz, S. J., Loveland, T. R., Kommareddy, A., Egorov, A., Chini, L., Justice, C. O., & Townshend, J. R. G. (2013). High-Resolution Global Maps of 21st-Century Forest Cover Change. *Science*, *342*(6160), 850–853.

Hansen, M. C., Stehman, S. V., Potapov, P. V., Loveland, T. R., Townshend, J. R. G., DeFries, R. S., Pittman, K. W., Arunarwati, B., Stolle, F., Steininger, M. K., Carroll, M., & DiMiceli, C. (2008). Humid Tropical Forest Clearing from 2000 to 2005 Quantified by Using Multitemporal and Multiresolution Remotely Sensed Data. *Proceedings of the National Academy of Sciences of the United States of America*, *105*(27), 9439–9444.

Hao, P., Zhan, Y., Wang, L., Niu, Z., & Shakir, M. (2015). Feature Selection of Time Series MODIS Data for Early Crop Classification Using Random Forest: A Case Study in Kansas, USA. *Remote Sensing*, *7*(5), 5347–5369. https://doi.org/10.3390/rs70505347

Haralick, R. M., Shanmugam, K., & Dinstein, I. (1973). Textural Features for Image Classification. *IEEE Transactions on Systems, Man, and Cybernetics*, *SMC-3*(6), 610–621. https://doi.org/10.1109/TSMC.1973.4309314

Hay, G. J., & Castilla, G. (n.d.). *Geographic Object-Based Image Analysis (GEOBIA): A new name for a new discipline* (pp. 75–89). Springer Berlin Heidelberg. https://doi.org/10.1007/978-3-540-77058-9_4

Hedley, J. D., Roelfsema, C., Brando, V., Giardino, C., Kutser, T., Phinn, S., Mumby, P. J., Barrilero, O., Laporte, J., & Koetz, B. (2018). Coral reef applications of Sentinel-2: Coverage, characteristics, bathymetry and benthic mapping with comparison to Landsat 8. *Remote Sensing of Environment*, *216*, 598–614. https://doi.org/10.1016/j.rse.2018.07.014

Heiden, U., Roessner, S., Segl, K., & Kaufmann, H. (2001). Analysis of spectral signatures of urban surfaces for their identification using hyperspectral HyMap data. *IEEE/ISPRS Joint Workshop on Remote Sensing and Data Fusion over Urban Areas (Cat. No.01EX482)*, 173–177. https://doi.org/10.1109/DFUA.2001.985871

Herold, M., Liu, X., & Clarke, K. C. (2003). Spatial Metrics and Image Texture for Mapping Urban Land Use. *Photogrammetric Engineering and Remote Sensing*, *69*(9), 991–1001. https://doi.org/10.14358/pers.69.9.991

Herold, M., Roberts, D. A., Gardner, M. E., & Dennison, P. E. (2004). Spectrometry for urban area remote sensing—Development and analysis of a spectral library from 350 to 2400 nm. *Remote Sensing of Environment*, *91*(3), 304–319. https://doi.org/10.1016/j.rse.2004.02.013

Holah, N., Baghdadi, N., Zribi, M., Bruand, A., & King, C. (2005). Potential of ASAR/ENVISAT for the characterization of soil surface parameters over bare agricultural fields. *Remote Sensing of Environment*, *96*(1), 78–86. https://doi.org/10.1016/j.rse.2005.01.008

Hoshikawa, K., & Umezaki, M. (2014). Effects of terrain-induced shade removal using global DEM data sets on land-cover classification. *International Journal of Remote Sensing*, *35*(4), 1331–1355. https://doi.org/10.1080/01431161.2013.876122

Howens, D., Harper, J., & Owens, E. H. (1994). *Physical Shore-Zone Mapping System for British Columbia*. https://www2.gov.bc.ca/assets/gov/data/geographic/topography/bc_shorezonemappingsystem.pdf

Huang, H., Gong, P., Clinton, N., & Hui, F. (2008). Reduction of atmospheric and topographic effect on Landsat TM data for forest classification. *International Journal of Remote Sensing*, *29*(19), 5623–5642. https://doi.org/10.1080/01431160802082148

Huete, A., Didan, K., Miura, T., Rodriguez, E. P., Gao, X., & Ferreira, L. G. (2002). Overview of the radiometric and biophysical performance of the MODIS vegetation indices. *Remote Sensing of Environment*, *83*(1), 195–213. https://doi.org/10.1016/S0034-4257(02)00096-2

Huete, A. R. (1988). A soil-adjusted vegetation index (SAVI). *Remote Sensing of Environment*, *25*(3), 295–309. https://doi.org/10.1016/0034-4257(88)90106-X

Hussain, M., Chen, D., Cheng, A., Wei, H., & Stanley, D. (2013). Change detection from remotely sensed images: From pixel-based to object-based approaches. *ISPRS Journal of Photogrammetry and Remote Sensing*, *80*, 91–106. https://doi.org/10.1016/j.isprsjprs.2013.03.006

Immitzer, M., Vuolo, F., & Atzberger, C. (2016). First Experience with Sentinel-2 Data for Crop and Tree Species Classifications in Central Europe. *Remote Sensing*, *8*(3), 166. http://dx.doi.org/10.3390/rs8030166

Iwahashi, J., Kamiya, I., Matsuoka, M., & Yamazaki, D. (2018). Global terrain classification using 280 m DEMs: Segmentation, clustering, and reclassification. *Prog Earth Planet Sci*, *5*(1). https://doi.org/10.1186/s40645-017-0157-2

Iwahashi, J., & Pike, R. J. (2007). Automated classifications of topography from DEMs by an unsupervised nested-means algorithm and a three-part geometric signature. In *Geomorphology* (Vol. 86, Issues 3–4, p. 32). https://doi.org/10.1016/j.geomorph.2006.09.012

Jackson, J. B. C., Cubit, J. D., Keller, B. D., Batista, V., Burns, K., Caffey, H. M., Caldwell, R. L., Garrity, S. D., Getter, C. D., Gonzalez, C., Guzman, H. M., Kaufmann, K. W., Knap, A. H., Levings, S. C., Marshall, M. J., Steger, R., Thompson, R. C., & Weil, E. (1989). Ecological Effects of a Major Oil Spill on Panamanian Coastal Marine Communities. *Science*, *243*(4887), 37–44.

Jensen, J. R. (2016). *Introductory Digital Image Processing. A remote Sensing Perspective.* (4th ed.). PEARSON.

Jenssen, B. M. (1994). Review article: Effects of oil pollution, chemically treated oil, and cleaning on thermal balance of birds. *Environmental Pollution*, *86*(2), 207–215. https://doi.org/10.1016/0269-7491(94)90192-9

Jia, M., Wang, Z., Mao, D., Ren, C., Wang, C., & Wang, Y. (2021). Rapid, robust, and automated mapping of tidal flats in China using time series Sentinel-2 images and Google Earth Engine. *Remote Sensing of Environment*, *255*, 112285. https://doi.org/10.1016/j.rse.2021.112285

Jiang, Z., Huete, A. R., Chen, J., Chen, Y., Li, J., Yan, G., & Zhang, X. (2006). Analysis of NDVI and scaled difference vegetation index retrievals of vegetation fraction. *Remote Sensing of Environment*, *101*(3), 366–378. https://doi.org/10.1016/j.rse.2006.01.003

Jiang, Z., Huete, A. R., Didan, K., & Miura, T. (2008). Development of a two-band enhanced vegetation index without a blue band. *Remote Sensing of Environment*, *112*(10), 3833–3845. https://doi.org/10.1016/j.rse.2008.06.006

Jiao, L., Sun, W., Yang, G., Ren, G., & Liu, Y. (2019). A Hierarchical Classification Framework of Satellite Multispectral/Hyperspectral Images for Mapping Coastal Wetlands. *Remote Sensing*, *11*(19), 2238. https://doi.org/10.3390/rs11192238

Jin, Y.-Q. (2013). *Polarimetric scattering and SAR information retrieval*. John Wiley & Sons Singapore PteLtd.

Joensuu, M., Pilditch, C. A., Harris, R., Hietanen, S., Pettersson, H., & Norkko, A. (2018). Sediment properties, biota, and local habitat structure explain variation in the erodibility of coastal sediments. *Limnology and Oceanography*, *63*(1), 173–186. https://doi.org/10.1002/lno.10622

Jolliffe, I. T., & Cadima, J. (2016). Principal component analysis: A review and recent developments. *Philosophical Transactions of the Royal Society A: Mathematical, Physical and Engineering Sciences*, *374*(2065), 20150202. https://doi.org/10.1098/rsta.2015.0202

Kaplan, G., & Avdan, U. (2017). Object-based water body extraction model using Sentinel-2 satellite imagery. *European Journal of Remote Sensing*, *50*(1), 137–143. https://doi.org/10.1080/22797254.2017.1297540

Karnieli, A., Kaufman, Y. J., Remer, L., & Wald, A. (2001). AFRI — aerosol free vegetation index. *Remote Sensing of Environment*, *77*(1), 10–21. https://doi.org/10.1016/S0034-4257(01)00190-0

Kavzoglu, T., & Reis, S. (2008). Performance Analysis of Maximum Likelihood and Artificial Neural Network Classifiers for Training Sets with Mixed Pixels. *GIScience & Remote Sensing*, *45*(3), 330–342. https://doi.org/10.2747/1548-1603.45.3.330

Kayitakire, F., Hamel, C., & Defourny, P. (2006). Retrieving forest structure variables based on image texture analysis and IKONOS-2 imagery. *Remote Sensing of Environment*, *102*(3–4), 390–401. https://doi.org/10.1016/j.rse.2006.02.022

Khan, R. A., & Payne, J. F. (2005). Influence of a crude oil dispersant, corexit 9527, and dispersed oil on capelin (Mallotus villosus), Atlantic cod (Gadus morhua), longhorn sculpin (Myoxocephalus octodecemspinosus), and cunner (Tautogolabrus adspersus). *Bulletin of Environmental Contamination and Toxicology*, *75*(1), 50–56. Scopus. https://doi.org/10.1007/s00128-005-0717-9

Khorram, S., Nelson, S. A. C., Koch, F. H., & van der Wiele, C. F. (2012). *Remote Sensing*. Springer US. https://doi.org/10.1007/978-1-4614-3103-9

Klemas, V. (2013). Remote Sensing of Coastal Wetland Biomass: An Overview. *Journal of Coastal Research*, *29*(5), 1016–1028. http://dx.doi.org/10.2112/JCOASTRES-D-12-00237.1

Kopecka, M., Szatmari, D., & Rosina, K. (2017). Analysis of Urban Green Spaces Based on Sentinel-2A: Case Studies from Slovakia†. *Land*, *6*(2), 25. http://dx.doi.org/10.3390/land6020025

Korhonen, L., Hadi, Packalen, P., & Rautiainen, M. (2017). Comparison of Sentinel-2 and Landsat 8 in the estimation of boreal forest canopy cover and leaf area index. *Remote Sensing of Environment*, *195*, 259–274. https://doi.org/10.1016/j.rse.2017.03.021

Kumar, P., Prasad, R., Choudhary, A., Mishra, V. N., Gupta, D. K., & Srivastava, P. K. (2017). A statistical significance of differences in classification accuracy of crop types using different classification algorithms. *Geocarto International*, *32*(2), 206–224. https://doi.org/10.1080/10106049.2015.1132483

Laba, M., Downs, R., Smith, S., Welsh, S., Neider, C., White, S., Richmond, M., Philpot, W., & Baveye, P. (2008). Mapping invasive wetland plants in the Hudson River National Estuarine Research Reserve using quickbird satellite imagery. *Remote Sensing of Environment*, *112*(1), 286–300. https://doi.org/10.1016/j.rse.2007.05.003

Lacaux, J. P., Tourre, Y. M., Vignolles, C., Ndione, J. A., & Lafaye, M. (2007). Classification of ponds from high-spatial resolution remote sensing: Application to Rift Valley Fever epidemics in Senegal. *Remote Sensing of Environment*, *106*(1), 66–74. https://doi.org/10.1016/j.rse.2006.07.012

Lamarche, A., Sergy, G. A., & Owens, E. H. (2007). Shoreline cleanup and assessment technique (SCAT) data management manual. *Edmonton, Canada: Emergencies Science and Technology Division, Science and Technology Branch, Environment Canada*. http://www.shorelinescat.com/Documents/Manuals/Environment%20Canada%202007%20SCAT%20Data%20Management%20Manual.pdf

Lane, C. R., Liu, H., Autrey, B. C., Anenkhonov, O. A., Chepinoga, V. V., & Wu, Q. (2014). Improved Wetland Classification Using Eight-Band High Resolution Satellite Imagery and a Hybrid Approach. *Remote Sensing*, *6*(12), 12187–12216. https://doi.org/10.3390/rs61212187

Lawal, O., & Oyegun, C. U. (2017). Geographic information systems-based expert system modelling for shoreline sensitivity to oil spill disaster in Rivers State, Nigeria. *Jàmbá : Journal of Disaster Risk Studies*, *9*(1). https://doi.org/10.4102/jamba.v9i1.429

Lebourgeois, V., Dupuy, S., Vintrou, É., Ameline, M., Butler, S., & Bégué, A. (2017). A Combined Random Forest and OBIA Classification Scheme for Mapping Smallholder Agriculture at Different Nomenclature Levels Using Multisource Data (Simulated Sentinel-2 Time Series, VHRS and DEM). *Remote Sensing*, *9*(3), 259. https://doi.org/10.3390/rs9030259

Lee, J., Jurkevich, L., Dewaele, P., Wambacq, P., & Oosterlinck, A. (1994). Speckle filtering of synthetic aperture radar images: A Review. *Remote Sensing Reviews*, *8*. https://doi.org/10.1080/02757259409532206

Lee, J.-S. (1981). Speckle analysis and smoothing of synthetic aperture radar images. *Computer Graphics and Image Processing*, *17*(1), 24–32. https://doi.org/10.1016/S0146-664X(81)80005-6

Lee, J.-S., Grunes, M. R., & Grandi, G. de. (1999). Polarimetric SAR speckle filtering and its implication for classification. *IEEE Transactions on Geoscience and Remote Sensing*, *37*(5), 2363–2373. https://doi.org/10.1109/36.789635

Lefebvre, A., Sannier, C., & Corpetti, T. (2016). Monitoring Urban Areas with Sentinel-2A Data: Application to the Update of the Copernicus High Resolution Layer Imperviousness Degree. *Remote Sensing*, *8*(7), 606. https://doi.org/10.3390/rs8070606

Leigh, S., Wang, Z., & Clausi, D. A. (2014). Automated Ice–Water Classification Using Dual Polarization SAR Satellite Imagery. *IEEE Transactions on Geoscience and Remote Sensing*, *52*(9), 5529–5539. https://doi.org/10.1109/TGRS.2013.2290231

Lever, J., Krzywinski, M., & Altman, N. (2017). Principal component analysis. *Nature Methods*, *14*(7), 641–642. https://doi.org/10.1038/nmeth.4346

Li, M., Ma, L., Blaschke, T., Cheng, L., & Tiede, D. (2016). A systematic comparison of different object-based classification techniques using high spatial resolution imagery in agricultural environments. *International Journal of Applied Earth Observation and Geoinformation*, *49*, 87–98. https://doi.org/10.1016/j.jag.2016.01.011

Lillesand, T. M., & Kiefer, R. W. (2000). *Remote sensing and image interpretation* (4th ed.). John Wiley & Sons, Incorporated.

Liu, D., & Xia, F. (2010). Assessing object-based classification: Advantages and limitations. *Remote Sensing Letters*, *1*(4), 187–194. https://doi.org/10.1080/01431161003743173

Lu, D., Batistella, M., Moran, E., & de Miranda, E. E. (2008). A Comparative Study of Landsat TM and SPOT HRG Images for Vegetation Classification in the Brazilian Amazon. *Photogrammetric Engineering & Remote Sensing*, *74*(3), 311–321. https://doi.org/10.14358/PERS.74.3.311

Lu, D., & Weng, Q. (2007). A survey of image classification methods and techniques for improving classification performance. *International Journal of Remote Sensing*, *28*(5), 823–870. https://doi.org/10.1080/01431160600746456

Ma, L., Li, M., Ma, X., Cheng, L., Du, P., & Liu, Y. (2017). A review of supervised object-based land-cover image classification. *ISPRS Journal of Photogrammetry and Remote Sensing*, *130*, 277–293. https://doi.org/10.1016/j.isprsjprs.2017.06.001

Mahdianpari, M., Salehi, B., Mohammadimanesh, F., Homayouni, S., & Gill, E. (2019). The first wetland inventory map of newfoundland at a spatial resolution of 10 m using sentinel-1

and sentinel-2 data on the Google Earth Engine cloud computing platform. *Remote Sensing (Basel, Switzerland)*, *11*(1), 43-. https://doi.org/10.3390/rs11010043

Main, R., Cho, M. A., Mathieu, R., O'Kennedy, M. M., Ramoelo, A., & Koch, S. (2011). An investigation into robust spectral indices for leaf chlorophyll estimation. *ISPRS Journal of Photogrammetry and Remote Sensing*, *66*(6), 751–761. https://doi.org/10.1016/j.isprsjprs.2011.08.001

Major, D. J., Baret, F., & Guyot, G. (1990). A ratio vegetation index adjusted for soil brightness. *International Journal of Remote Sensing*, *11*(5), 727–740. https://doi.org/10.1080/01431169008955053

Marceau, D. J., Howarth, P. J., Dubois, J. M., & Gratton, D. J. (1990). Evaluation Of The Grey-level Co-occurrence Matrix Method For Land-cover Classification Using Spot Imagery. *IEEE Transactions on Geoscience and Remote Sensing*, *28*(4), 513–519. https://doi.org/10.1109/tgrs.1990.572937

Mardia, K. V., & Hainsworth, T. J. (1988). A spatial thresholding method for image segmentation. *IEEE Transactions on Pattern Analysis and Machine Intelligence*, *10*(6), 919–927. https://doi.org/10.1109/34.9113

Martín Alonso, J. M., Ortega Piris, A., & Pérez Labajos, C. (2015). Illegal discharges in Spanish waters. Analysis of the profile of the Alleged Offending Vessel. *Marine Pollution Bulletin*, *97*(1), 255–261. https://doi.org/10.1016/j.marpolbul.2015.06.009

Marzano, F. S., Iacobelli, M., Orlandi, M., & Cimini, D. (2021). Coastal Water Remote Sensing From Sentinel-2 Satellite Data Using Physical, Statistical, and Neural Network Retrieval Approach. *IEEE Transactions on Geoscience and Remote Sensing*, *59*(2), 915–928. https://doi.org/10.1109/TGRS.2020.2980941

McFeeters, S. K. (1996). The use of the Normalized Difference Water Index (NDWI) in the delineation of open water features. *International Journal of Remote Sensing, London, England*, *17*(7), 1425–1432.

McInerney, D. O., & Nieuwenhuis, M. (2009). A comparative analysis of kNN and decision tree methods for the Irish National Forest Inventory. *International Journal of Remote Sensing*, *30*(19), 4937–4955. https://doi.org/10.1080/01431160903022936

McNemar, Q. (1947). Note on the sampling error of the difference between correlated proportions or percentages. *Psychometrika*, *12*(2), 153–157. https://doi.org/10.1007/BF02295996

Michel, J., Christopherson, S., & Whipple, F. (1995). Mechanical protection guidelines. *International Oil Spill Conference Proceedings*, *1995*(1), 841–842. https://doi.org/10.7901/2169-3358-1995-1-841

Michel, J., Owens, E. H., Zengel, S., Graham, A., Nixon, Z., Allard, T., Holton, W., Reimer, P. D., Lamarche, A., White, M., Rutherford, N., Childs, C., Mauseth, G., Challenger, G., & Taylor, E. (2013). Extent and Degree of Shoreline Oiling: Deepwater Horizon Oil Spill, Gulf of Mexico, USA. *PloS One*, *8*(6), e65087-. https://doi.org/10.1371/journal.pone.0065087

Miliaresis, G., & Kokkas, N. (2007). Segmentation and object-based classification for the extraction of the building class from LIDAR DEMs. *Computers & Geosciences*, *33*(8), 1076–1087. https://doi.org/10.1016/j.cageo.2006.11.012

Millard, K., & Richardson, M. (2013). Wetland mapping with LiDAR derivatives, SAR polarimetric decompositions, and LiDAR–SAR fusion using a random forest classifier. *Canadian Journal of Remote Sensing*, *39*(4), 290–307. https://doi.org/10.5589/m13-038

Mitchell, H. B. (2010). Multi-resolution Analysis. In H. B. Mitchell (Ed.), *Image Fusion: Theories, Techniques and Applications* (pp. 93–106). Springer. https://doi.org/10.1007/978-3-642-11216-4_8

Moigne, J. L., & Tilton, J. C. (1995). Refining image segmentation by integration of edge and region data. *IEEE Transactions on Geoscience and Remote Sensing*, *33*(3), 605–615. https://doi.org/10.1109/36.387576

Motohka, T., Nasahara, K. N., Oguma, H., & Tsuchida, S. (2010). Applicability of Green-Red Vegetation Index for Remote Sensing of Vegetation Phenology. *Remote Sensing*, *2*(10), 2369–2387. https://doi.org/10.3390/rs2102369

Mountrakis, G., Im, J., & Ogole, C. (2011). Support vector machines in remote sensing: A review. *ISPRS Journal of Photogrammetry and Remote Sensing*, *66*(3), 247–259. https://doi.org/10.1016/j.isprsjprs.2010.11.001

Murray, G., Neis, B., & Schneider, D. C. (2007). Lessons from a Multi-Scale Historical Reconstruction of Newfoundland and Labrador Fisheries. *Coastal Management*, *36*(1), 81–108. https://doi.org/10.1080/08920750701682056

Myint, S. W., Gober, P., Brazel, A., Grossman-Clarke, S., & Weng, Q. (2011). Per-pixel vs. Object-based classification of urban land cover extraction using high spatial resolution imagery. *Remote Sensing of Environment*, *115*(5), 1145–1161. https://doi.org/10.1016/j.rse.2010.12.017

Myneni, R. B., Yang, W., Nemani, R. R., Huete, A. R., Dickinson, R. E., Knyazikhin, Y., Didan, K., Fu, R., Juárez, R. I. N., Saatchi, S. S., Hashimoto, H., Ichii, K., Shabanov, N. V., Tan, B., Ratana, P., Privette, J. L., Morisette, J. T., Vermote, E. F., Roy, D. P., … Salomonson,

V. V. (2007). Large Seasonal Swings in Leaf Area of Amazon Rainforests. *Proceedings of the National Academy of Sciences of the United States of America*, *104*(12), 4820–4823.

Nagendra, H. (2001). Review article. Using remote sensing to assess biodiversity. *International Journal of Remote Sensing*, *22*, 2377–2400. https://doi.org/10.1080/01431160117096

Nagendra, H., & Gadgil, M. (1999). Biodiversity Assessment at Multiple Scales: Linking Remotely Sensed Data with Field Information. *Proceedings of the National Academy of Sciences of the United States of America*, *96*(16), 9154–9158.

Narbonne, G. M., & Gehling, J. G. (2003). Life after snowball: The oldest complex Ediacaran fossils. *Geology*, *31*(1), 27–30. https://doi.org/10.1130/0091-7613(2003)031<0027:LASTOC>2.0.CO;2

National Geographic. (2010, October 20). *Coastal Destinations Rated*. Travel. https://www.nationalgeographic.com/travel/coastal-destinations-rated/top-rated/

Natural Resources Canada. (2016, July 6). *Natural Resources Canada*. Natural Resources Canada. https://www.nrcan.gc.ca/home

NCC. (2020). *Coasting along Canada's habitats.* Nature Conservancy Canada. https://www.natureconservancy.ca/en/blog/coasting-along-canadas.html

Neff, J. M., Owens, E. H., Stoker, S. W., & McCormick, D. M. (1995). Shoreline Oiling Conditions in Prince William Sound Following the Exxon Valdez Oil Spill. *Exxon Valdez Oil Spill: Fate and Effects in Alaskan Waters*. https://doi.org/10.1520/STP19869S

Nitze, I., Schulthess, U., & Asche, H. (2012). *Comparison of machine learning algorithms random forest, artificial neural network and support vector machine to maximum likelihood for supervised crop type classification.* GEOBIA 2012.

Nivedita Priyadarshini, K., Kumar, M., Rahaman, S. A., & Nitheshnirmal, S. (2018). A comparative study of advanced land use/land cover classification algorithms using sentinel-2 data. *ISPRS - International Archives of the Photogrammetry, Remote Sensing and Spatial Information Sciences*, *XLII–5*, 665–670. https://doi.org/10.5194/isprs-archives-XLII-5-665-2018

NOAA. (2013). *Shoreline Assessment Manual*. U.S. Dept. of Commerce, Emergency Response Division, Office of Response and Restoration, National Oceanic and Atmospheric Administration. https://response.restoration.noaa.gov/sites/default/files/manual_shore_assess_aug2013.pdf

Novelli, A., Aguilar, M. A., Nemmaoui, A., Aguilar, F. J., & Tarantino, E. (2016). Performance evaluation of object based greenhouse detection from Sentinel-2 MSI and Landsat 8 OLI data: A case study from Almería (Spain). *International Journal of Applied Earth Observation and Geoinformation*, *52*, 403–411. https://doi.org/10.1016/j.jag.2016.07.011

Ouyang, Z., Becker, R., Shaver, W., & Chen, J. (2014). Evaluating the sensitivity of wetlands to climate change with remote sensing techniques. *Hydrological Processes*, *28*(4), 1703–1712. https://doi.org/10.1002/hyp.9685

Owens, E. H., & Sergy, G. A. (2004). *The Arctic SCAT Manual: A Field Guide to the Documentation of Oiled Shorelines in Arctic Environments.* Environment Canada, Edmonton, AB, Canada. http://www.environmentalunit.com/Documentation/06%20Shoreline%20Assessment%20SCAT/Env%20Canada%20Arctic%20SCAT.pdf

Pal, M. (2005). Random forest classifier for remote sensing classification. *International Journal of Remote Sensing*, *26*(1), 217–222. https://doi.org/10.1080/01431160412331269698

Pan, S., Guan, H., Yu, Y., Li, J., & Peng, D. (2019). A Comparative Land-Cover Classification Feature Study of Learning Algorithms: DBM, PCA, and RF Using Multispectral LiDAR Data. *IEEE Journal of Selected Topics in Applied Earth Observations and Remote Sensing*, *12*(4), 1314–1326. https://doi.org/10.1109/JSTARS.2019.2899033

Pearson, R. L., & Miller, L. D. (1972). *Remote Mapping of Standing Crop Biomass for Estimation of the Productivity of the Shortgrass Prairie*. 1355.

Pelletier, C., Valero, S., Inglada, J., Champion, N., & Dedieu, G. (2016). Assessing the robustness of Random Forests to map land cover with high resolution satellite image time series over large areas. *Remote Sensing of Environment*, *187*, 156–168. https://doi.org/10.1016/j.rse.2016.10.010

Peña-Barragán, J. M., Ngugi, M. K., Plant, R. E., & Six, J. (2011). Object-based crop identification using multiple vegetation indices, textural features and crop phenology. *Remote Sensing of Environment*, *115*(6), 1301–1316. https://doi.org/10.1016/j.rse.2011.01.009

Percy, R. J., LeBlanc, S. R., & Owens, E. H. (1997). *An integrated approach to shoreline mapping for spill response planning in Canada*. https://ioscproceedings.org/doi/abs/10.7901/2169-3358-1997-1-277

Persson, M., Lindberg, E., & Reese, H. (2018). Tree Species Classification with Multi-Temporal Sentinel-2 Data. *Remote Sensing; Basel*, *10*(11). http://dx.doi.org/10.3390/rs10111794

Pinty, B., & Verstraete, M. M. (1992). GEMI: A non-linear index to monitor global vegetation from satellites. *Vegetatio*, *101*(1), 15–20. https://doi.org/10.1007/BF00031911

Polikar, R. (2006). Ensemble based systems in decision making. *IEEE Circuits and Systems Magazine*, *6*(3), 21–45. https://doi.org/10.1109/MCAS.2006.1688199

Pouget, M., Madeira Netto, J., Le Floc'h, E., & Kamal, S. (1991). *Caractéristiques spectrales des surfaces sableuses de la région côtière Nord-Ouest de l'Egypte: Application aux données satellitaires SPOT* (pp. 27–38). https://www.documentation.ird.fr/hor/fdi:34605#

Presutti, M. E., Franklin, S. E., Moskal, L. M., & Dickson, E. E. (2001). Supervised classification of multisource satellite image spectral and texture data for agricultural crop mapping in Buenos Aires Province, Argentina. *Canadian Journal of Remote Sensing*, *27*(6), 679–684. https://doi.org/10.1080/07038992.2001.10854910

Pu, R., Landry, S., & Yu, Q. (2011). Object-based urban detailed land cover classification with high spatial resolution IKONOS imagery. *International Journal of Remote Sensing*, *32*(12), 3285–3308. https://doi.org/10.1080/01431161003745657

Purkis, S., Myint, S., & Riegl, B. (2006). Enhanced detection of the coral Acropora cervicornis from satellite imagery using a textural operator. *Remote Sensing of Environment*, *101*, 82–94. https://doi.org/10.1016/j.rse.2005.11.009

Qi, J., Chehbouni, A., Huete, A. R., Kerr, Y. H., & Sorooshian, S. (1994). A modified soil adjusted vegetation index. *Remote Sensing of Environment*, *48*(2), 119–126. https://doi.org/10.1016/0034-4257(94)90134-1

Qian, Y., Zhou, W., Yan, J., Li, W., & Han, L. (2015). Comparing Machine Learning Classifiers for Object-Based Land Cover Classification Using Very High Resolution Imagery. *Remote Sensing; Basel*, *7*(1), 153–168. http://dx.doi.org/10.3390/rs70100153

Qiu, C., Mou, L., Schmitt, M., & Zhu, X. X. (2020). Fusing Multiseasonal Sentinel-2 Imagery for Urban Land Cover Classification With Multibranch Residual Convolutional Neural

Networks. *IEEE Geoscience and Remote Sensing Letters*, *17*(10), 1787–1791. https://doi.org/10.1109/LGRS.2019.2953497

Qunming Wang, Blackburn, G. A., Onojeghuo, A. O., Dash, J., Lingquan Zhou, Yihang Zhang, & Atkinson, P. M. (2017). Fusion of Landsat 8 OLI and Sentinel-2 MSI Data. *IEEE Transactions on Geoscience and Remote Sensing*, *55*(7), 3885–3899. https://doi.org/10.1109/TGRS.2017.2683444

Rajendran, S., al-Khirbash, S., Pracejus, B., Nasir, S., Al-Abri, A. H., Kusky, T. M., & Ghulam, A. (2012). ASTER detection of chromite bearing mineralized zones in Semail Ophiolite Massifs of the northern Oman Mountains: Exploration strategy. *Ore Geology Reviews*, *44*, 121–135. https://doi.org/10.1016/j.oregeorev.2011.09.010

Ranson, K. J., Sun, G., Kharuk, V. I., & Kovacs, K. (2001). Characterization of Forests in Western Sayani Mountains, Siberia from SIR-C SAR Data. *Remote Sensing of Environment*, *75*(2), 188–200. https://doi.org/10.1016/S0034-4257(00)00166-8

Reese, H., Nyström, M., Nordkvist, K., & Olsson, H. (2014). Combining airborne laser scanning data and optical satellite data for classification of alpine vegetation. *International Journal of Applied Earth Observation and Geoinformation*, *27*, 81–90. https://doi.org/10.1016/j.jag.2013.05.003

Rejaur Rahman, Md., & Saha, S. K. (2008). Multi-resolution segmentation for object-based classification and accuracy assessment of land use/land cover classification using remotely sensed data. *Journal of the Indian Society of Remote Sensing*, *36*(2), 189–201. https://doi.org/10.1007/s12524-008-0020-4

Ricchetti, E. (2000). Multispectral Satellite Image and Ancillary Data Integration for Geological Classification. *Photogrammetric Engineering & Remote Sensing*, *66*(4). https://www.asprs.org/wp-content/uploads/pers/2000journal/april/2000_apr_429-435.pdf

Rodrigues, S. W. P., & Souza-Filho, P. W. M. (2011). Use of Multi-Sensor Data to Identify and Map Tropical Coastal Wetlands in the Amazon of Northern Brazil. *Wetlands*, *31*(1), 11–23. https://doi.org/10.1007/s13157-010-0135-6

Rondeaux, G., Steven, M., & Baret, F. (1996). Optimization of soil-adjusted vegetation indices. *Remote Sensing of Environment*, *55*(2), 95–107. https://doi.org/10.1016/0034-4257(95)00186-7

RRT. (2015). *Shoreline Segmentation Guidance for Shoreline Cleanup and Assessment Technique (SCAT) Section 9422*. https://rrt10nwac.com/Files/NWACP/2020/Section%209422%20v21.pdf

Saleem, A., & Awange, J. L. (2019). Coastline shift analysis in data deficient regions: Exploiting the high spatio-temporal resolution Sentinel-2 products. *CATENA*, *179*, 6–19. https://doi.org/10.1016/j.catena.2019.03.023

Santner, R., Cocklan-Vendl, M., Stong, B., Jacqueline, M., Owens, E. H., & Taylor, E. (2011). *The Deep Water Horizon MC252-Macondo Shoreline Cleanup Assessment Technique (SCAT) Program* (Manuscript No. 270). http://www.shorelinescat.com/Documents/Publications/06%202011%20Deepwater%20Horizon%20SCAT%20Program.pdf

Schowengerdt, R. A., & Schowengerdt, R. A. (2006). *Remote Sensing: Models and Methods for Image Processing*. Elsevier Science & Technology. http://ebookcentral.proquest.com/lib/mun/detail.action?docID=294338

Schultz, B., Immitzer, M., Formaggio, A. R., Sanches, I. D. A., Luiz, A. J. B., & Atzberger, C. (2015). Self-Guided Segmentation and Classification of Multi-Temporal Landsat 8 Images for Crop Type Mapping in Southeastern Brazil. *Remote Sensing; Basel*, *7*(11), 14482–14508. http://dx.doi.org/10.3390/rs71114482

Segarra, J., Buchaillot, M. L., Link to external site, this link will open in a new window, Araus, J. L., Link to external site, this link will open in a new window, & Kefauver, S. C. (2020). Remote Sensing for Precision Agriculture: Sentinel-2 Improved Features and Applications. *Agronomy; Basel*, *10*(5), 641. http://dx.doi.org/10.3390/agronomy10050641

Shao, Y., & Lunetta, R. S. (2012). Comparison of support vector machine, neural network, and CART algorithms for the land-cover classification using limited training data points. *ISPRS Journal of Photogrammetry and Remote Sensing*, *70*, 78–87. https://doi.org/10.1016/j.isprsjprs.2012.04.001

Simioni, J., Guasselli, L., Ruiz, L., Fernandez Nascimento, V., & Oliveira, G. (2018). Small inner marsh area delimitation using remote sensing spectral indexes and decision tree method in southern Brazil. *Revista de Teledetección*, 55. https://doi.org/10.4995/raet.2018.10366

Singh, M., Malhi, Y., & Bhagwat, S. (2014). Evaluating land use and aboveground biomass dynamics in an oil palm–dominated landscape in Borneo using optical remote sensing. *Journal of Applied Remote Sensing*, *8*(1), 083695. https://doi.org/10.1117/1.JRS.8.083695

Skidmore, A. K., Pettorelli, N., Coops, N. C., Geller, G. N., Hansen, M., Lucas, R., Mücher, C. A., O'Connor, B., Paganini, M., Pereira, H. M., Schaepman, M. E., Turner, W., Wang, T., & Wegmann, M. (2015). Environmental science: Agree on biodiversity metrics to track from space. *Nature*, *523*(7561), 403–405. https://doi.org/10.1038/523403a

Sluiter, R., & Pebesma, E. J. (2010). Comparing techniques for vegetation classification using multi- and hyperspectral images and ancillary environmental data. *International Journal of Remote Sensing*, *31*(23), 6143–6161. https://doi.org/10.1080/01431160903401379

Small, D. (2011). Flattening Gamma: Radiometric Terrain Correction for SAR Imagery. *IEEE Transactions on Geoscience and Remote Sensing*, *49*(8), 3081–3093. https://doi.org/10.1109/TGRS.2011.2120616

Small, D., Miranda, N., & Meier, E. (2009). *A Revised Radiometric Normalisation Standard for SAR*. *4*, 566–569. https://doi.org/10.1109/IGARSS.2009.5417439

Smith, A. M. S., Wooster, M. J., Powell, A. K., & Usher, D. (2010). Texture based feature extraction: Application to burn scar detection in Earth observation satellite sensor imagery. *International Journal of Remote Sensing*. https://doi.org/10.1080/01431160110106104

Song, C., Woodcock, C. E., Seto, K. C., Lenney, M. P., & Macomber, S. A. (2001). Classification and Change Detection Using Landsat TM Data: When and How to Correct Atmospheric Effects? *Remote Sensing of Environment*, *75*(2), 230–244. https://doi.org/10.1016/S0034-4257(00)00169-3

Song, X., Duan, Z., & Jiang, X. (2012). Comparison of artificial neural networks and support vector machine classifiers for land cover classification in Northern China using a SPOT-5 HRG image. *International Journal of Remote Sensing*, *33*(10), 3301–3320. https://doi.org/10.1080/01431161.2011.568531

Stepinski, T. F., & Bagaria, C. (2009). Segmentation-Based Unsupervised Terrain Classification for Generation of Physiographic Maps. *IEEE Geoscience and Remote Sensing Letters*. https://doi.org/10.1109/LGRS.2009.2024333

Steven E. Franklin. (2010). *Remote sensing for biodiversity and wildlife management: Synthesis and applications*. McGraw-Hill.

Su, L., & Gibeaut, J. (2017). Using UAS Hyperspatial RGB Imagery for Identifying Beach Zones along the South Texas Coast. *Remote Sensing*, *9*(2), 159. https://doi.org/10.3390/rs9020159

Syed, T. H., Famiglietti, J. S., Chambers, D. P., Willis, J. K., Hilburn, K., & Cazenave, A. (2010). Satellite-based global-ocean mass balance estimates of interannual variability and emerging trends in continental freshwater discharge. *Proceedings of the National Academy of Sciences of the United States of America*, *107*(42), 17916–17921.

Tairova, Z., Frantzen, M., Mosbech, A., Arukwe, A., & Gustavson, K. (2019). Effects of water accommodated fraction of physically and chemically dispersed heavy fuel oil on beach spawning capelin (Mallotus villosus). *Marine Environmental Research*, *147*, 62–71. https://doi.org/10.1016/j.marenvres.2019.03.010

Tavares, P. A., Link to external site, this link will open in a new window, Beltrão, N. E. S., Link to external site, this link will open in a new window, Guimarães, U. S., Link to external site, this link will open in a new window, Teodoro, A. C., & Link to external site, this link will open in a new window. (2019). Integration of Sentinel-1 and Sentinel-2 for Classification and LULC Mapping in the Urban Area of Belém, Eastern Brazilian Amazon. *Sensors (Basel, Switzerland)*, *19*(5). http://dx.doi.org/10.3390/s19051140

Thanh Noi, P., & Kappas, M. (2018). Comparison of Random Forest, k-Nearest Neighbor, and Support Vector Machine Classifiers for Land Cover Classification Using Sentinel-2 Imagery. *Sensors*, *18*(1), 18. https://doi.org/10.3390/s18010018

Thome, K., Palluconi, F., Takashima, T., & Masuda, K. (1998). Atmospheric correction of ASTER. *IEEE Transactions on Geoscience and Remote Sensing*, *36*(4), 1199–1211. https://doi.org/10.1109/36.701026

Tian, J., & Chen, D.-M. (2007). Optimization in multi-scale segmentation of high-resolution satellite images for artificial feature recognition. *International Journal of Remote Sensing*, *28*(20), 4625–4644. https://doi.org/10.1080/01431160701241746

Tøttrup, C. (2004). Improving tropical forest mapping using multi-date Landsat TM data and pre-classification smoothing. *International Journal of Remote Sensing - INT J REMOTE SENS*, *25*. https://doi.org/10.1080/01431160310001598926

Tucker, C. J. (1979). Red and photographic infrared linear combinations for monitoring vegetation. *Remote Sensing of Environment*, *8*(2), 127–150. https://doi.org/10.1016/0034-4257(79)90013-0

Tuominen, S., & Pekkarinen, A. (2005). Performance of different spectral and textural aerial photograph features in multi-source forest inventory. *Remote Sensing of Environment*, *94*(2), 256–268. https://doi.org/10.1016/j.rse.2004.10.001

Turner, M. (2010). *Review of Offshore Oil-spill Prevention and Remediation Requirements and Practices in Newfoundland and Labrador*. Department of Natural Resources, Government of Newfoundland and Labrador. https://www.gov.nl.ca/nr/files/publications-energy-nloffshore-oil-review-appendix-package.pdf

US EPA, O. (2019, April 10). *What is an oil spill contingency plan?* [Overviews and Factsheets]. US EPA. https://www.epa.gov/oil-spills-prevention-and-preparedness-regulations/what-oil-spill-contingency-plan

Van Tricht, K., Gobin, A., Gilliams, S., & Piccard, I. (2018). Synergistic Use of Radar Sentinel-1 and Optical Sentinel-2 Imagery for Crop Mapping: A Case Study for Belgium. *Remote Sensing*, *10*(10), 1642. https://doi.org/10.3390/rs10101642

Vapnik, V. N. (2000). *The nature of statistical learning theory* (2nd ed..). Springer.

Wang, K., Lepparanta, M., Gastgifvars, M., Vainio, J., & Wang, C. (2008). The drift and spreading of the Runner 4 oil spill and the ice conditions in the Gulf of Finland, winter 2006. *Estonian Journal of Earth Sciences*, *57*(3), 181–191. https://doi.org/10.3176/earth.2008.3.06

Wang, L., & Qu, J. J. (2007). NMDI: A normalized multi-band drought index for monitoring soil and vegetation moisture with satellite remote sensing. *Geophysical Research Letters*, *34*(20). https://doi.org/10.1029/2007GL031021

Wang, M., Fei, X., Zhang, Y., Chen, Z., Wang, X., Tsou, J. Y., Liu, D., & Lu, X. (2018). Assessing Texture Features to Classify Coastal Wetland Vegetation from High Spatial Resolution Imagery Using Completed Local Binary Patterns (CLBP). *Remote Sensing*, *10*(5), 778. http://dx.doi.org/10.3390/rs10050778

Wang, Y. (2010). *Remote sensing of coastal environments*. CRC Press/Taylor & Francis.

WECP. (n.d.). *St. John's, Canada*. World Energy Cities Partnership. Retrieved April 27, 2021, from https://energycities.org/member-cities/st-johns-canada

Wenxia Wei, Xiuwan Chen, & Ainai Ma. (2005). *Object-oriented information extraction and application in high-resolution remote sensing image*. *6*, 3803–3806. https://doi.org/10.1109/IGARSS.2005.1525737

Whiteside, T., Boggs, G., & Maier, S. (2011). Comparing object-based and pixel-based classifications for mapping savannas. *International Journal Of Applied Earth Observation And Geoinformation*, *13*(6), 884–893. https://doi.org/10.1016/j.jag.2011.06.008

Wiens, J. A. (2013). *Oil in the Environment: Legacies and Lessons of the Exxon Valdez Oil Spill*. Cambridge University Press.

Woestyne, I., Jordan, M., Moons, T., & Cord, M. (2004). *A software system for efficient DEM segmentation and DTM estimation in complex urban areas*.

Woodhouse, I. H. (2017). *Introduction to Microwave Remote Sensing*. CRC Press.

Wynja, V., Demers, A.-M., Laforest, S., Lacelle, M., Pasher, J., Duffe, J., Chaudhary, B., Wang, H., & Giles, T. (2014). Mapping coastal information across Canada's northern regions based on low-altitude helicopter videography in support of environmental emergency preparedness efforts. *Journal of Coastal Research*, *31*(2), 276–290. https://doi.org/10.2112/JCOASTRES-D-14-00059.1

Xu, H. (2006). Modification of normalised difference water index (NDWI) to enhance open water features in remotely sensed imagery. *International Journal of Remote Sensing*, *27*(14), 3025–3033. https://doi.org/10.1080/01431160600589179

Yagüe-Martínez, N., Prats-Iraola, P., González, F. R., Brcic, R., Shau, R., Geudtner, D., Eineder, M., & Bamler, R. (2016). Interferometric Processing of Sentinel-1 TOPS Data. *IEEE Transactions on Geoscience and Remote Sensing*, *54*(4), 2220–2234. https://doi.org/10.1109/TGRS.2015.2497902

Yan, G., Mas, J.-F., Maathuis, B. H. P., Xiangmin, Z., & Dijk, P. M. V. (2006). Comparison of pixel-based and object-oriented image classification approaches—A case study in a coal fire area, Wuda, Inner Mongolia, China. *International Journal of Remote Sensing*, *27*(18), 4039–4055. https://doi.org/10.1080/01431160600702632

Yang, J., Gong, P., Fu, R., Zhang, M., Chen, J., Liang, S., Xu, B., Shi, J., & Dickinson, R. (2013). The role of satellite remote sensing in climate change studies. *Nature Climate Change*, *3*(10), 875–883. http://dx.doi.org/10.1038/nclimate1908

Yang, X., Zhao, S., Qin, X., Zhao, N., & Liang, L. (2017). Mapping of Urban Surface Water Bodies from Sentinel-2 MSI Imagery at 10 m Resolution via NDWI-Based Image Sharpening. *Remote Sensing*, *9*(6), 596. https://doi.org/10.3390/rs9060596

Yengoh, G. T., Dent, D., Olsson, L., Tengberg, A. E., & Tucker, C. J. (2016). Applications of NDVI for Land Degradation Assessment. In G. T. Yengoh, D. Dent, L. Olsson, A. E. Tengberg, & C. J. Tucker III (Eds.), *Use of the Normalized Difference Vegetation Index (NDVI) to Assess Land Degradation at Multiple Scales: Current Status, Future Trends, and Practical Considerations* (pp. 17–25). Springer International Publishing. https://doi.org/10.1007/978-3-319-24112-8_3

Yommy, A. S., Liu, R., & Wu, A. S. (2015). SAR Image Despeckling Using Refined Lee Filter. *2015 7th International Conference on Intelligent Human-Machine Systems and Cybernetics*, *2*, 260–265. https://doi.org/10.1109/IHMSC.2015.236

Yuri Fialko, Sandwell, D., Simons, M., & Rosen, P. (2005). Three-dimensional deformation caused by the Bam, Iran, earthquake and the origin of shallow slip deficit. *Nature*, *435*(7040), 295–299. https://doi.org/10.1038/nature03425

Zha, Y., Gao, J., & Ni, S. (2003). Use of normalized difference built-up index in automatically mapping urban areas from TM imagery. *International Journal of Remote Sensing - INT J REMOTE SENS*, *24*, 583–594. https://doi.org/10.1080/01431160304987

Zhang, A., Sun, G., Ma, P., Jia, X., Ren, J., Huang, H., & Zhang, X. (2019). Coastal Wetland Mapping with Sentinel-2 MSI Imagery Based on Gravitational Optimized Multilayer

Perceptron and Morphological Attribute Profiles. *Remote Sensing*, *11*(8). http://dx.doi.org/10.3390/rs11080952

Zhang, L., He, X., Balz, T., Wei, X., & Liao, M. (2011). Rational function modeling for spaceborne SAR datasets. *ISPRS Journal of Photogrammetry and Remote Sensing*, *66*(1), 133–145. https://doi.org/10.1016/j.isprsjprs.2010.10.007

Zhao, L., Boufadel, M. C., Socolofsky, S. A., Adams, E., King, T., & Lee, K. (2014). Evolution of droplets in subsea oil and gas blowouts: Development and validation of the numerical model VDROP-J. *Marine Pollution Bulletin*, *83*(1), 58–69. https://doi.org/10.1016/j.marpolbul.2014.04.020

Zhenku, M., & Redmond, R. (1995). Tau coetficienfts for accuracy assessment for classification of remote seensing data. *Photogrammetric Engineering & Remote Sensing*, 5.

Zhong, H., Xu, J., & Jiao, L. (2009). Classification based nonlocal means despeckling for SAR image. *Proc SPIE*. https://doi.org/10.1117/12.832169

Zhou, W., & Troy, A. (2008). An object-oriented approach for analysing and characterizing urban landscape at the parcel level. *International Journal of Remote Sensing*, *29*(11), 3119–3135. https://doi.org/10.1080/01431160701469065

Appendix A: Spatial Resolution Enhancement Results

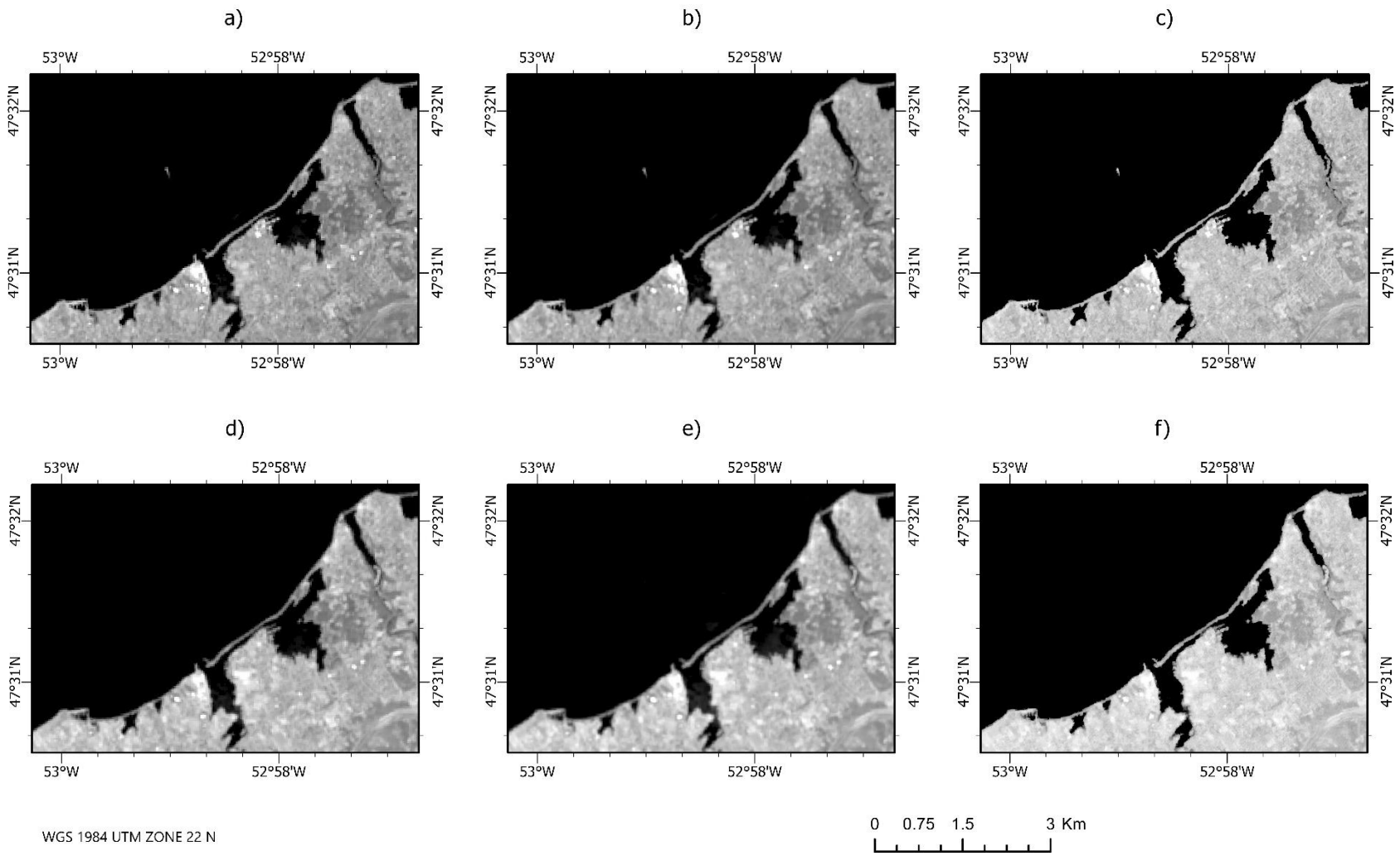

Figure A.1. Original B5 and B11 20m-resolution images (a, d) and the corresponding 10-m resolution products obtained after resampling (d, e) and super-resolution (c, f) algorithms.

Appendix B: Correlation Matrices

	B2	B3	B4	B8	B11	B12	B5	B6	B7	B8a	PC1	BI2	BI	CI	DVI	GNDVI	IPVI	IRECI	MNDWI	MSAVI	NDPI	NDTI	NDWI2	NDWI
B2	1.00	0.94	0.93	0.57	0.66	0.74	0.77	0.60	0.58	0.57	0.62	0.67	0.94	-0.06	0.39	0.29	0.57	0.30	0.00	0.38	-0.14	-0.06	-0.29	0.00
B3	0.94	1.00	0.98	0.81	0.86	0.90	0.93	0.84	0.82	0.81	0.84	0.88	1.00	-0.12	0.68	0.54	0.75	0.56	-0.01	0.67	-0.25	-0.12	-0.54	0.01
B4	0.93	0.98	1.00	0.77	0.86	0.91	0.93	0.80	0.78	0.77	0.81	0.84	0.99	-0.02	0.62	0.51	0.70	0.48	-0.01	0.61	-0.25	-0.02	-0.51	0.01
B8	0.57	0.81	0.77	1.00	0.96	0.91	0.95	1.00	1.00	1.00	1.00	0.99	0.80	-0.18	0.98	0.82	0.86	0.85	-0.02	0.97	-0.38	-0.18	-0.82	0.01
B11	0.66	0.86	0.86	0.96	1.00	0.99	0.97	0.96	0.95	0.96	0.97	0.96	0.87	-0.09	0.89	0.76	0.84	0.73	-0.02	0.88	-0.37	-0.09	-0.76	0.01
B12	0.74	0.90	0.91	0.91	0.99	1.00	0.97	0.92	0.92	0.92	0.94	0.94	0.91	-0.07	0.82	0.70	0.82	0.67	-0.02	0.81	-0.35	-0.07	-0.70	0.01
B5	0.77	0.93	0.93	0.95	0.97	0.97	1.00	0.96	0.95	0.95	0.97	0.97	0.94	-0.10	0.86	0.73	0.83	0.71	-0.02	0.85	-0.34	-0.10	-0.73	0.01
B6	0.60	0.84	0.80	1.00	0.96	0.92	0.96	1.00	1.00	1.00	1.00	0.99	0.82	-0.18	0.97	0.81	0.86	0.84	-0.02	0.96	-0.37	-0.18	-0.81	0.01
B7	0.58	0.82	0.78	1.00	0.95	0.92	0.95	1.00	1.00	1.00	1.00	0.99	0.81	-0.18	0.97	0.82	0.86	0.85	-0.02	0.97	-0.38	-0.18	-0.82	0.01
B8a	0.57	0.81	0.77	1.00	0.96	0.92	0.95	1.00	1.00	1.00	1.00	0.99	0.80	-0.17	0.98	0.82	0.86	0.85	-0.02	0.97	-0.38	-0.17	-0.82	0.01
PC1	0.62	0.84	0.81	1.00	0.97	0.94	0.97	1.00	1.00	1.00	1.00	1.00	0.84	-0.16	0.96	0.81	0.86	0.83	-0.02	0.95	-0.38	-0.16	-0.81	0.01
BI2	0.67	0.88	0.84	0.99	0.96	0.94	0.97	0.99	0.99	0.99	1.00	1.00	0.87	-0.18	0.94	0.79	0.87	0.82	-0.02	0.94	-0.36	-0.18	-0.79	0.01
BI	0.94	1.00	0.99	0.80	0.87	0.91	0.94	0.82	0.81	0.80	0.84	0.87	1.00	-0.08	0.66	0.53	0.74	0.53	-0.01	0.64	-0.25	-0.08	-0.53	0.01
CI	-0.06	-0.12	-0.02	-0.18	-0.09	-0.07	-0.10	-0.18	-0.18	-0.17	-0.16	-0.18	-0.08	1.00	-0.22	0.14	-0.37	-0.25	-0.01	-0.23	-0.06	1.00	-0.14	0.00
DVI	0.39	0.68	0.62	0.98	0.89	0.82	0.86	0.97	0.97	0.98	0.96	0.94	0.66	-0.22	1.00	0.84	0.83	0.90	-0.02	1.00	-0.38	-0.22	-0.84	0.01
GNDVI	0.29	0.54	0.51	0.82	0.76	0.70	0.73	0.81	0.82	0.82	0.81	0.79	0.53	0.14	0.84	1.00	0.66	0.74	-0.02	0.85	-0.38	0.14	-1.00	0.01
IPVI	0.57	0.75	0.70	0.86	0.84	0.82	0.83	0.86	0.86	0.86	0.86	0.87	0.74	-0.37	0.83	0.66	1.00	0.73	-0.02	0.84	-0.34	-0.37	-0.66	0.01
IRECI	0.30	0.56	0.48	0.85	0.73	0.67	0.71	0.84	0.85	0.85	0.83	0.82	0.53	-0.25	0.90	0.74	0.73	1.00	-0.02	0.90	-0.33	-0.25	-0.74	0.01
MNDWI	0.00	-0.01	-0.01	-0.02	-0.02	-0.02	-0.02	-0.02	-0.02	-0.02	-0.02	-0.02	-0.01	-0.01	-0.02	-0.02	-0.02	-0.02	1.00	-0.02	0.02	-0.01	0.02	0.21
MSAVI	0.38	0.67	0.61	0.97	0.88	0.81	0.85	0.96	0.97	0.97	0.95	0.94	0.64	-0.23	1.00	0.85	0.84	0.90	-0.02	1.00	-0.38	-0.23	-0.85	0.01
NDPI	-0.14	-0.25	-0.25	-0.38	-0.37	-0.35	-0.34	-0.37	-0.38	-0.38	-0.38	-0.36	-0.25	-0.06	-0.38	-0.38	-0.34	-0.33	0.02	-0.38	1.00	-0.06	0.38	0.00
NDTI	-0.06	-0.12	-0.02	-0.18	-0.09	-0.07	-0.10	-0.18	-0.18	-0.17	-0.16	-0.18	-0.08	1.00	-0.22	0.14	-0.37	-0.25	-0.01	-0.23	-0.06	1.00	-0.14	0.00
NDWI2	-0.29	-0.54	-0.51	-0.82	-0.76	-0.70	-0.73	-0.81	-0.82	-0.82	-0.81	-0.79	-0.53	-0.14	-0.84	-1.00	-0.66	-0.74	0.02	-0.85	0.38	-0.14	1.00	-0.01
NDWI	0.00	0.01	0.01	0.01	0.01	0.01	0.01	0.01	0.01	0.01	0.01	0.01	0.01	0.00	0.01	0.01	0.01	0.01	0.21	0.01	0.00	0.00	-0.01	1.00
PSSRA	0.18	0.33	0.27	0.51	0.42	0.39	0.42	0.50	0.51	0.51	0.49	0.49	0.31	-0.28	0.54	0.47	0.52	0.52	-0.01	0.55	-0.22	-0.28	-0.47	0.00
PVI	0.39	0.68	0.62	0.98	0.89	0.82	0.86	0.97	0.97	0.98	0.96	0.94	0.66	-0.22	1.00	0.84	0.83	0.90	-0.02	1.00	-0.38	-0.22	-0.84	0.01
TNDVI	0.58	0.76	0.71	0.85	0.83	0.82	0.83	0.85	0.85	0.85	0.85	0.85	0.74	-0.37	0.81	0.64	1.00	0.71	-0.02	0.82	-0.34	-0.37	-0.64	0.01
WDVI	0.50	0.76	0.71	1.00	0.93	0.88	0.91	0.99	0.99	0.99	0.99	0.98	0.74	-0.20	0.99	0.84	0.85	0.88	-0.02	0.99	-0.38	-0.20	-0.84	0.01
AFRI	0.60	0.72	0.68	0.71	0.72	0.74	0.73	0.72	0.71	0.71	0.72	0.74	0.71	-0.37	0.65	0.40	0.94	0.56	-0.02	0.65	-0.29	-0.37	-0.40	0.00
AFRI21	0.60	0.72	0.68	0.71	0.72	0.74	0.73	0.72	0.71	0.71	0.72	0.74	0.71	-0.37	0.65	0.40	0.94	0.56	-0.02	0.65	-0.29	-0.37	-0.40	0.00
CIRedEdge	0.39	0.68	0.62	0.98	0.89	0.82	0.86	0.97	0.97	0.98	0.96	0.94	0.66	-0.22	1.00	0.84	0.83	0.90	-0.02	1.00	-0.38	-0.22	-0.84	0.01
EVI2	0.60	0.72	0.68	0.71	0.72	0.74	0.73	0.72	0.71	0.71	0.72	0.74	0.71	-0.37	0.65	0.40	0.94	0.56	-0.02	0.65	-0.29	-0.37	-0.40	0.00
EVI	0.60	0.72	0.68	0.71	0.72	0.74	0.73	0.72	0.71	0.71	0.72	0.74	0.71	-0.37	0.65	0.40	0.94	0.56	-0.02	0.65	-0.29	-0.37	-0.40	0.00
GEMI	0.60	0.72	0.68	0.71	0.72	0.74	0.73	0.72	0.71	0.71	0.72	0.74	0.71	-0.37	0.65	0.40	0.94	0.56	-0.02	0.65	-0.29	-0.37	-0.40	0.00
GI	0.38	0.67	0.61	0.97	0.88	0.81	0.85	0.96	0.97	0.97	0.95	0.94	0.65	-0.23	1.00	0.86	0.84	0.89	-0.02	1.00	-0.39	-0.23	-0.86	0.01
GRVI	0.37	0.66	0.60	0.97	0.87	0.80	0.84	0.96	0.97	0.97	0.95	0.93	0.64	-0.24	1.00	0.85	0.83	0.90	-0.02	1.00	-0.38	-0.24	-0.85	0.01
GVI	0.46	0.71	0.66	0.94	0.89	0.84	0.86	0.93	0.94	0.94	0.93	0.92	0.69	-0.20	0.94	0.80	0.84	0.83	-0.02	0.94	-0.37	-0.20	-0.80	0.01
LAI	-0.42	-0.12	-0.22	0.43	0.20	0.05	0.13	0.39	0.42	0.42	0.36	0.33	-0.17	-0.24	0.60	0.52	0.29	0.63	-0.01	0.61	-0.20	-0.24	-0.52	0.01
MCARI2	0.60	0.72	0.68	0.71	0.72	0.74	0.73	0.72	0.71	0.71	0.72	0.74	0.71	-0.37	0.65	0.40	0.94	0.56	-0.02	0.65	-0.29	-0.37	-0.40	0.00
MCARI	0.39	0.67	0.60	0.97	0.87	0.80	0.84	0.96	0.97	0.97	0.95	0.94	0.65	-0.25	1.00	0.83	0.83	0.90	-0.02	1.00	-0.37	-0.25	-0.83	0.01
MSAVI2	0.38	0.66	0.60	0.97	0.88	0.81	0.85	0.96	0.97	0.97	0.95	0.94	0.64	-0.23	1.00	0.85	0.84	0.90	-0.02	1.00	-0.39	-0.23	-0.85	0.01
MTVI	0.60	0.72	0.68	0.71	0.72	0.74	0.73	0.72	0.71	0.71	0.72	0.74	0.71	-0.37	0.65	0.40	0.94	0.56	-0.02	0.65	-0.29	-0.37	-0.40	0.00
NDNI	0.60	0.72	0.68	0.71	0.72	0.74	0.73	0.72	0.71	0.71	0.72	0.74	0.71	-0.37	0.65	0.40	0.94	0.56	-0.02	0.65	-0.29	-0.37	-0.40	0.00
NDVI	0.37	0.66	0.59	0.96	0.87	0.80	0.84	0.95	0.96	0.96	0.94	0.93	0.63	-0.24	0.99	0.87	0.85	0.88	-0.02	0.99	-0.39	-0.24	-0.87	0.01
NMDI	0.60	0.72	0.68	0.71	0.72	0.74	0.73	0.71	0.71	0.71	0.72	0.73	0.70	-0.37	0.65	0.40	0.94	0.56	-0.02	0.65	-0.29	-0.37	-0.40	0.00
OSAVI	0.61	0.73	0.69	0.72	0.73	0.75	0.74	0.72	0.72	0.72	0.73	0.74	0.71	-0.37	0.65	0.40	0.93	0.57	-0.02	0.66	-0.29	-0.37	-0.40	0.00
PSRI	0.35	0.64	0.56	0.95	0.83	0.76	0.81	0.94	0.95	0.95	0.93	0.92	0.61	-0.29	0.99	0.83	0.83	0.91	-0.02	0.99	-0.37	-0.29	-0.83	0.01
RENDVI	0.60	0.72	0.68	0.71	0.72	0.74	0.73	0.72	0.71	0.71	0.72	0.74	0.71	-0.37	0.65	0.40	0.94	0.56	-0.02	0.65	-0.29	-0.37	-0.40	0.00
RVI	0.57	0.68	0.64	0.67	0.68	0.70	0.69	0.67	0.67	0.67	0.68	0.69	0.67	-0.35	0.61	0.38	0.89	0.53	-0.02	0.61	-0.27	-0.35	-0.38	0.00
SAVI	0.60	0.72	0.68	0.71	0.72	0.74	0.73	0.72	0.71	0.71	0.72	0.74	0.71	-0.37	0.65	0.40	0.94	0.56	-0.02	0.65	-0.29	-0.37	-0.40	0.00

Figure B.1. Matrix of correlation between Sentinel-2 bands, principal components, and spectral indices.

	PSSRA	PVI	TNDVI	WDVI	AFRI	AFRI21	CIRedEdg	EVI2	EVI	GEMI	GI	GRVI	GVI	LAI	MCARI2	MCARI	MSAVI2	MTVI	NDNI	NDVI	NMDI	OSAVI	PSRI	RENDVI	RVI	SAVI
B2	0.18	0.39	0.58	0.50	0.60	0.60	0.39	0.60	0.60	0.60	0.38	0.37	0.46	-0.42	0.60	0.39	0.38	0.60	0.60	0.37	0.60	0.61	0.35	0.60	0.57	0.60
B3	0.33	0.68	0.76	0.76	0.72	0.72	0.68	0.72	0.72	0.72	0.67	0.66	0.71	-0.12	0.72	0.67	0.66	0.72	0.72	0.66	0.72	0.73	0.64	0.72	0.68	0.72
B4	0.27	0.62	0.71	0.71	0.68	0.68	0.62	0.68	0.68	0.68	0.61	0.60	0.66	-0.22	0.68	0.60	0.60	0.68	0.68	0.59	0.68	0.69	0.56	0.68	0.64	0.68
B8	0.51	0.98	0.85	1.00	0.71	0.71	0.98	0.71	0.71	0.71	0.97	0.97	0.94	0.43	0.71	0.97	0.97	0.71	0.71	0.96	0.71	0.72	0.95	0.71	0.67	0.71
B11	0.42	0.89	0.83	0.93	0.72	0.72	0.89	0.72	0.72	0.72	0.88	0.87	0.89	0.20	0.72	0.87	0.88	0.72	0.72	0.87	0.72	0.73	0.83	0.72	0.68	0.72
B12	0.39	0.82	0.82	0.88	0.74	0.74	0.82	0.74	0.74	0.74	0.81	0.80	0.84	0.05	0.74	0.80	0.81	0.74	0.74	0.80	0.74	0.75	0.76	0.74	0.70	0.74
B5	0.42	0.86	0.83	0.91	0.73	0.73	0.86	0.73	0.73	0.73	0.85	0.84	0.86	0.13	0.73	0.84	0.85	0.73	0.73	0.84	0.73	0.74	0.81	0.73	0.69	0.73
B6	0.50	0.97	0.85	0.99	0.72	0.72	0.97	0.72	0.72	0.72	0.96	0.96	0.93	0.39	0.72	0.96	0.96	0.72	0.72	0.95	0.71	0.72	0.94	0.72	0.67	0.72
B7	0.51	0.97	0.85	0.99	0.71	0.71	0.97	0.71	0.71	0.71	0.97	0.97	0.94	0.42	0.71	0.97	0.97	0.71	0.71	0.96	0.71	0.72	0.95	0.71	0.67	0.71
B8a	0.51	0.98	0.85	0.99	0.71	0.71	0.98	0.71	0.71	0.71	0.97	0.97	0.94	0.42	0.71	0.97	0.97	0.71	0.71	0.96	0.71	0.72	0.95	0.71	0.67	0.71
PC1	0.49	0.96	0.85	0.99	0.72	0.72	0.96	0.72	0.72	0.72	0.95	0.95	0.93	0.36	0.72	0.95	0.95	0.72	0.72	0.94	0.72	0.73	0.93	0.72	0.68	0.72
BI2	0.49	0.94	0.85	0.98	0.74	0.74	0.94	0.74	0.74	0.74	0.94	0.93	0.92	0.33	0.74	0.94	0.94	0.74	0.74	0.93	0.73	0.74	0.92	0.74	0.69	0.74
BI	0.31	0.66	0.74	0.74	0.71	0.71	0.66	0.71	0.71	0.71	0.65	0.64	0.69	-0.17	0.71	0.65	0.64	0.71	0.71	0.63	0.70	0.71	0.61	0.71	0.67	0.71
CI	-0.28	-0.22	-0.37	-0.20	-0.37	-0.37	-0.22	-0.37	-0.37	-0.37	-0.23	-0.24	-0.20	-0.24	-0.37	-0.25	-0.23	-0.37	-0.37	-0.24	-0.37	-0.37	-0.29	-0.37	-0.35	-0.37
DVI	0.54	1.00	0.81	0.99	0.65	0.65	1.00	0.65	0.65	0.65	1.00	1.00	0.94	0.60	0.65	1.00	1.00	0.65	0.65	0.99	0.65	0.65	0.99	0.65	0.61	0.65
GNDVI	0.47	0.84	0.64	0.84	0.40	0.40	0.84	0.40	0.40	0.40	0.86	0.85	0.80	0.52	0.40	0.83	0.85	0.40	0.40	0.87	0.40	0.40	0.83	0.40	0.38	0.40
IPVI	0.52	0.83	1.00	0.85	0.94	0.94	0.83	0.94	0.94	0.94	0.84	0.83	0.84	0.29	0.94	0.83	0.84	0.94	0.94	0.85	0.94	0.93	0.83	0.94	0.89	0.94
IRECI	0.52	0.90	0.71	0.88	0.56	0.56	0.90	0.56	0.56	0.56	0.89	0.90	0.83	0.63	0.56	0.90	0.90	0.56	0.56	0.88	0.56	0.57	0.91	0.56	0.53	0.56
MNDWI	-0.01	-0.02	-0.02	-0.02	-0.02	-0.02	-0.02	-0.02	-0.02	-0.02	-0.02	-0.02	-0.02	-0.01	-0.02	-0.02	-0.02	-0.02	-0.02	-0.02	-0.02	-0.02	-0.02	-0.02	-0.02	-0.02
MSAVI	0.55	1.00	0.82	0.99	0.65	0.65	1.00	0.65	0.65	0.65	1.00	1.00	0.94	0.61	0.65	1.00	1.00	0.65	0.65	0.99	0.65	0.66	0.99	0.65	0.61	0.65
NDPI	-0.22	-0.38	-0.34	-0.38	-0.29	-0.29	-0.38	-0.29	-0.29	-0.29	-0.39	-0.38	-0.37	-0.20	-0.29	-0.37	-0.39	-0.29	-0.29	-0.39	-0.29	-0.29	-0.37	-0.29	-0.27	-0.29
NDTI	-0.28	-0.22	-0.37	-0.20	-0.37	-0.37	-0.22	-0.37	-0.37	-0.37	-0.23	-0.24	-0.20	-0.24	-0.37	-0.25	-0.23	-0.37	-0.37	-0.24	-0.37	-0.37	-0.29	-0.37	-0.35	-0.37
NDWI2	-0.47	-0.84	-0.64	-0.84	-0.40	-0.40	-0.84	-0.40	-0.40	-0.40	-0.86	-0.85	-0.80	-0.52	-0.40	-0.83	-0.85	-0.40	-0.40	-0.87	-0.40	-0.40	-0.83	-0.40	-0.38	-0.40
NDWI	0.00	0.01	0.01	0.01	0.00	0.00	0.01	0.00	0.00	0.00	0.01	0.01	0.01	0.01	0.00	0.01	0.01	0.00	0.00	0.01	0.00	0.00	0.01	0.00	0.00	0.00
PSSRA	1.00	0.54	0.51	0.52	0.42	0.42	0.54	0.42	0.42	0.42	0.55	0.55	0.51	0.39	0.42	0.55	0.55	0.42	0.42	0.56	0.42	0.42	0.57	0.42	0.40	0.42
PVI	0.54	1.00	0.81	0.99	0.65	0.65	1.00	0.65	0.65	0.65	1.00	1.00	0.94	0.60	0.65	1.00	1.00	0.65	0.65	0.99	0.65	0.65	0.99	0.65	0.61	0.65
TNDVI	0.51	0.81	1.00	0.83	0.94	0.94	0.81	0.94	0.94	0.94	0.82	0.81	0.83	0.26	0.94	0.81	0.82	0.94	0.94	0.83	0.94	0.94	0.81	0.94	0.89	0.94
WDVI	0.52	0.99	0.83	1.00	0.68	0.68	0.99	0.69	0.68	0.68	0.99	0.99	0.95	0.51	0.68	0.99	0.99	0.68	0.68	0.98	0.68	0.69	0.97	0.68	0.65	0.68
AFRI	0.42	0.65	0.94	0.68	1.00	1.00	0.65	1.00	1.00	1.00	0.65	0.65	0.69	0.08	1.00	0.65	0.65	1.00	1.00	0.65	1.00	0.99	0.64	1.00	0.94	1.00
AFRI21	0.42	0.65	0.94	0.68	1.00	1.00	0.65	1.00	1.00	1.00	0.65	0.65	0.69	0.08	1.00	0.65	0.65	1.00	1.00	0.65	1.00	0.99	0.64	1.00	0.94	1.00
CIRedEdge	0.54	1.00	0.81	0.99	0.65	0.65	1.00	0.65	0.65	0.65	1.00	1.00	0.94	0.60	0.65	1.00	1.00	0.65	0.65	0.99	0.65	0.65	0.99	0.65	0.61	0.65
EVI2	0.42	0.65	0.94	0.69	1.00	1.00	0.65	1.00	1.00	1.00	0.65	0.65	0.69	0.08	1.00	0.65	0.65	1.00	1.00	0.65	1.00	0.99	0.64	1.00	0.94	1.00
EVI	0.42	0.65	0.94	0.68	1.00	1.00	0.65	1.00	1.00	1.00	0.65	0.65	0.69	0.08	1.00	0.65	0.65	1.00	1.00	0.65	1.00	0.99	0.64	1.00	0.94	1.00
GEMI	0.42	0.65	0.94	0.68	1.00	1.00	0.65	1.00	1.00	1.00	0.65	0.65	0.69	0.08	1.00	0.65	0.65	1.00	1.00	0.65	1.00	0.99	0.64	1.00	0.94	1.00
GI	0.55	1.00	0.82	0.99	0.65	0.65	1.00	0.65	0.65	0.65	1.00	1.00	0.94	0.61	0.65	0.99	1.00	0.65	0.65	1.00	0.65	0.66	0.99	0.65	0.62	0.65
GRVI	0.55	1.00	0.81	0.99	0.65	0.65	1.00	0.65	0.65	0.65	1.00	1.00	0.94	0.62	0.65	1.00	1.00	0.65	0.65	0.99	0.65	0.65	0.99	0.65	0.61	0.65
GVI	0.51	0.94	0.83	0.95	0.69	0.69	0.94	0.69	0.69	0.69	0.94	0.94	1.00	0.47	0.69	0.94	0.94	0.69	0.69	0.94	0.69	0.70	0.93	0.69	0.65	0.69
LAI	0.39	0.60	0.26	0.51	0.08	0.08	0.60	0.08	0.08	0.08	0.61	0.62	0.47	1.00	0.08	0.62	0.62	0.08	0.08	0.61	0.08	0.08	0.65	0.08	0.08	0.08
MCARI2	0.42	0.65	0.94	0.68	1.00	1.00	0.65	1.00	1.00	1.00	0.65	0.65	0.69	0.08	1.00	0.65	0.65	1.00	1.00	0.65	1.00	0.99	0.64	1.00	0.94	1.00
MCARI	0.55	1.00	0.81	0.99	0.65	0.65	1.00	0.65	0.65	0.65	0.99	1.00	0.94	0.62	0.65	1.00	1.00	0.65	0.65	0.99	0.65	0.66	0.99	0.65	0.61	0.65
MSAVI2	0.55	1.00	0.82	0.99	0.65	0.65	1.00	0.65	0.65	0.65	1.00	1.00	0.94	0.62	0.65	1.00	1.00	0.65	0.65	1.00	0.65	0.66	0.99	0.65	0.61	0.65
MTVI	0.42	0.65	0.94	0.68	1.00	1.00	0.65	1.00	1.00	1.00	0.65	0.65	0.69	0.08	1.00	0.65	0.65	1.00	1.00	0.65	1.00	0.99	0.64	1.00	0.94	1.00
NDNI	0.42	0.65	0.94	0.68	1.00	1.00	0.65	1.00	1.00	1.00	0.65	0.65	0.69	0.08	1.00	0.65	0.65	1.00	1.00	0.65	1.00	0.99	0.64	1.00	0.94	1.00
NDVI	0.56	0.99	0.83	0.98	0.65	0.65	0.99	0.65	0.65	0.65	1.00	0.99	0.94	0.61	0.65	0.99	1.00	0.65	0.65	1.00	0.65	0.66	0.99	0.65	0.62	0.65
NMDI	0.42	0.65	0.94	0.68	1.00	1.00	0.65	1.00	1.00	1.00	0.65	0.65	0.69	0.08	1.00	0.65	0.65	1.00	1.00	0.65	1.00	0.99	0.64	1.00	0.94	1.00
OSAVI	0.42	0.65	0.94	0.69	0.99	0.99	0.65	0.99	0.99	0.99	0.66	0.65	0.70	0.08	0.99	0.66	0.66	0.99	0.99	0.66	0.99	1.00	0.65	0.99	0.93	0.99
PSRI	0.57	0.99	0.81	0.97	0.64	0.64	0.99	0.64	0.64	0.64	0.99	0.99	0.93	0.65	0.64	0.99	0.99	0.64	0.64	0.99	0.64	0.65	1.00	0.64	0.61	0.64
RENDVI	0.42	0.65	0.94	0.68	1.00	1.00	0.65	1.00	1.00	1.00	0.65	0.65	0.69	0.08	1.00	0.65	0.65	1.00	1.00	0.65	1.00	0.99	0.64	1.00	0.94	1.00
RVI	0.40	0.61	0.89	0.65	0.94	0.94	0.61	0.94	0.94	0.94	0.62	0.61	0.65	0.08	0.94	0.61	0.61	0.94	0.94	0.62	0.94	0.93	0.61	0.94	1.00	0.94
SAVI	0.42	0.65	0.94	0.68	1.00	1.00	0.65	1.00	1.00	1.00	0.65	0.65	0.69	0.08	1.00	0.65	0.65	1.00	1.00	0.65	1.00	0.99	0.64	1.00	0.94	1.00

Figure B.1. Matrix of correlation between Sentinel-2 bands, principal components, and spectral indices [continue].

Band	GLCM texture measure	CON	DISS	HOM	ASM	E	MAX	ENT	MEAN	CORR	VAR	CON	DISS	HOM	ASM	E	MAX	ENT	MEAN	CORR	VAR	CON	DISS	HOM	ASM	E	MAX	ENT	MEAN	CORR	VAR	CON	DISS	HOM	ASM	E	MAX	ENT	MEAN	CORR	VAR
B2	CON	1.00	0.92	0.27	0.04	0.22	0.10	0.74	0.53	0.46	0.50	0.70	0.78	0.37	0.13	0.30	0.20	0.70	0.58	0.55	0.53	0.80	0.84	0.31	0.08	0.24	0.14	0.73	0.57	0.53	0.53	0.50	0.55	0.46	0.40	0.45	0.43	0.24	0.58	0.55	0.53
	DISS	0.92	1.00	0.45	0.10	0.36	0.19	0.94	0.73	0.62	0.73	0.62	0.83	0.58	0.27	0.48	0.37	0.83	0.78	0.74	0.76	0.73	0.90	0.52	0.18	0.41	0.28	0.87	0.77	0.71	0.75	0.44	0.57	0.67	0.59	0.64	0.61	0.26	0.78	0.74	0.75
	HOM	0.27	0.45	1.00	0.82	0.97	0.90	0.50	0.72	0.65	0.91	0.19	0.39	0.95	0.86	0.95	0.90	0.34	0.71	0.66	0.90	0.23	0.42	0.97	0.84	0.95	0.89	0.36	0.70	0.64	0.91	0.16	0.26	0.90	0.82	0.87	0.85	-0.03	0.68	0.63	0.90
	ASM	0.04	0.10	0.82	1.00	0.92	0.98	0.03	0.38	0.38	0.58	0.05	0.10	0.69	0.83	0.77	0.79	-0.04	0.33	0.31	0.56	0.05	0.09	0.73	0.85	0.80	0.83	-0.04	0.34	0.32	0.57	0.06	0.08	0.60	0.59	0.60	0.59	-0.16	0.31	0.28	0.57
	E	0.22	0.36	0.97	0.92	1.00	0.97	0.35	0.63	0.58	0.83	0.17	0.32	0.90	0.89	0.92	0.90	0.23	0.61	0.57	0.82	0.20	0.33	0.92	0.88	0.94	0.91	0.23	0.60	0.55	0.82	0.15	0.22	0.83	0.77	0.81	0.79	-0.08	0.58	0.53	0.82
	MAX	0.10	0.19	0.90	0.98	0.97	1.00	0.15	0.49	0.46	0.69	0.09	0.18	0.79	0.87	0.84	0.85	0.06	0.44	0.41	0.67	0.11	0.18	0.82	0.88	0.87	0.88	0.06	0.44	0.41	0.68	0.10	0.14	0.70	0.67	0.69	0.68	-0.13	0.42	0.38	0.67
	ENT	0.74	0.94	0.50	0.03	0.35	0.15	1.00	0.78	0.65	0.80	0.48	0.76	0.64	0.28	0.52	0.39	0.84	0.85	0.79	0.81	0.59	0.85	0.58	0.18	0.44	0.29	0.90	0.83	0.75	0.81	0.33	0.51	0.72	0.63	0.69	0.65	0.26	0.84	0.79	0.81
	MEAN	0.53	0.73	0.72	0.38	0.63	0.49	0.78	1.00	0.97	0.88	0.32	0.57	0.80	0.58	0.74	0.65	0.59	0.95	0.94	0.87	0.39	0.62	0.78	0.50	0.69	0.59	0.63	0.96	0.95	0.87	0.22	0.40	0.80	0.70	0.76	0.73	0.16	0.91	0.87	0.87
	CORR	0.46	0.62	0.65	0.38	0.58	0.46	0.65	0.97	1.00	0.77	0.26	0.47	0.71	0.55	0.67	0.61	0.47	0.88	0.90	0.76	0.32	0.51	0.70	0.50	0.65	0.57	0.49	0.91	0.93	0.76	0.19	0.34	0.70	0.62	0.67	0.64	0.13	0.84	0.81	0.75
	VAR	0.50	0.73	0.91	0.58	0.83	0.69	0.80	0.88	0.77	1.00	0.32	0.60	0.95	0.73	0.89	0.81	0.61	0.89	0.83	1.00	0.40	0.65	0.93	0.67	0.86	0.75	0.65	0.88	0.80	1.00	0.22	0.39	0.95	0.85	0.91	0.88	0.09	0.86	0.81	1.00
B3	CON	0.70	0.62	0.19	0.05	0.17	0.09	0.48	0.32	0.26	0.32	1.00	0.88	0.16	0.03	0.13	0.07	0.64	0.29	0.24	0.32	0.90	0.76	0.17	0.03	0.14	0.07	0.55	0.30	0.24	0.32	0.83	0.82	0.19	0.09	0.16	0.12	0.52	0.29	0.24	0.33
	DISS	0.78	0.83	0.39	0.10	0.32	0.18	0.76	0.57	0.47	0.60	0.88	1.00	0.38	0.11	0.30	0.19	0.91	0.55	0.47	0.60	0.86	0.92	0.39	0.12	0.30	0.19	0.81	0.55	0.45	0.60	0.71	0.86	0.43	0.29	0.38	0.33	0.61	0.53	0.46	0.60
	HOM	0.37	0.58	0.95	0.69	0.90	0.79	0.64	0.80	0.71	0.95	0.16	0.38	1.00	0.88	0.98	0.93	0.36	0.83	0.80	0.95	0.24	0.47	0.97	0.78	0.93	0.85	0.45	0.82	0.77	0.95	0.11	0.20	0.97	0.92	0.96	0.94	-0.14	0.82	0.78	0.95
	ASM	0.13	0.27	0.86	0.83	0.89	0.87	0.28	0.58	0.55	0.73	0.03	0.11	0.88	1.00	0.95	0.98	-0.03	0.58	0.57	0.72	0.07	0.18	0.86	0.88	0.89	0.89	0.09	0.58	0.57	0.73	0.02	0.03	0.79	0.79	0.80	0.80	-0.28	0.56	0.55	0.72
	E	0.30	0.48	0.95	0.77	0.92	0.84	0.52	0.74	0.67	0.89	0.13	0.30	0.98	0.95	1.00	0.98	0.22	0.76	0.73	0.89	0.19	0.38	0.96	0.84	0.94	0.89	0.33	0.75	0.72	0.89	0.09	0.15	0.93	0.90	0.92	0.91	-0.20	0.74	0.72	0.89
	MAX	0.20	0.37	0.90	0.79	0.90	0.85	0.39	0.65	0.61	0.81	0.07	0.19	0.93	0.98	0.98	1.00	0.07	0.67	0.66	0.80	0.12	0.26	0.91	0.86	0.92	0.89	0.20	0.66	0.65	0.80	0.05	0.08	0.86	0.85	0.86	0.86	-0.26	0.65	0.64	0.80
	ENT	0.70	0.83	0.34	-0.04	0.23	0.06	0.84	0.59	0.47	0.61	0.64	0.91	0.36	-0.03	0.22	0.07	1.00	0.59	0.50	0.62	0.69	0.87	0.35	0.00	0.22	0.09	0.89	0.57	0.46	0.61	0.49	0.73	0.44	0.27	0.37	0.31	0.62	0.56	0.48	0.61
	MEAN	0.58	0.78	0.71	0.33	0.61	0.44	0.85	0.95	0.88	0.89	0.29	0.55	0.83	0.58	0.76	0.67	0.59	1.00	0.99	0.90	0.41	0.67	0.77	0.44	0.66	0.54	0.71	0.99	0.96	0.89	0.19	0.32	0.87	0.81	0.85	0.82	0.01	0.99	0.97	0.89
	CORR	0.55	0.74	0.66	0.31	0.57	0.41	0.79	0.94	0.90	0.83	0.24	0.47	0.80	0.57	0.73	0.66	0.50	0.99	1.00	0.84	0.36	0.60	0.73	0.43	0.63	0.53	0.63	0.99	0.98	0.84	0.15	0.24	0.83	0.80	0.83	0.81	-0.08	0.98	0.98	0.84
	VAR	0.53	0.76	0.90	0.56	0.82	0.67	0.81	0.87	0.76	1.00	0.32	0.60	0.95	0.72	0.89	0.80	0.62	0.90	0.84	1.00	0.41	0.67	0.93	0.65	0.84	0.74	0.67	0.88	0.81	1.00	0.22	0.39	0.96	0.86	0.92	0.89	0.08	0.88	0.82	1.00
B4	CON	0.80	0.73	0.23	0.05	0.20	0.11	0.59	0.39	0.32	0.40	0.90	0.86	0.24	0.07	0.19	0.12	0.69	0.41	0.36	0.41	1.00	0.89	0.21	0.02	0.15	0.07	0.68	0.40	0.33	0.41	0.79	0.79	0.29	0.20	0.26	0.23	0.46	0.41	0.37	0.41
	DISS	0.84	0.90	0.42	0.09	0.33	0.18	0.85	0.62	0.51	0.65	0.76	0.92	0.47	0.18	0.38	0.26	0.87	0.67	0.60	0.67	0.89	1.00	0.40	0.07	0.29	0.15	0.93	0.64	0.55	0.66	0.62	0.76	0.53	0.41	0.49	0.45	0.47	0.66	0.60	0.67
	HOM	0.31	0.52	0.97	0.73	0.92	0.82	0.58	0.78	0.70	0.93	0.17	0.39	0.97	0.86	0.96	0.91	0.35	0.77	0.73	0.93	0.21	0.40	1.00	0.87	0.98	0.92	0.35	0.76	0.72	0.93	0.12	0.21	0.94	0.88	0.92	0.90	-0.10	0.74	0.70	0.93
	ASM	0.08	0.18	0.84	0.85	0.88	0.88	0.18	0.50	0.50	0.67	0.03	0.12	0.78	0.88	0.84	0.86	0.00	0.44	0.43	0.65	0.02	0.07	0.87	1.00	0.95	0.99	-0.08	0.46	0.46	0.66	0.02	0.04	0.71	0.71	0.72	0.71	-0.24	0.42	0.39	0.66
	E	0.24	0.41	0.95	0.80	0.94	0.87	0.44	0.69	0.65	0.86	0.14	0.30	0.93	0.89	0.94	0.92	0.22	0.66	0.63	0.84	0.15	0.29	0.98	0.95	1.00	0.98	0.19	0.67	0.64	0.85	0.09	0.16	0.88	0.84	0.87	0.85	-0.16	0.63	0.60	0.85
	MAX	0.14	0.28	0.89	0.83	0.91	0.88	0.29	0.59	0.57	0.75	0.07	0.19	0.85	0.89	0.89	0.89	0.09	0.54	0.53	0.74	0.07	0.15	0.92	0.99	0.98	1.00	0.02	0.55	0.55	0.74	0.05	0.08	0.79	0.77	0.79	0.78	-0.22	0.51	0.49	0.74
	ENT	0.73	0.87	0.36	-0.04	0.23	0.06	0.90	0.63	0.49	0.65	0.55	0.81	0.45	0.09	0.33	0.20	0.89	0.71	0.63	0.67	0.68	0.93	0.35	-0.08	0.19	0.02	1.00	0.67	0.56	0.66	0.42	0.62	0.53	0.40	0.48	0.43	0.45	0.70	0.64	0.66
	MEAN	0.57	0.77	0.70	0.34	0.60	0.44	0.83	0.96	0.91	0.88	0.30	0.55	0.82	0.58	0.75	0.66	0.57	0.99	0.99	0.88	0.40	0.64	0.76	0.46	0.67	0.55	0.67	1.00	0.98	0.88	0.19	0.32	0.85	0.79	0.83	0.81	0.02	0.98	0.96	0.88
	CORR	0.53	0.71	0.64	0.32	0.55	0.41	0.75	0.95	0.93	0.80	0.24	0.45	0.77	0.57	0.72	0.65	0.46	0.96	0.98	0.81	0.33	0.55	0.72	0.46	0.64	0.55	0.56	0.98	1.00	0.81	0.15	0.23	0.80	0.77	0.80	0.78	-0.07	0.95	0.95	0.81
	VAR	0.53	0.75	0.91	0.57	0.82	0.68	0.81	0.87	0.76	1.00	0.32	0.60	0.95	0.73	0.89	0.80	0.61	0.89	0.84	1.00	0.41	0.66	0.93	0.66	0.85	0.74	0.66	0.88	0.81	1.00	0.22	0.38	0.96	0.87	0.93	0.89	0.07	0.87	0.82	1.00
B8	CON	0.50	0.44	0.16	0.06	0.15	0.10	0.33	0.22	0.19	0.22	0.83	0.71	0.11	0.02	0.09	0.05	0.49	0.19	0.15	0.22	0.79	0.62	0.12	0.02	0.09	0.05	0.42	0.19	0.15	0.22	1.00	0.88	0.10	0.00	0.07	0.04	0.51	0.18	0.14	0.21
	DISS	0.55	0.57	0.26	0.08	0.22	0.14	0.51	0.40	0.34	0.39	0.82	0.86	0.20	0.03	0.15	0.08	0.73	0.32	0.24	0.39	0.79	0.76	0.21	0.04	0.16	0.08	0.62	0.32	0.23	0.38	0.88	1.00	0.16	0.00	0.10	0.04	0.80	0.28	0.19	0.37
	HOM	0.46	0.67	0.90	0.60	0.83	0.70	0.72	0.80	0.70	0.95	0.19	0.43	0.97	0.79	0.93	0.86	0.44	0.87	0.83	0.96	0.29	0.53	0.94	0.71	0.88	0.79	0.53	0.85	0.80	0.96	0.10	0.16	1.00	0.97	0.99	0.98	-0.21	0.86	0.84	0.96
	ASM	0.40	0.59	0.82	0.59	0.77	0.67	0.63	0.70	0.62	0.85	0.09	0.29	0.92	0.79	0.90	0.85	0.27	0.81	0.80	0.86	0.20	0.41	0.88	0.71	0.84	0.77	0.40	0.79	0.77	0.87	0.00	0.00	0.97	1.00	0.99	1.00	-0.41	0.82	0.83	0.87
	E	0.45	0.64	0.87	0.60	0.81	0.69	0.69	0.76	0.67	0.91	0.16	0.38	0.96	0.80	0.92	0.86	0.37	0.85	0.83	0.92	0.26	0.49	0.92	0.72	0.87	0.79	0.48	0.83	0.80	0.93	0.07	0.10	0.99	0.99	1.00	1.00	-0.30	0.85	0.84	0.93
	MAX	0.43	0.61	0.85	0.59	0.79	0.68	0.65	0.73	0.64	0.88	0.12	0.33	0.94	0.80	0.91	0.86	0.31	0.82	0.81	0.89	0.23	0.45	0.90	0.71	0.85	0.78	0.43	0.81	0.78	0.89	0.04	0.04	0.98	1.00	1.00	1.00	-0.37	0.83	0.84	0.89
	ENT	0.24	0.26	-0.03	-0.16	-0.08	-0.13	0.26	0.16	0.13	0.09	0.52	0.61	-0.14	-0.28	-0.20	-0.26	0.62	0.01	-0.08	0.08	0.46	0.47	-0.10	-0.24	-0.16	-0.22	0.45	0.02	-0.07	0.07	0.51	0.80	-0.21	-0.41	-0.30	-0.37	1.00	-0.05	-0.16	0.07
	MEAN	0.58	0.78	0.68	0.31	0.58	0.42	0.84	0.91	0.84	0.86	0.29	0.53	0.82	0.56	0.74	0.65	0.56	0.99	0.98	0.88	0.41	0.66	0.74	0.42	0.63	0.51	0.70	0.98	0.95	0.87	0.18	0.28	0.86	0.82	0.85	0.83	-0.05	1.00	0.99	0.87
	CORR	0.55	0.74	0.63	0.28	0.53	0.38	0.79	0.87	0.81	0.81	0.24	0.46	0.78	0.55	0.72	0.64	0.48	0.97	0.98	0.82	0.37	0.60	0.70	0.39	0.60	0.49	0.64	0.96	0.95	0.82	0.14	0.19	0.84	0.83	0.84	0.84	-0.16	0.99	1.00	0.82
	VAR	0.53	0.75	0.90	0.57	0.82	0.67	0.81	0.87	0.75	1.00	0.33	0.60	0.95	0.72	0.89	0.80	0.61	0.89	0.84	1.00	0.41	0.67	0.93	0.66	0.85	0.74	0.66	0.88	0.81	1.00	0.21	0.37	0.96	0.87	0.93	0.89	0.07	0.87	0.82	1.00

Figure B.2. Correlation matrix of GLCM texture measures obtained from Sentinel-2 VNIR bands.

Appendix C: Box-and-Whiskers Plots

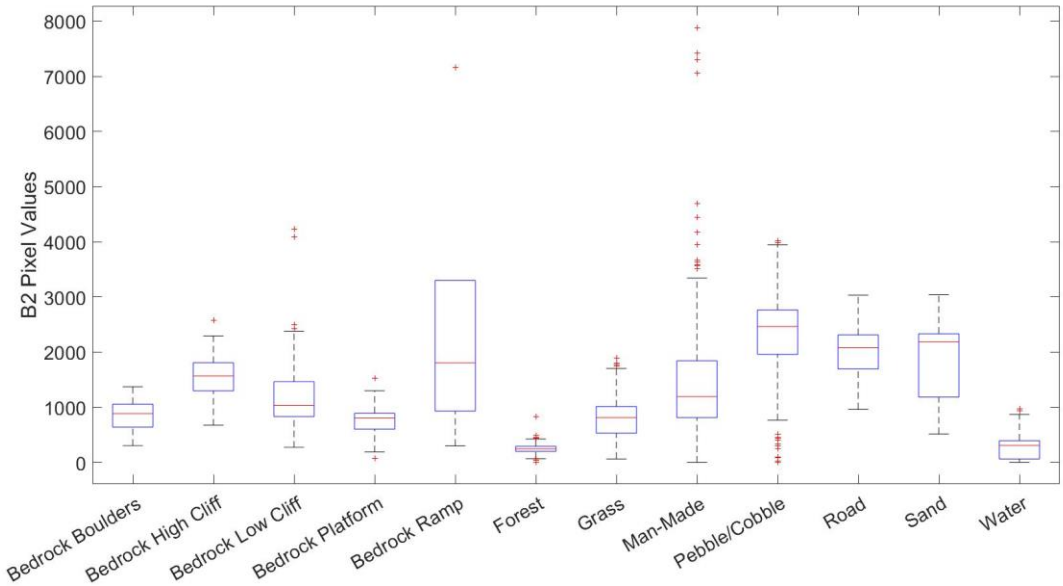

Figure C.1. Pixel distributions of the shoreline classes in Sentinel-2 B2.

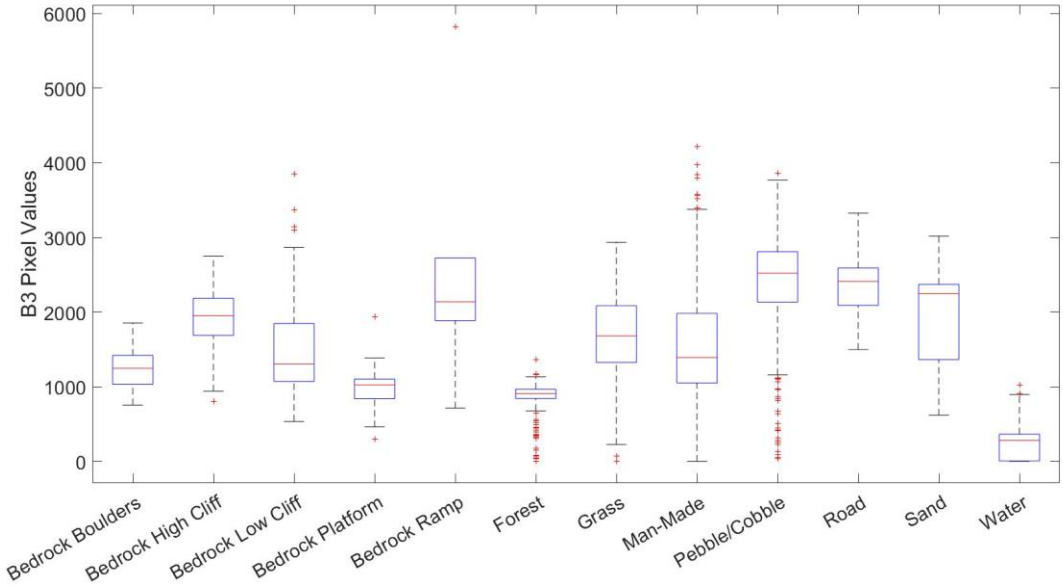

Figure C.2. Pixel distributions of the shoreline classes in Sentinel-2 B3.

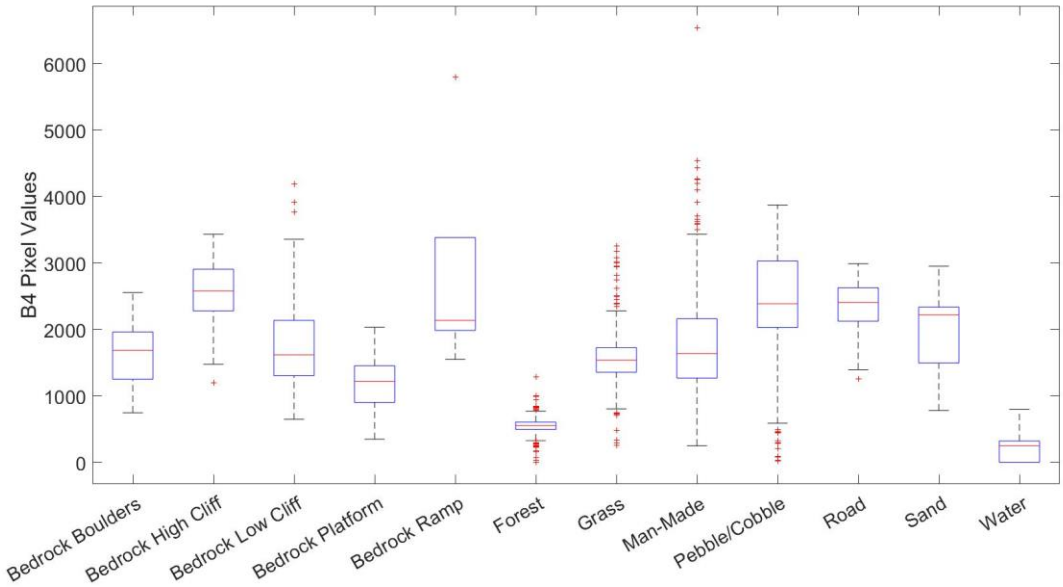

Figure C.3. Pixel distributions of the shoreline classes in Sentinel-2 B4.

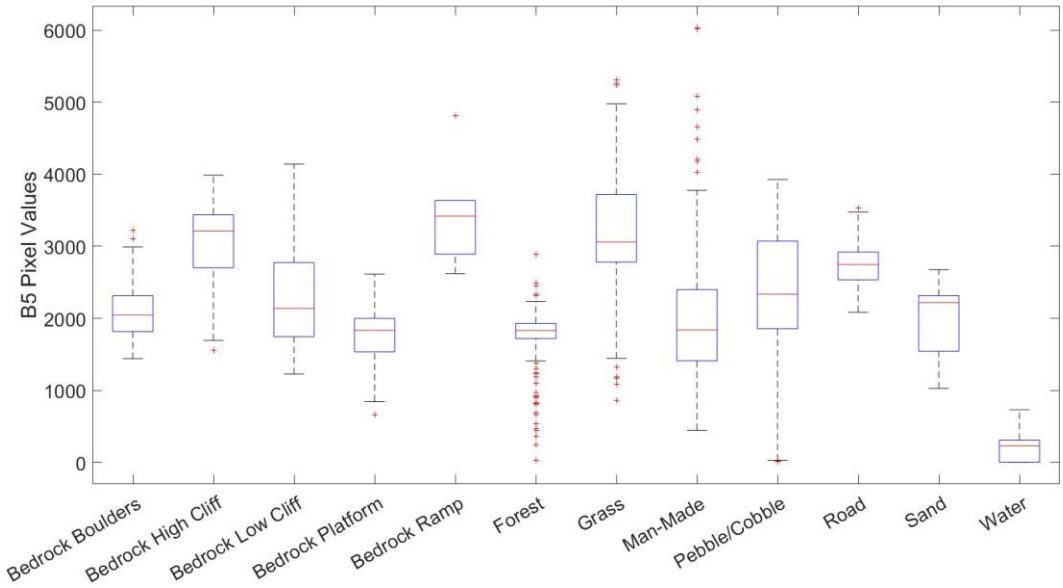

Figure C.4. Pixel distributions of the shoreline classes in Sentinel-2 B5.

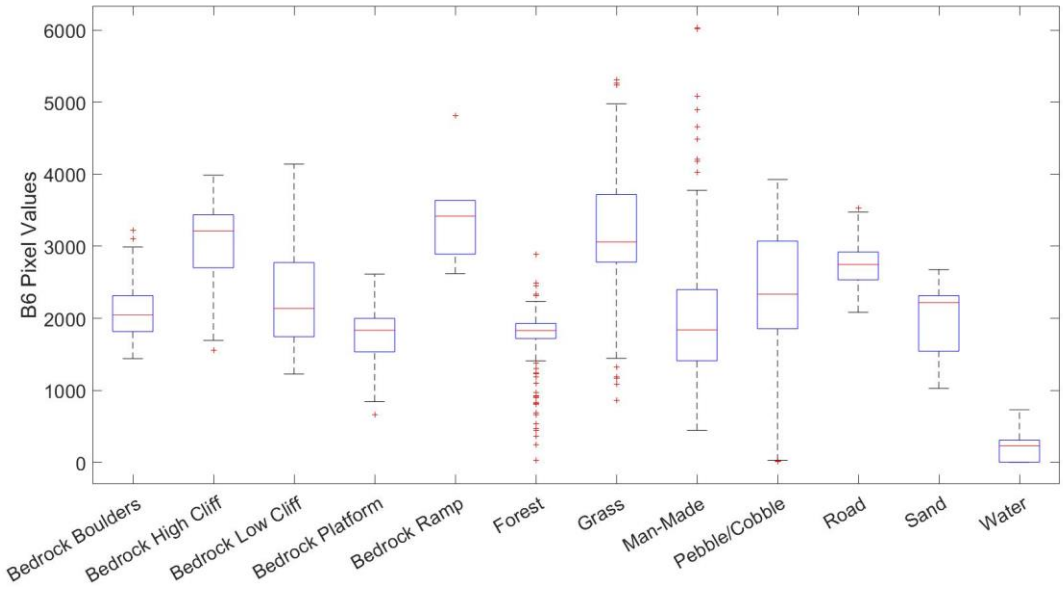

Figure C.5. Pixel distributions of the shoreline classes in Sentinel-2 B6.

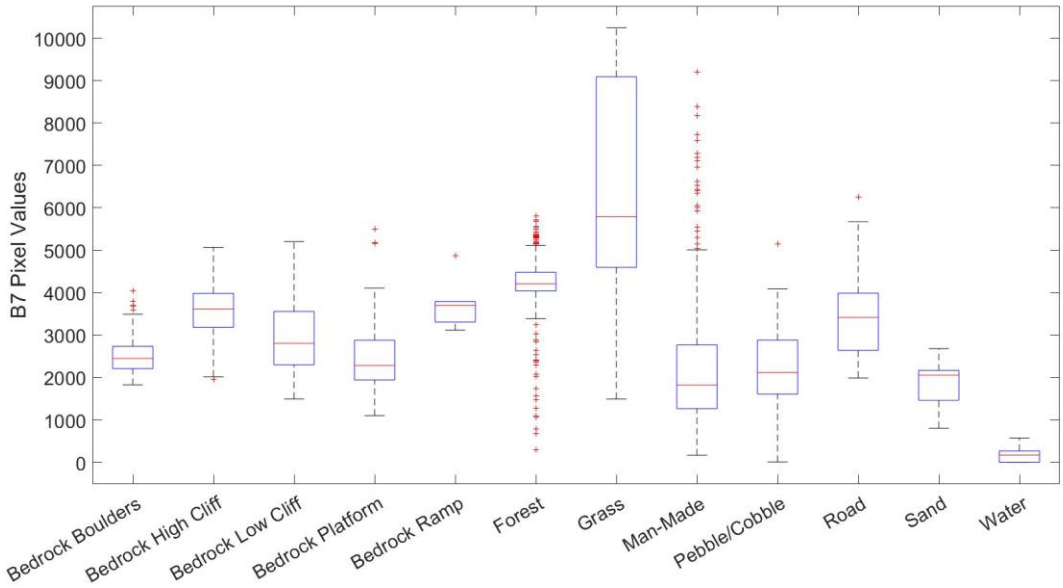

Figure C.6. Pixel distributions of the shoreline classes in Sentinel-2 B7.

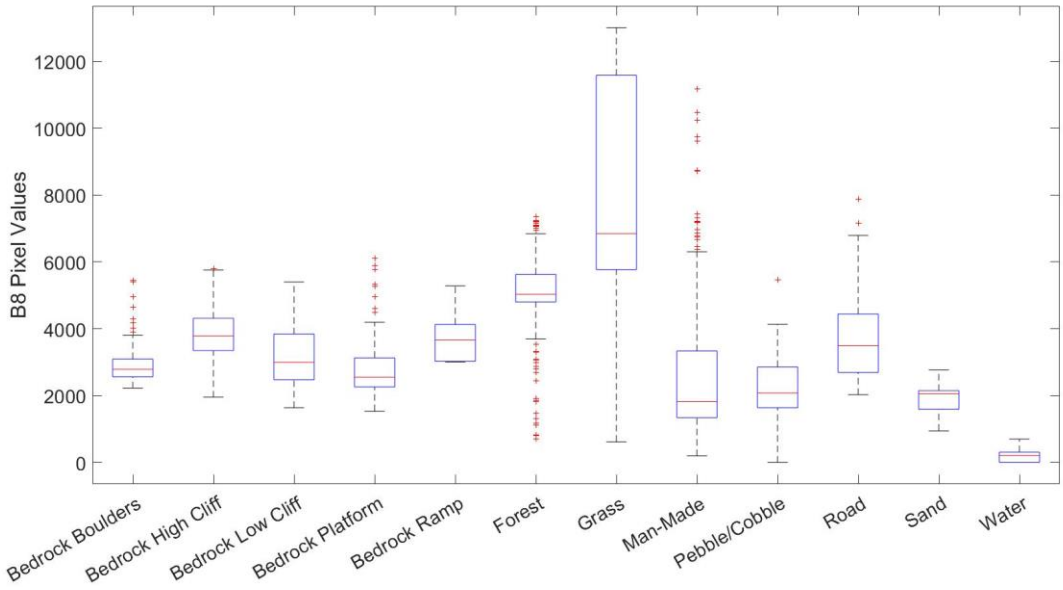

Figure C.7. Pixel distributions of the shoreline classes in Sentinel-2 B8.

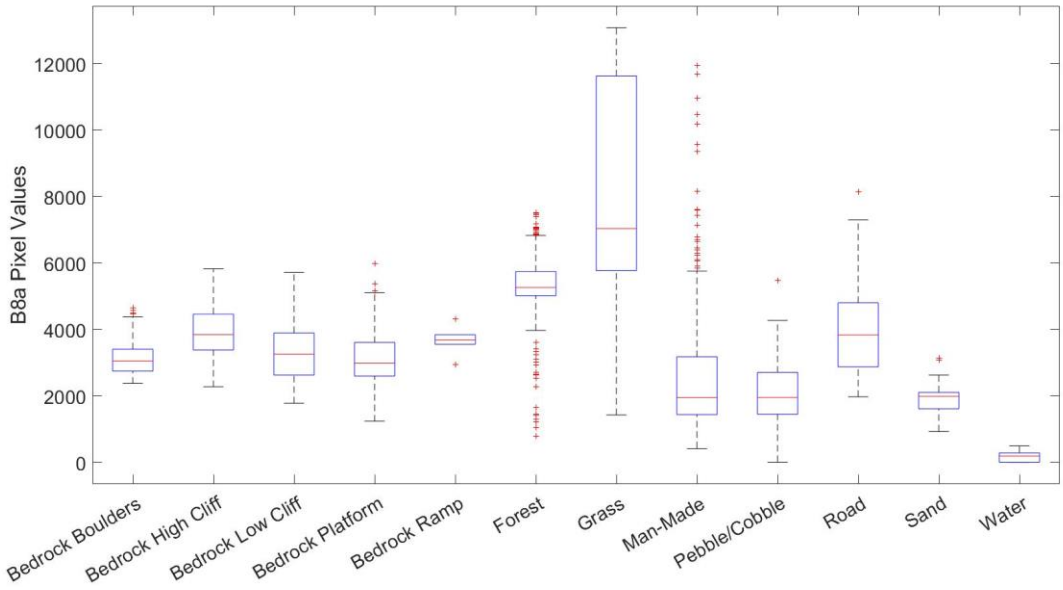

Figure C.8. Pixel distributions of the shoreline classes in Sentinel-2 B8a.

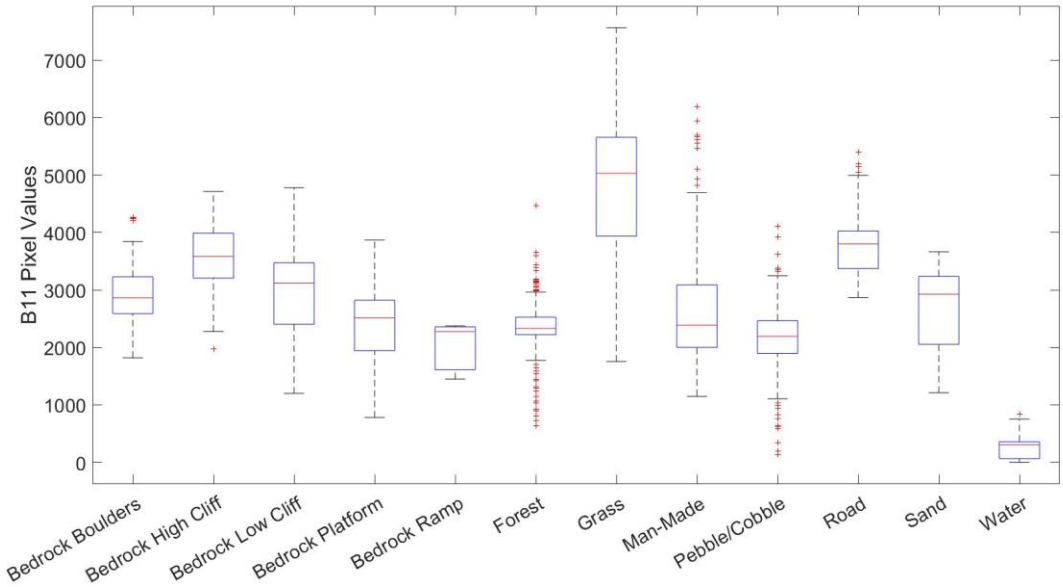

Figure C.9. Pixel distributions of the shoreline classes in Sentinel-2 B11.

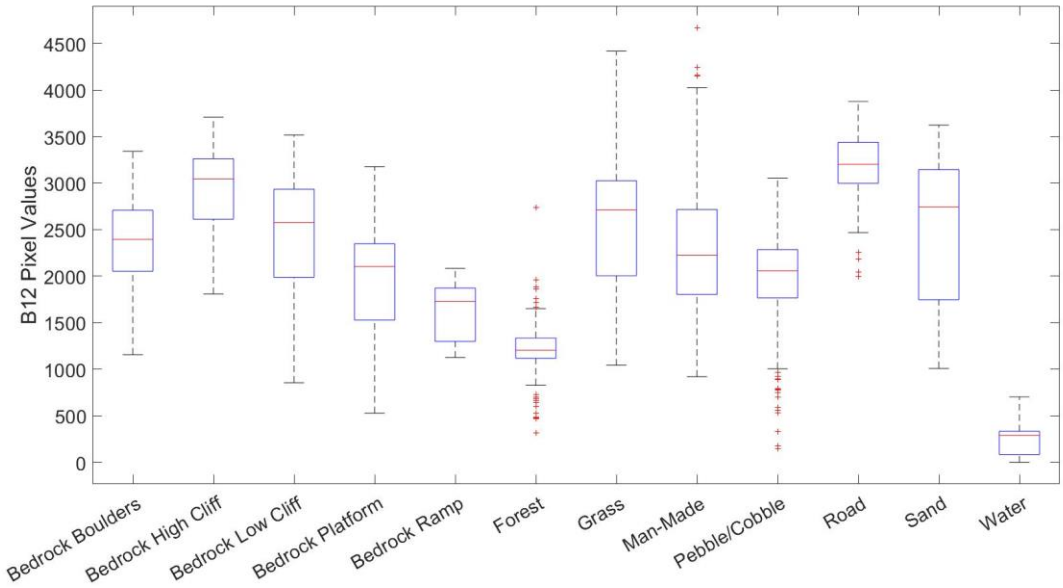

Figure C.10. Pixel distributions of the shoreline classes in Sentinel-2 B12.

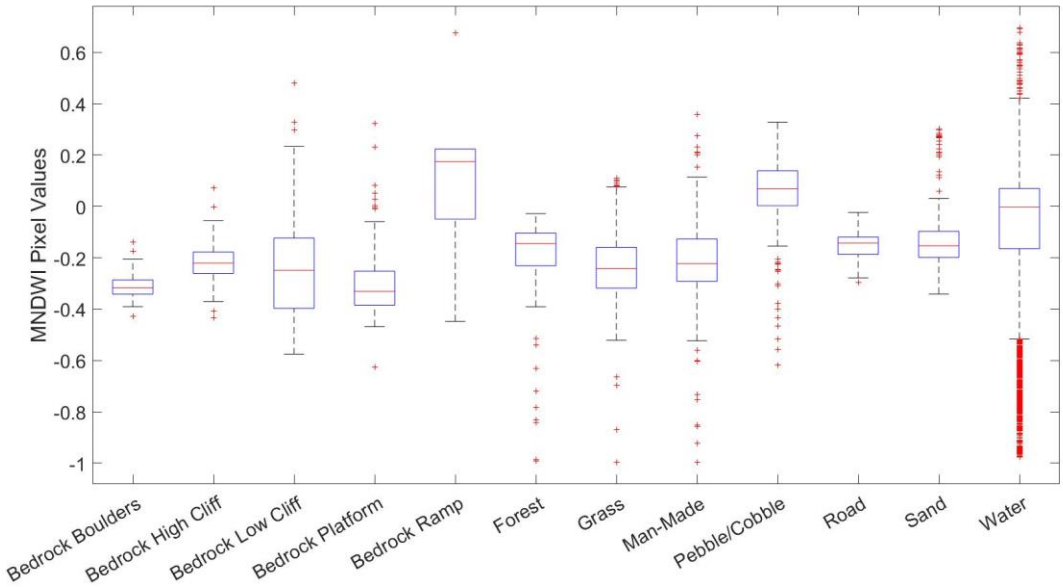

Figure C.11. Pixel distributions of the shoreline classes in MNDWI.

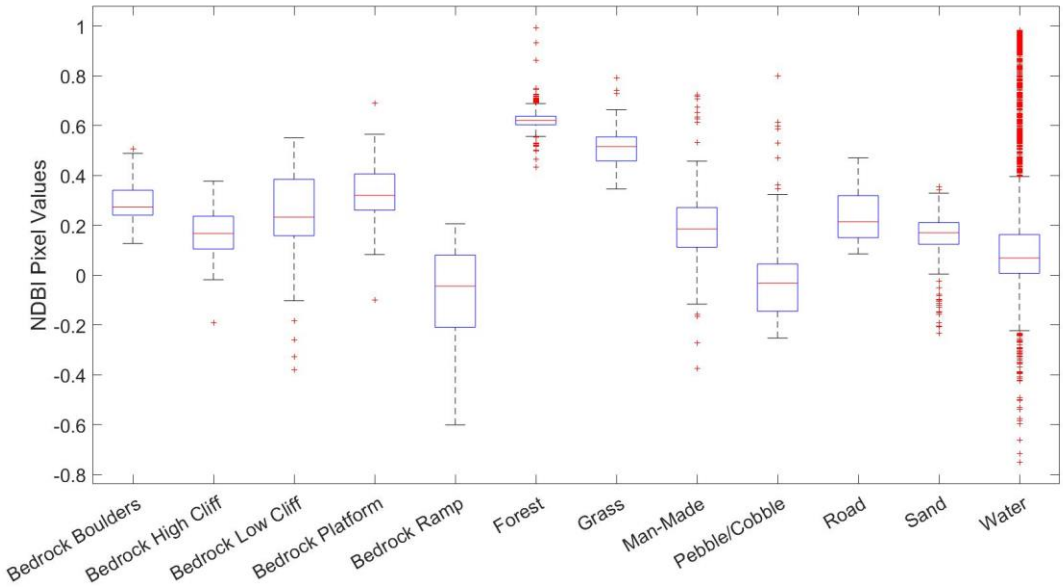

Figure C.12. Pixel distributions of the shoreline classes in NDBI.

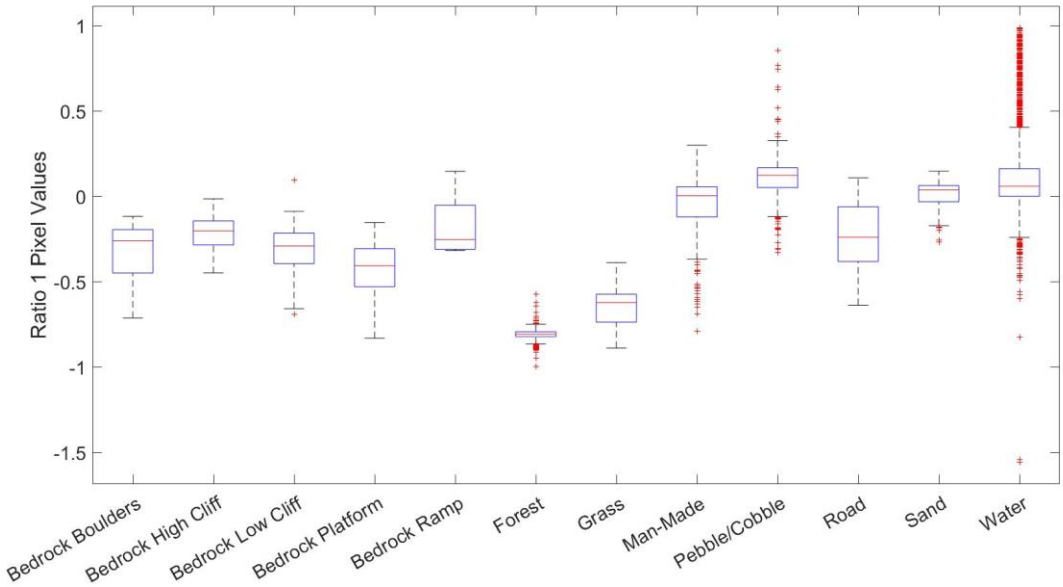

Figure C.13. Pixel distributions of the shoreline classes in Ratio 1.

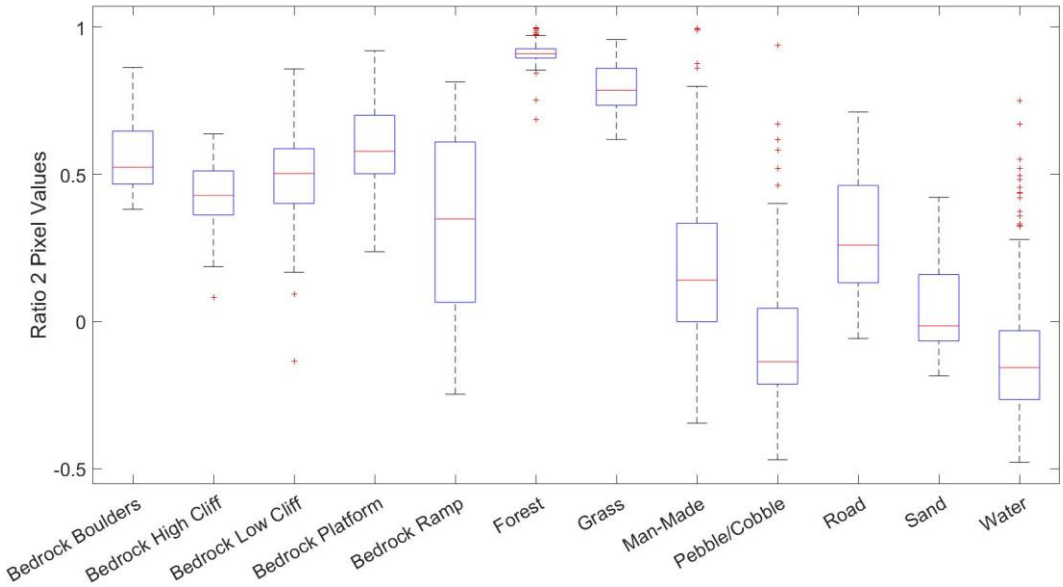

Figure C.14. Pixel distributions of the shoreline classes in Ratio 2.

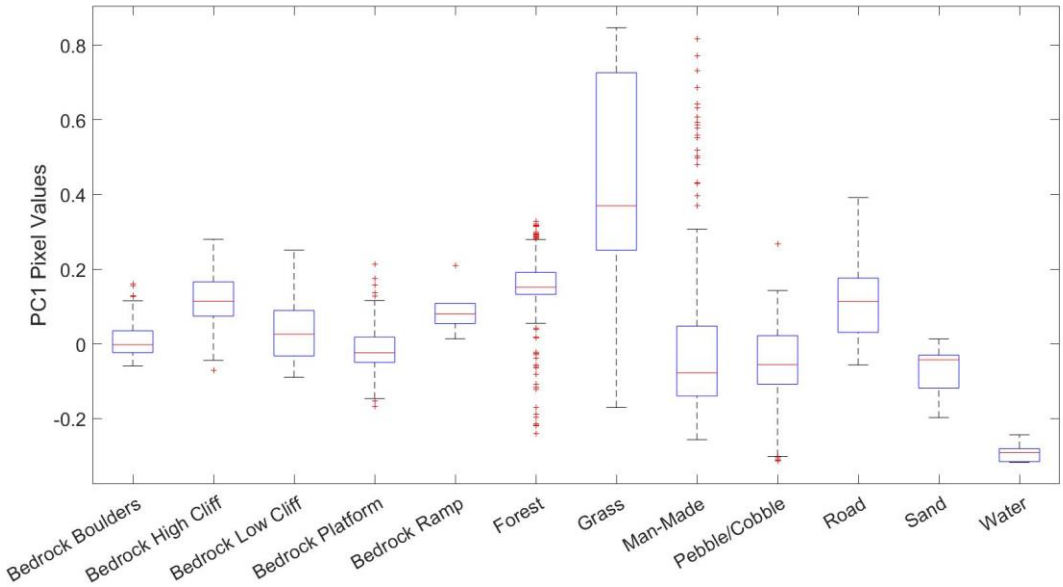

Figure C.15. Pixel distributions of the shoreline classes for PC1.

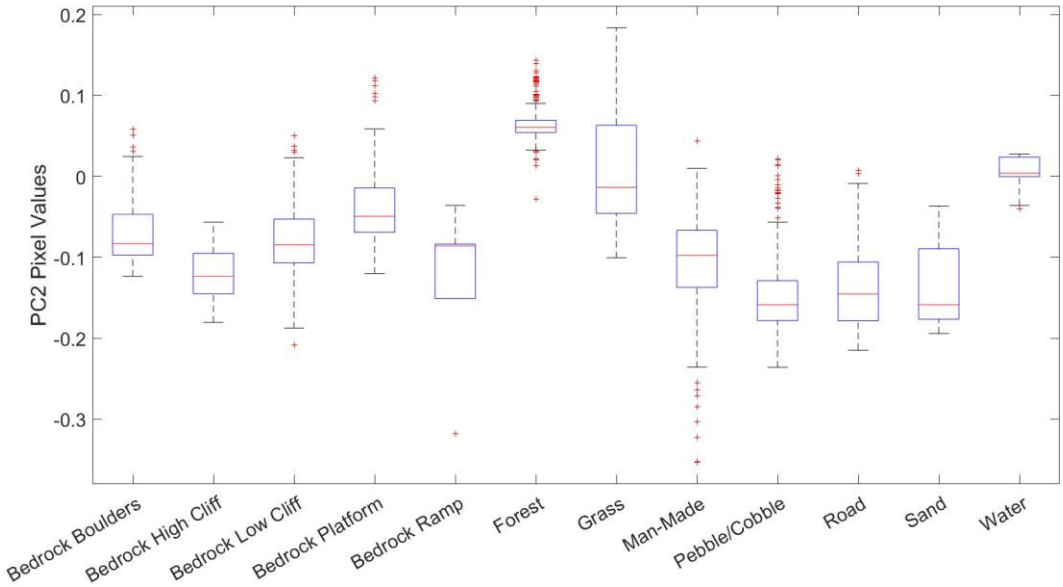

Figure C.16. Pixel distributions of the shoreline classes for PC2.

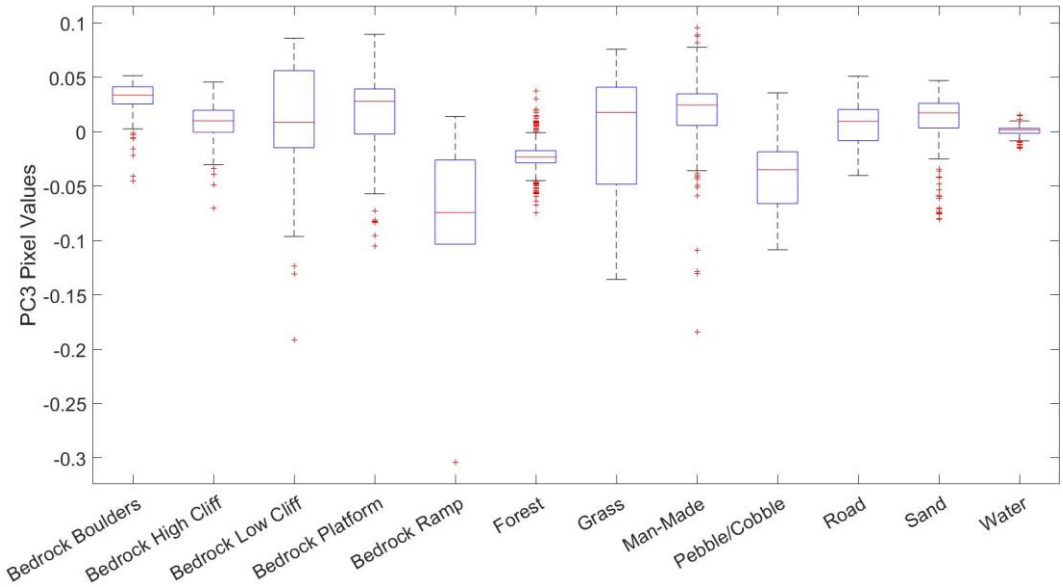

Figure C.17. Pixel distributions of the shoreline classes for PC3.

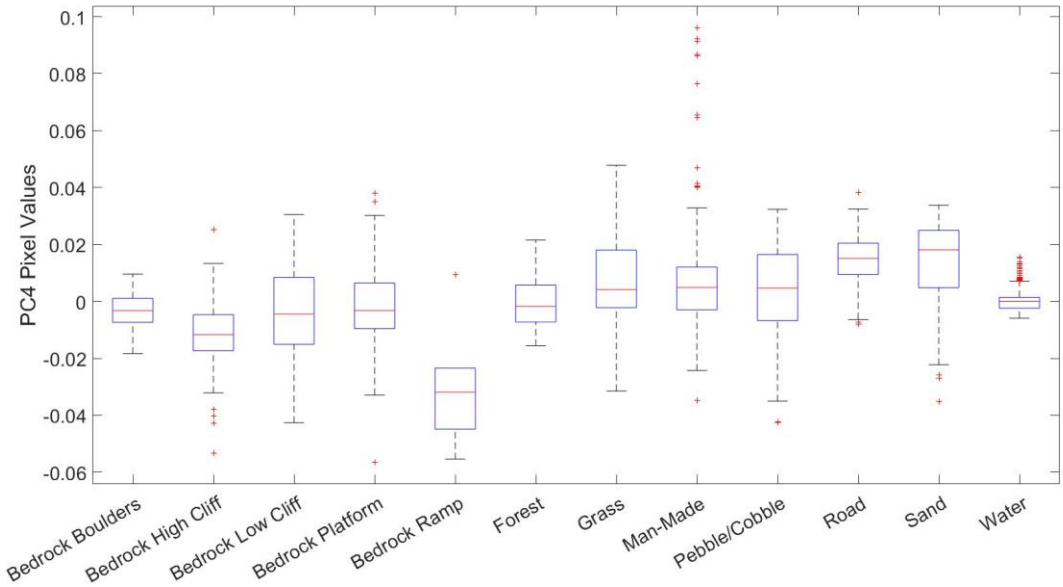

Figure C.18. Pixel distributions of the shoreline classes for PC4.

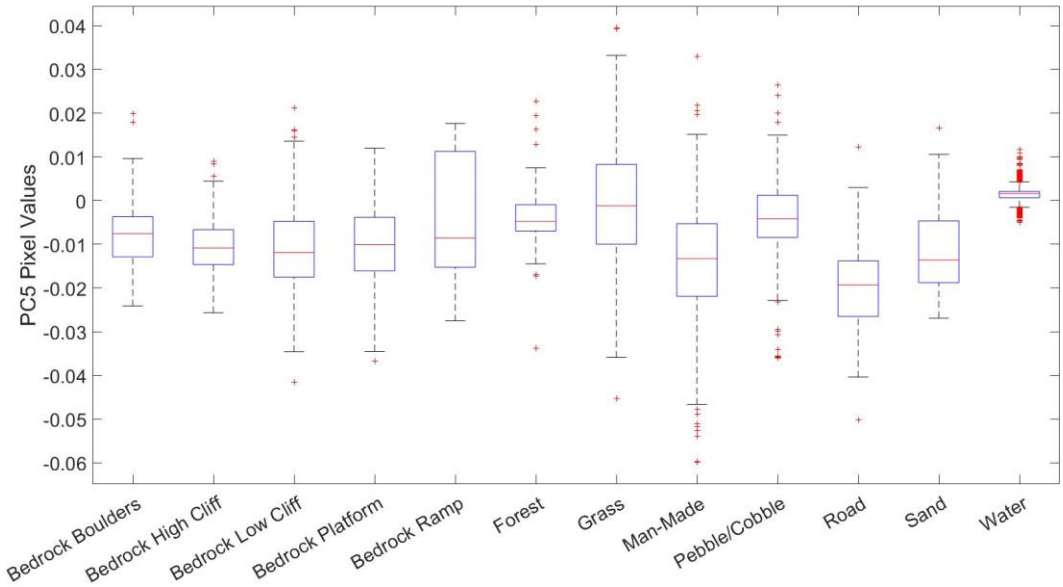

Figure C.19. Pixel distributions of the shoreline classes for PC5.

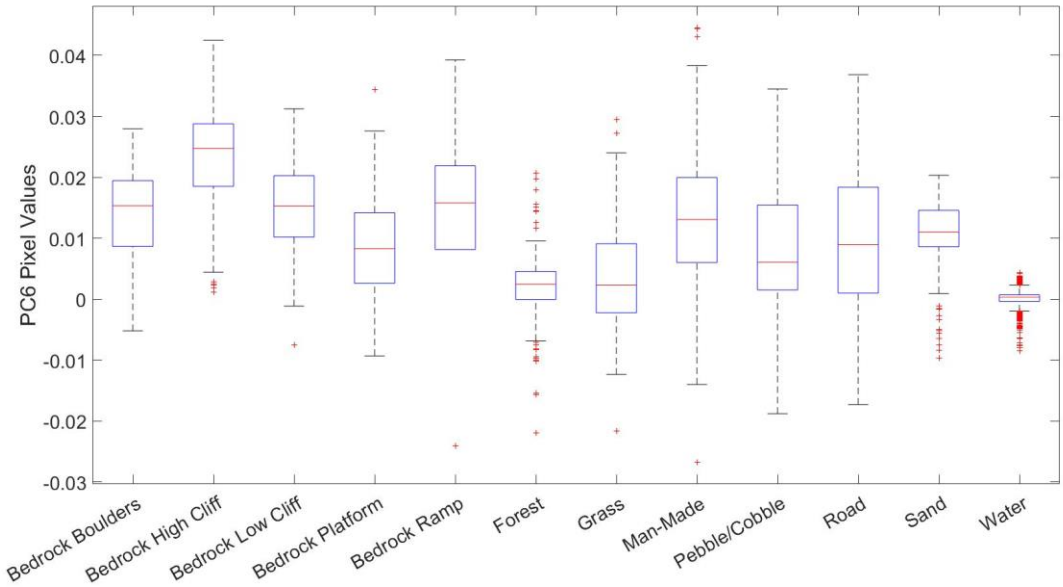

Figure C.20. Pixel distributions of the shoreline classes for PC6.

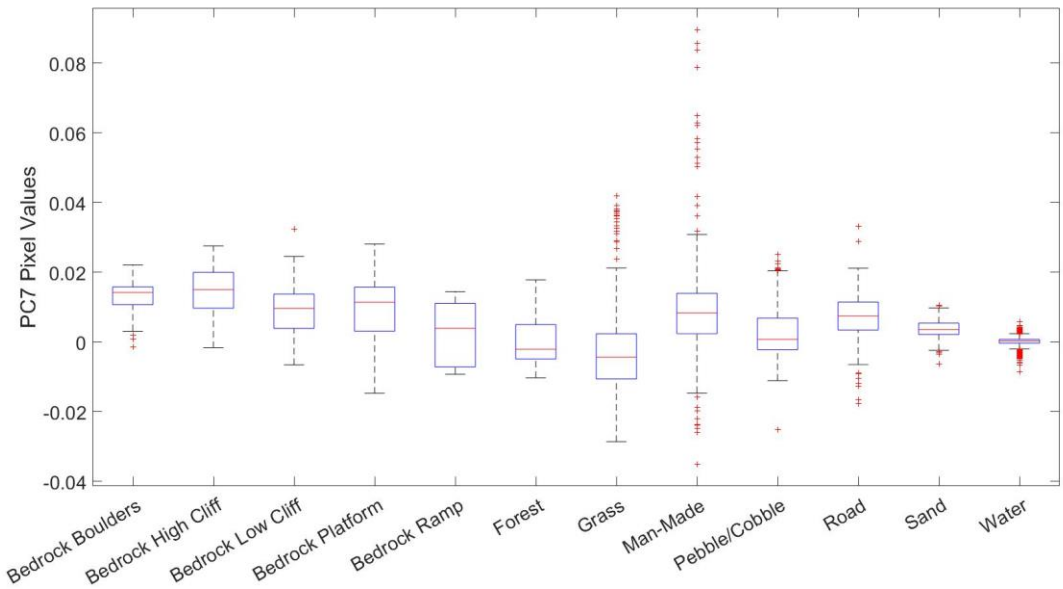

Figure C.21. Pixel distributions of the shoreline classes for PC7.

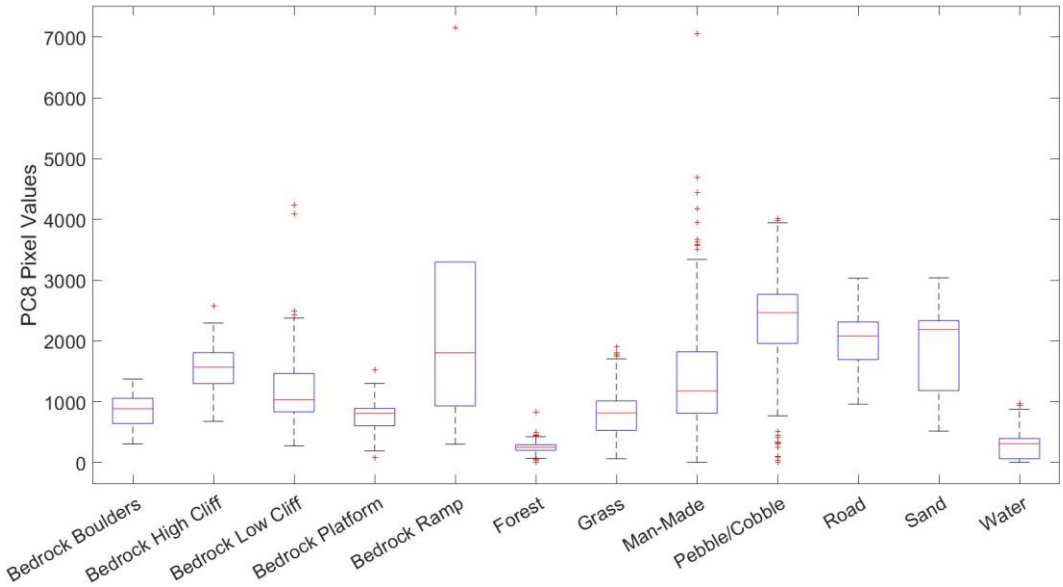

Figure C.22. Pixel distributions of the shoreline classes for PC8.

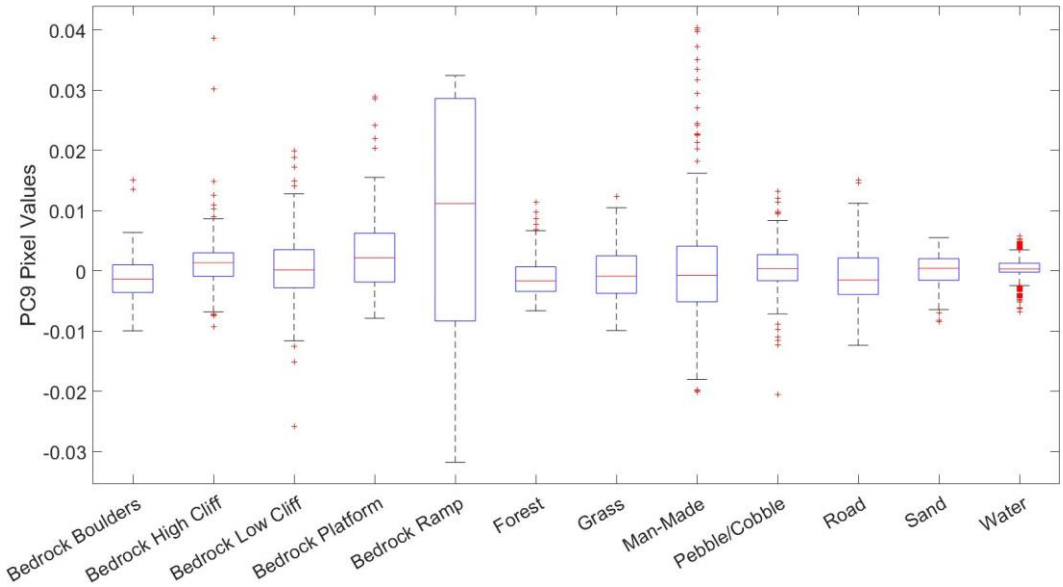

Figure C.23. Pixel distributions of the shoreline classes for PC9.

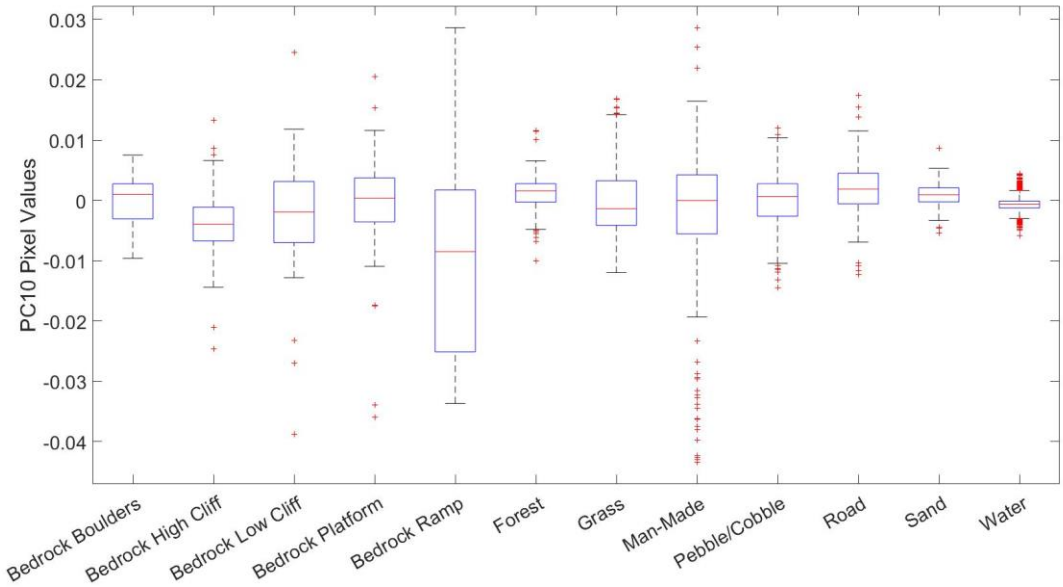

Figure C.24. Pixel distributions of the shoreline classes for PC10.

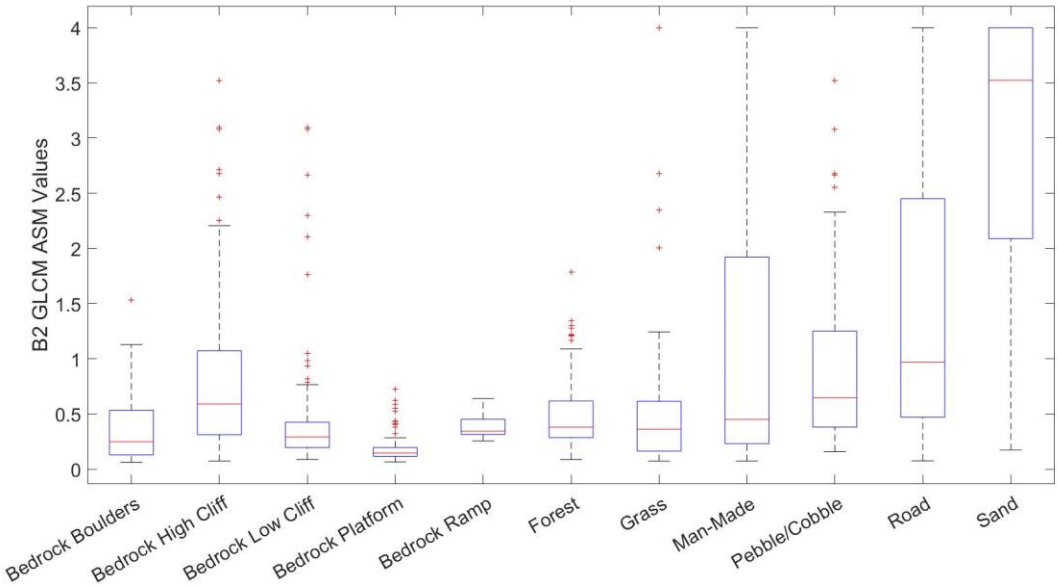

Figure C.25. Pixel distributions of the shoreline classes for B2 GLCM ASM measure.

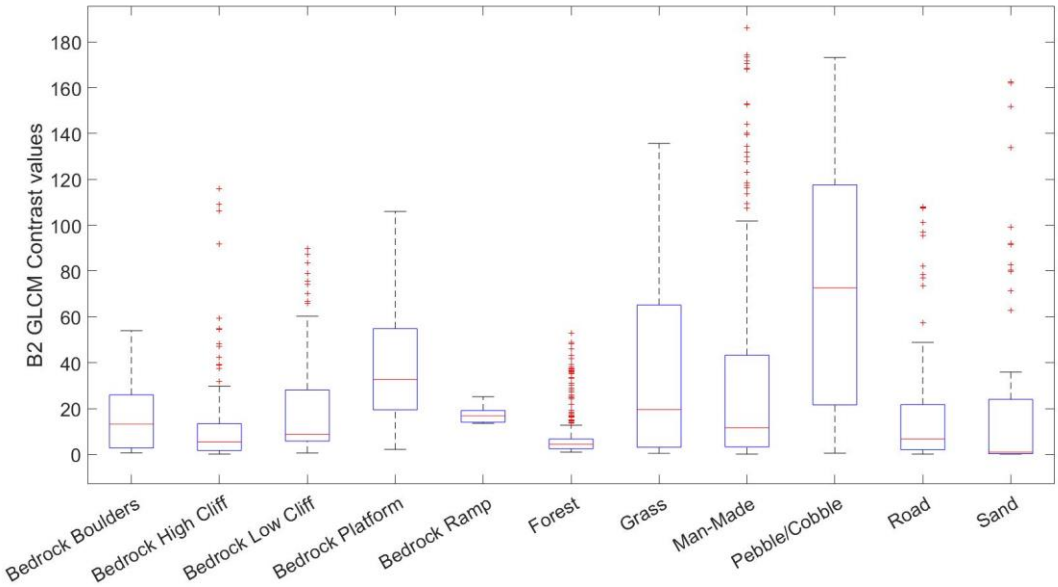

Figure C.26. Pixel distributions of the shoreline classes for B2 GLCM contrast measure.

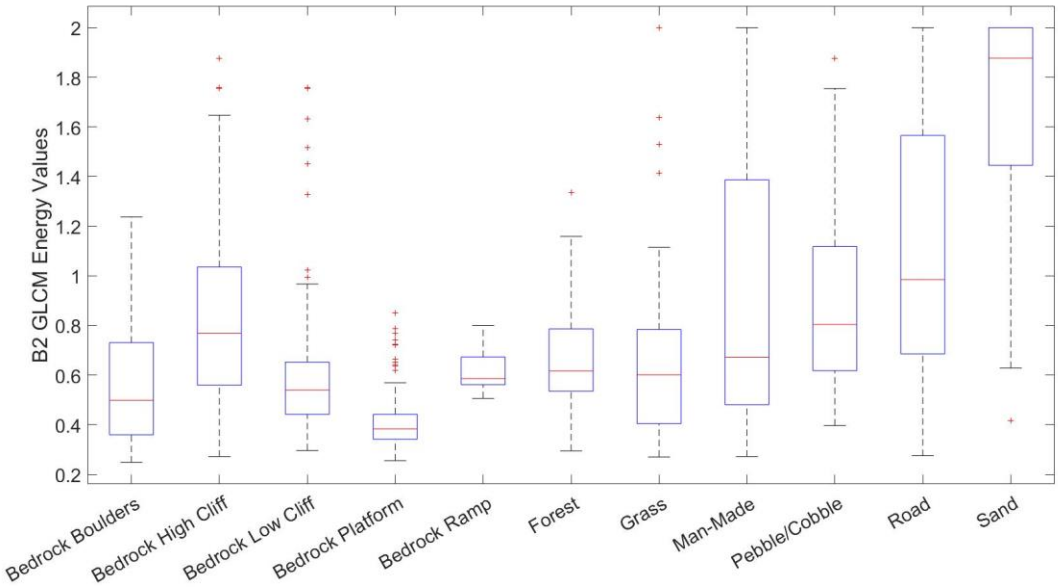

Figure C.27. Pixel distributions of the shoreline classes for B2 GLCM E measure.

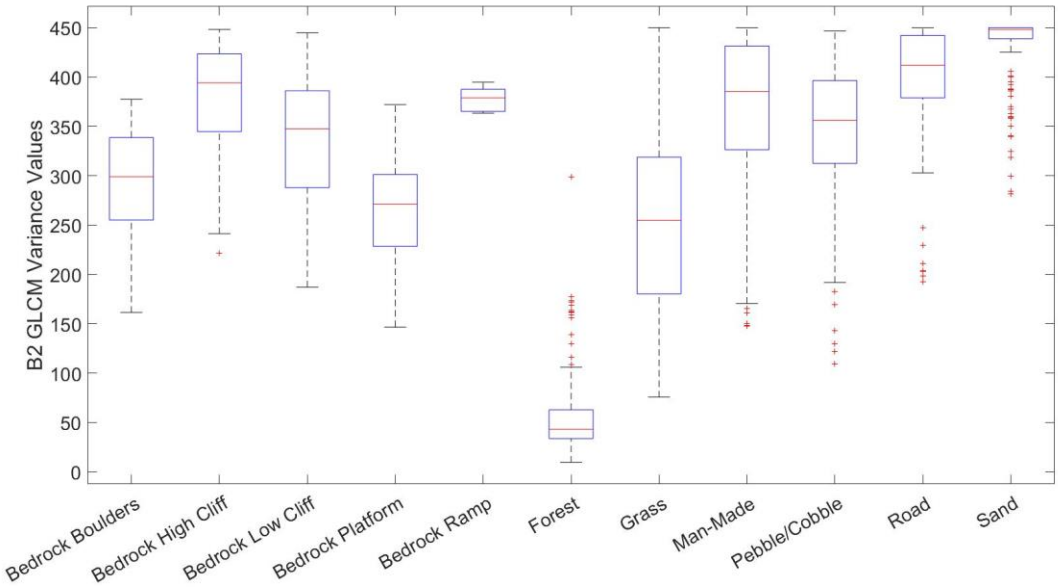

Figure C.28. Pixel distributions of the shoreline classes for B2 GLCM VAR measure.

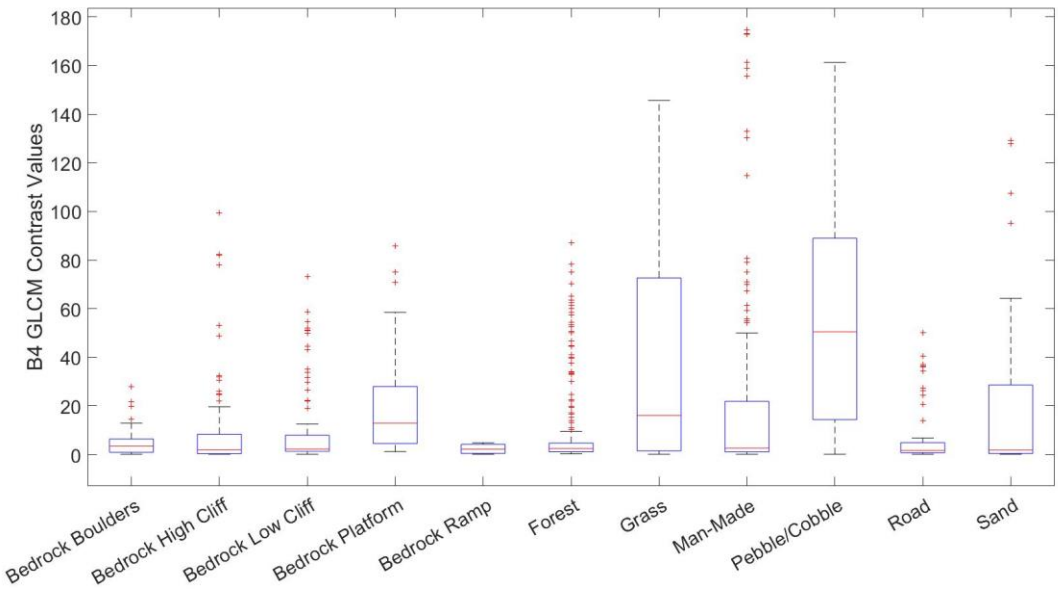

Figure C.29. Pixel distributions of the shoreline classes for B4 GLCM contrast measure.

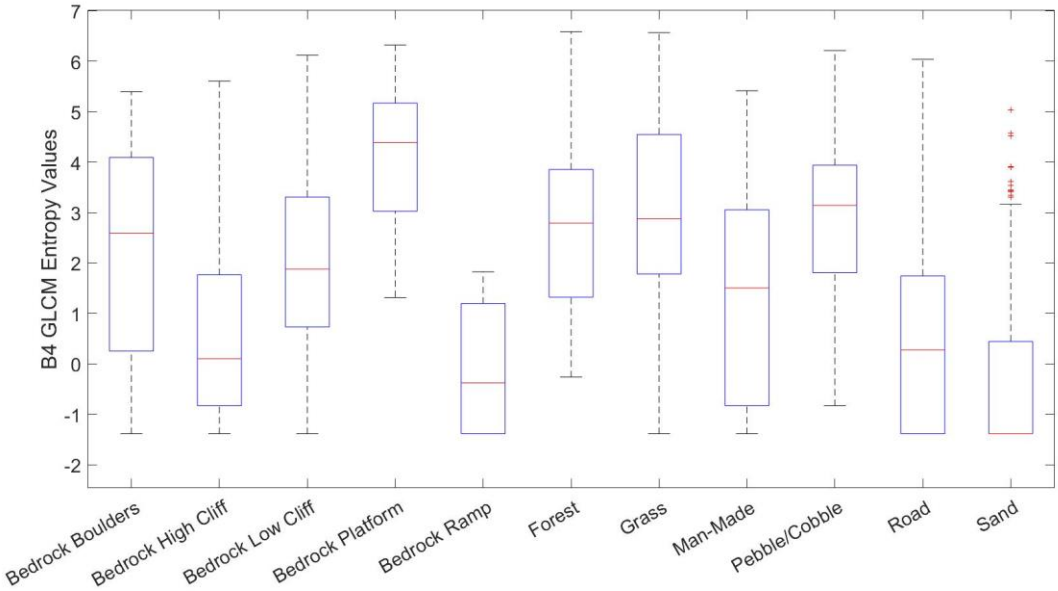

Figure C.30. Pixel distributions of the shoreline classes for B4 GLCM ENT measure.

Appendix D: Principal Components

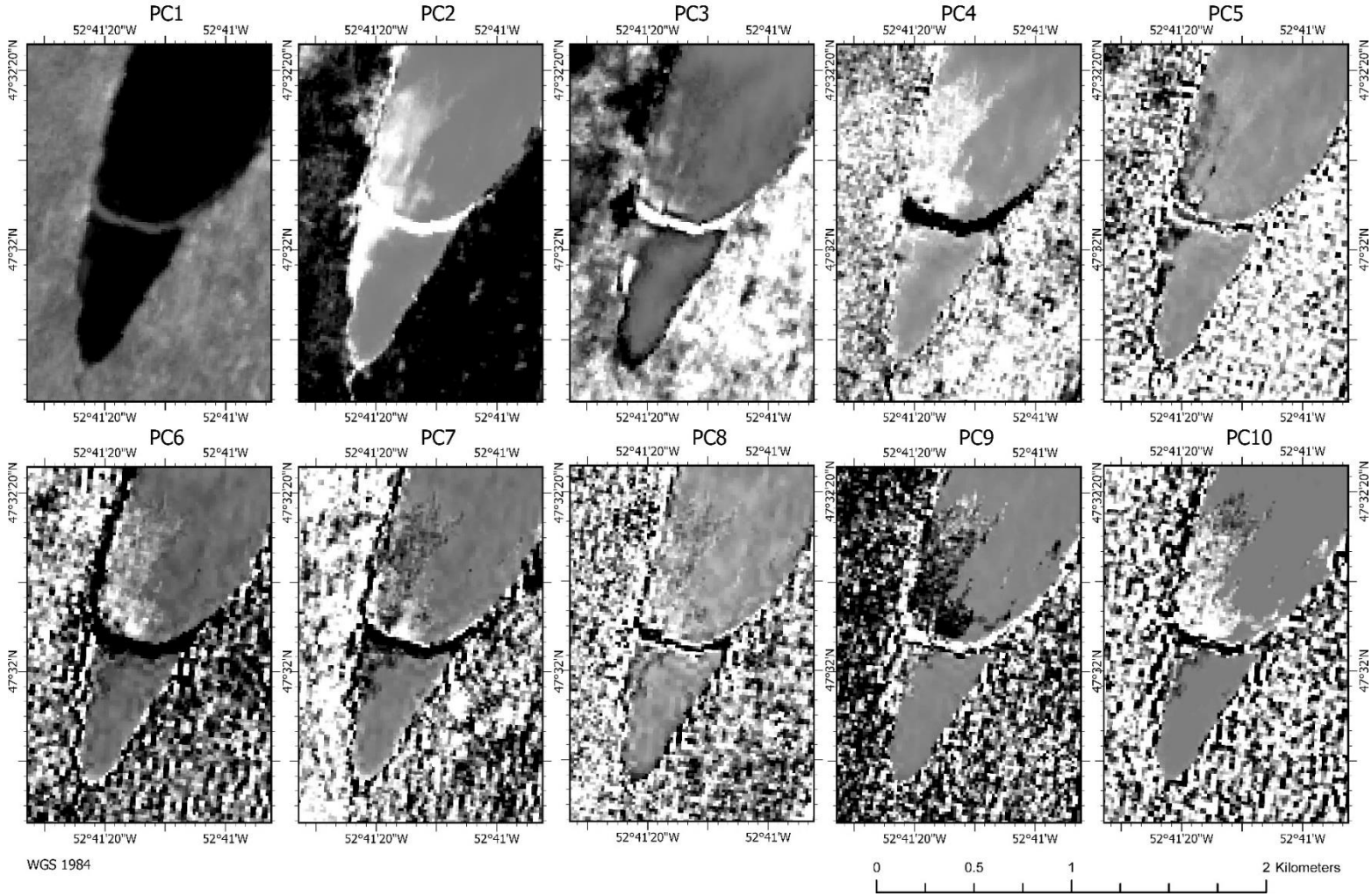

Figure D.1. Principal components obtained from Sentinel-2 red, green, blue, NIR, narrow-NIR, RE 1-3, SWIR-1, and SWIR-2 band.

This page is intentionally left blank